

FIRST- AND SECOND-ORDER PROPERTIES OF
SPATIOTEMPORAL POINT PROCESSES IN THE SPACE-TIME
AND FREQUENCY DOMAINS.

SUNDARDAS S. DORAI-RAJ

DISSERTATION SUBMITTED TO THE FACULTY OF THE
VIRGINIA POLYTECHNIC INSTITUTE AND STATE UNIVERSITY
IN PARTIAL FULFILLMENT OF THE REQUIREMENTS FOR THE DEGREE OF

DOCTOR OF PHILOSOPHY
OF
STATISTICS

OLIVER SCHABENBERGER, CHAIR

ROBERT V. FOUTZ

ERIC P. SMITH

GEORGE R. TERRELL

KEYING YE

JULY 23, 2001

BLACKSBURG, VIRGINIA

KEYWORDS: INTENSITY MEASURES, KERNEL ESTIMATION, K -FUNCTION, SPECTRAL
ANALYSIS, PERIODOGRAM, RED-COCKADED WOODPECKER, HOMERANGE ANALYSIS

COPYRIGHT © 2001, SUNDARDAS S. DORAI-RAJ

For Shelly

FIRST- AND SECOND-ORDER PROPERTIES OF SPATIOTEMPORAL POINT PROCESSES IN THE SPACE-TIME AND FREQUENCY DOMAINS.

SUNDARDAS S. DORAI-RAJ

(ABSTRACT)

Point processes are common in many physical applications found in engineering and biology. These processes can be observed in one-dimension as a time series or two-dimensions as a spatial point pattern with extensive amounts of literature devoted to their analyses. However, if the observed process is a hybrid of spatial and temporal point process, very few practical methods exist. In such cases, practitioners often remove the temporal component and analyze the spatial dependencies. This marginal spatial analysis may lead to misleading results if time is an important factor in the process.

In this dissertation we extend the current analysis of spatial point patterns to include a temporal dimension. First- and second-order intensity measures for analyzing spatiotemporal point patterns are explicitly defined. Estimation of first-order intensities are examined using 3-dimensional smoothing techniques.

Conditions for weak stationarity are provided so that subsequent second-order analysis can be conducted. We consider second-order analysis of spatiotemporal point patterns first in the space-time domain through an extension of Ripley's K -function. An alternative analysis is given in the frequency domain through construction of a spatiotemporal periodogram.

The methodology provided is tested through simulation of spatiotemporal point patterns and by analysis of a real data set. The biological application concerns the estimation of the homerange of groups of the endangered red-cockaded woodpecker in the Fort Bragg area of North Carolina. Monthly or bimonthly point patterns of the bird distribution are analyzed and integrated over a 23 month period.

ACKNOWLEDGEMENTS

I would like to thank the following people who have made all of this possible.

- My advisor, Oliver Schabenberger, for introducing me to spatial statistics and for motivating me to do my best.
- My committee members, Robert V. Foutz, Eric P. Smith, George R. Terrell, and Keying Ye.
- The Virginia Tech Department of Statistics for financially supporting me for four years and giving me invaluable experience in teaching and statistical consulting.
- My mother, Diana Dorai-Raj, for allowing me to follow any path in life I choose.
- And finally, my wife, Shelly Dorai-Raj, for enduring my long hours and offering me her love and support.

Contents

Contents	vii
List of Figures	xi
List of Tables	xiii
1 Introduction	1
1.1 Temporal Processes	3
1.1.1 Spectral Representation	4
1.1.2 The Periodogram	4
1.2 Fourier Transforms in \mathfrak{R}^d	6
1.3 Spatial Processes	7
1.3.1 Types of Spatial Processes	8
1.3.2 Spatial Point Processes	11
1.4 Spatiotemporal Point Processes	13
1.4.1 Types of Spatiotemporal Point Processes	14
1.4.2 Previous Work in Spatiotemporal Point Processes	17

1.5	An Example - The Red-cockaded woodpecker	18
2	Spatial Point Patterns	21
2.1	Intensity Measures of Spatial Point Patterns	21
2.1.1	Second-Order (Weak) Stationarity	22
2.1.2	Reduced Second-Order Intensity	24
2.1.3	Estimation of Intensities	26
2.1.4	Auto-covariance of an Orderly Spatial Point Process	29
2.2	Spectral Representation and Spatial Periodogram Analysis	30
2.2.1	Distribution of the Spatial Periodogram	33
2.2.2	Polar Representation of the Spatial Periodogram	37
2.2.3	Inference based on the R - and Θ -Spectrum	38
2.3	Geometric Anisotropy for Spatial Point Patterns	42
2.3.1	Properties of the Spatial Periodogram Under Geometric Anisotropy	44
2.3.2	Spectral Analysis under Geometric Anisotropy	47
2.3.3	Simulations for Clustered and Regular Processes	50
3	Spatiotemporal Point Patterns	52
3.1	Intensity Measures of Spatiotemporal Point Processes	52
3.1.1	First-Order Intensities	53
3.1.2	Second-Order Intensities	56
3.1.3	Second-Order (Weak) Stationarity	58

3.1.4	Reduced Second-Order Intensity	66
3.1.5	Estimation of Intensities	70
3.2	Spectral Representation and Spatiotemporal Periodogram Analysis	80
3.2.1	Distribution of the Spatiotemporal Periodogram	83
3.2.2	Polar Representation of the Spatiotemporal Periodogram	86
4	Simulation and Case Study	88
4.1	Simulated and Real Spatial Point Patterns	89
4.1.1	Simulations	89
4.1.2	Woodpecker Data	91
4.2	Simulated and Real Spatiotemporal Point Patterns	93
4.2.1	Simulating Spatiotemporal Point Patterns	93
4.2.2	Spatiotemporal K -analysis Simulation	95
4.2.3	Spatiotemporal Periodogram Simulations	96
4.2.4	Woodpecker Data	98
4.2.5	Remarks	102
5	Conclusion and Discussion	105
5.1	Proposed Work	106
5.2	Accomplishments	107
5.3	What has been learned	108
5.4	Future research	108

A Programs	110
A.1 anisotropy.mc()	111
A.2 anisotropy.pattern()	113
A.3 anisotropy.rotation()	113
A.4 hr.analysis()	113
A.5 kern.hr()	116
A.6 kern3d()	119
A.7 Lenv.mc()	120
A.8 Lhat.II()	122
A.9 make.stpp.pattern()	123
A.10 pgram.rho()	126
A.11 pgram.theta()	127
A.12 pgram.sp()	128
A.13 pgram.stp()	129
A.14 pgram.theta.htest()	132
 Bibliography	 134

List of Figures

1.1	Examples of Spatial Point Patterns.	11
1.2	Examples of Spatiotemporal Point Patterns.	15
1.3	The Red-cockaded Woodpecker.	18
1.4	Woodpecker Data	19
2.1	\widehat{L} -analysis of Spatial Point Patterns	28
2.2	Polar Spectra	38
2.3	Spectral Analysis of Spatial Point Patterns	39
2.4	Geometric Anisotropy	44
2.5	Geometric Anisotropic Poisson Process	48
2.6	Ratio of Θ -spectrum Ordinates	49
2.7	Geometric Anisotropic Clustered Process	50
2.8	Geometric Anisotropic Sequential Inhibition Process	51
3.1	Spatiotemporal First-Order Stationarity	58
3.2	Integrating the Conditional Spatiotemporal Intensity	61

3.3	Obtaining $K_I(h, k)$ and $K_{II}(h, k)$	69
3.4	Edge-correction Weights for $K(t \mathbf{s})$	72
3.5	Edge-correction Weights for $K_I(h, k)$	74
3.6	Edge-correction Weights for $K_{II}(h, k)$	76
4.1	Spatial periodogram for simulated CSR point patterns	91
4.2	Clustering radius and angle of rotation for FB002 family	92
4.3	Results of simulated \widehat{L} -functions	96
4.4	CSTR periodogram simulation	97
4.5	Kernel intensity estimates for FB002	99
4.6	95% homerange areas for FB002	100
4.7	R_γ -spectrum with $\rho = 2$ for FB002	101
4.8	Θ_γ -spectrum for FB002	103
4.9	R_γ -spectrum for FB002	104

List of Tables

2.1	Results of \hat{L} -analysis	29
3.1	First-Order Intensity Measures.	55
3.2	Second-Order Intensity Measures.	58
4.1	<code>make.pattern</code> calls for generating simulated data	89

Chapter 1

Introduction

Two common types of correlated data arise when observations are related temporally and/or spatially. In the temporal context the data are collected over time either through a longitudinal study or as a time series. A longitudinal study consists of collecting data from clusters or subjects over time and is quite often constructed as a repeated measures design [Hinkelmann and Kempthorne, 1992]. A time series may be thought of as a special case of a longitudinal study for which only one cluster exists. In the spatial context the notion of autocorrelation was best coined by Tobler's law, "everything is related to everything else, but near things are more related than distant things" [Tobler, 1970]. Much of the literature on correlated data is devoted to one of these fields. However, the literature is comparatively sparse for data that is correlated both temporally and spatially.

Analysis of continuous time series data is possible either in the time domain through the auto-correlation function (ACF) or in the frequency domain through the periodogram. The analysis of the ACF, and subsequently the Partial ACF and Inverse ACF, are discussed in great detail by Box et al. (1994). Estimating, for example, Auto-Regressive Moving Average (ARMA) models is straightforward in the time domain. Many scientists and statisticians prefer the time domain approach because of the relative ease of interpretation. Conversely, the frequency domain of time series data is steeped in Hilbert space algebra. For this reason,

spectral analysis is used little in practice due to its seemingly esoteric nature. However, the spectral analysis has advantages in its nonparametric approach to data analysis. Although ARMA models can be obtained in the frequency domain, the spectral approach does not require any parametric model for inference.

Similarly, continuous spatial data can be analyzed in the spatial domain through the semi-variogram or in the frequency domain through the spatial periodogram. Even more so than for time series data, the spectral analysis of spatial data is greatly overshadowed by analysis in the spatial domain. Papers by Renshaw and Ford (1983), Vecchia (1985), and Mugglestone and Renshaw (1996b) have been promoting the use of spectral analysis for spatial data since Bartlett (1964) first suggested this approach. As in time series analysis, the frequency domain takes a more abstract approach to the data, intimidating many by concepts in Fourier transforms and Hilbert space theory.

A special case of time series or spatial data is the point process. In point processes, the data collected are coordinates of events in time or space. Point processes are covered in detail by Bartlett (1975) and Daley and Vere-Jones (1988). Bartlett (1964, 1975) extends analysis of the spatial point process to the frequency domain through the spatial periodogram. Ripley (1976) introduced the analysis in the spatial domain through his celebrated K -function. Currently, Ripley's approach of studying the dependency structure of point patterns remains the dominant method for analysis.

In this dissertation, we first discuss basic concepts in time series and spatial statistics. Further, we will gather current methods for analyzing spatial point processes in the spatial and frequency domains. Bringing together arguments of time series and spatial statistics, we then define methods for analyzing spatiotemporal point patterns in both the space-time and frequency domains and establish their properties.

This chapter is organized in a fashion that blends the theory and methodology of time series and spatial statistics. Section 1 covers basic periodogram analysis in time series and Fourier transforms in \mathfrak{R} . In Section 2, a sketch of the extension of the Fourier transform to \mathfrak{R}^d is

given. Section 3 is concerned with methodology for analyzing spatial processes in general and spatial point patterns in particular. Section 4 describes types of spatiotemporal point processes and lists established work in this area.

Chapter 2 extends the work of Renshaw and Ford for the spectral analysis of spatial point patterns. Chapter 3 introduces new definitions for spatiotemporal intensities and their estimators and states conditions of weak spatiotemporal stationarity. Chapter 4 applies the theories of Chapter 3 to simulated spatiotemporal point processes as well as the red-cockaded woodpecker data. Chapter 5 summarizes the conclusions and offers avenues future research in this important area.

1.1 Temporal Processes

Before discussing spatiotemporal processes, a brief review of time series analysis in the frequency domain is prudent. Much of the terminology in the frequency domain of a temporal process will be extended both for spatial processes and spatiotemporal processes.

A stochastic process observed over time is called a time series [Box et al., 1994]. A time series can either be analyzed in the time domain or in the frequency domain. Descriptions of the former approach can be found in Box et al. (1994). A brief discussion and the relative merits of the latter approach follow.

Define a real-valued time series by

$$\{X_t \in \Re : -\infty < t < \infty\}. \quad (1.1.1)$$

The stochastic process in (1.1.1) is said to be a second-order (weakly) stationary if

$$E(X_t) = \mu (= 0)$$

and

$$\text{cov}(X_t, X_{t-k}) = c(k), \quad (1.1.2)$$

where $c(k)$ is the auto-covariance function and is completely specified by the time lag k . Without loss of generality, the time series is usually detrended so that $E(X_t) = 0$.

1.1.1 Spectral Representation

By Bochner's theorem (see, e.g., Goldberg 1961), if $c(0) < \infty$, the spectral representation of the auto-covariance function given by (1.1.2) can be written as

$$c(k) = \int_{-\infty}^{\infty} e^{i\gamma k} F(d\gamma), \quad (1.1.3)$$

where γ is the frequency for which $c(k)$ is decomposed and $F(\gamma)$ is the spectral distribution function [Koopmans, 1971]. If $F(d\gamma) = f(\gamma)d\gamma$, then we define $f(\gamma)$ as the spectral density of the auto-covariance function. Taking the Fourier transform of $c(k)$ gives us $f(\gamma)$:

$$f(\gamma) = \frac{1}{2\pi} \int_{-\infty}^{\infty} c(k) e^{-i\gamma k} dk. \quad (1.1.4)$$

Koopmans (1971) sketches the proof of the spectral representation (1.1.3).

1.1.2 The Periodogram

A nonparametric estimate of the spectral density can be constructed through the periodogram, an estimate of (1.1.4). To obtain the periodogram we first obtain the discrete Fourier transform (DFT) of the data

$$J(\gamma_\nu) = \frac{1}{\sqrt{2\pi T}} \sum_{t=1}^T x_t \exp\{i\gamma_\nu t/T\}, \quad (1.1.5)$$

for frequencies $\gamma_\nu = 2\pi\nu$, where $\nu = -\lfloor \frac{T-1}{2} \rfloor, \dots, \lfloor \frac{T}{2} \rfloor$. ($\lfloor \cdot \rfloor$ denotes the floor, or greatest integer, function.) Thus the periodogram has the form

$$\begin{aligned}
 I(\gamma_\nu) &= J(\gamma_\nu)\overline{J}(\gamma_\nu) \\
 &= \left(\frac{1}{\sqrt{2\pi T}} \sum_{u=1}^T x_u \exp\{i\gamma_\nu u/T\} \right) \left(\frac{1}{\sqrt{2\pi T}} \sum_{t=1}^T x_t \exp\{i\gamma_\nu t/T\} \right) \\
 &= \frac{1}{2\pi T} \sum_{t=1}^T \sum_{u=1}^T x_t \cdot x_u \exp\{-i\gamma_\nu(t-u)/T\} \\
 &= \frac{1}{2\pi T} \sum_{k=-(T-1)}^{T-1} \hat{c}(k) \exp\{-i\gamma_\nu k/T\},
 \end{aligned}$$

where $\overline{J}(\gamma_\nu)$ is the complex conjugate of $J(\gamma_\nu)$ and $\hat{c}(k)$ is an estimate of (1.1.2) after the time series has been detrended.

The periodogram is an unbiased estimate of the spectral density $f(\gamma)$ but is inconsistent [Koopmans, 1971]. To improve the consistency of $I(\gamma_\nu)$ a smoothing parameter is incorporated. Specifically, the spectral density $f(\gamma)$ is estimated by the smoothed periodogram $I(\gamma_\nu)$ given by

$$\hat{f}(\gamma) = \sum_{\nu=-\lfloor (T-1)/2 \rfloor}^{\lfloor T/2 \rfloor} W(\gamma - \gamma_\nu) I(\gamma_\nu), \quad (1.1.6)$$

where $W(\cdot)$ is a spectral window. W is chosen to be a symmetric, periodic, and real-valued weight function for which

$$\sum_{\nu=-\lfloor (T-1)/2 \rfloor}^{\lfloor T/2 \rfloor} W(\gamma_\nu) = 1.$$

Examples of spectral windows and their respective properties can be found in Koopmans (1971, p. 279).

The main advantage of analyzing a time series via the frequency domain is asymptotic independence of the periodogram ordinates. Test statistics about the second-order properties can be formulated with simple asymptotic properties. Also, from a theoretical standpoint,

the spectral domain offers simpler mathematical proofs.

1.2 Fourier Transforms in \Re^d

In order to extend the spectral representation to the spatial context, and ultimately to the spatiotemporal context, a brief discussion of higher dimension Fourier transforms is required. The extension of the univariate Fourier transform draws on the separation of variables [Haberman, 1987]. Suppose we are given a function $f(\mathbf{x})$ where $\mathbf{x} \in \Re^d$ and $f(\mathbf{x})$ decays sufficiently fast as each element of $\mathbf{x} \rightarrow \pm\infty$. The Fourier transform in x_1 is defined by

$$F(\omega_1, \mathbf{x}^*) = \frac{1}{2\pi} \int_{-\infty}^{\infty} f(x_1, \mathbf{x}^*) e^{-i\omega_1 x_1} dx_1 \quad (1.2.1)$$

and the inverse Fourier transform is defined by

$$f(x_1, \mathbf{x}^*) = \int_{-\infty}^{\infty} F(\omega_1, \mathbf{x}^*) e^{i\omega_1 x_1} d\omega_1, \quad (1.2.2)$$

where $\mathbf{x}^* = [x_2 \ \dots \ x_d]'$. Applying the Fourier transform to (1.2.1) and (1.2.2) for x_2 we get

$$F(\omega_1, \omega_2, \mathbf{x}^{**}) = \frac{1}{(2\pi)^2} \int_{-\infty}^{\infty} \int_{-\infty}^{\infty} f(x_1, x_2, \mathbf{x}^{**}) e^{-i(\omega_1 x_1 + \omega_2 x_2)} dx_1 dx_2$$

and

$$f(x_1, x_2, \mathbf{x}^{**}) = \int_{-\infty}^{\infty} \int_{-\infty}^{\infty} F(\omega_1, \omega_2, \mathbf{x}^{**}) e^{i(\omega_1 x_1 + \omega_2 x_2)} d\omega_1 d\omega_2,$$

where $\mathbf{x}^{**} = [x_3 \ \dots \ x_d]'$. Continuing in this fashion leads to the Fourier transform of $f(\mathbf{x})$ defined by

$$F(\boldsymbol{\omega}) = \frac{1}{(2\pi)^d} \int_{-\infty}^{\infty} \cdots \int_{-\infty}^{\infty} f(\mathbf{x}) e^{-i\boldsymbol{\omega}'\mathbf{x}} d\mathbf{x} \quad (1.2.3)$$

and the inverse transform

$$f(\mathbf{x}) = \int_{-\infty}^{\infty} \cdots \int_{-\infty}^{\infty} F(\boldsymbol{\omega}) e^{i\boldsymbol{\omega}'\mathbf{x}} d\boldsymbol{\omega}, \quad (1.2.4)$$

where $\boldsymbol{\omega}'\mathbf{x} = \sum_{j=1}^d \omega_j x_j$. Strichartz (1994) cautions that there is no agreement among mathematical texts on whether the minus sign on the exponential should be with (1.2.2) or (1.2.4) or where the factor $1/(2\pi)^d$ should be placed. The notation described above is used in the rest of this text.

1.3 Spatial Processes

A stochastic process with a spatial domain is called a spatial process. A spatial process is defined by

$$\{Z(\mathbf{s}) : \mathbf{s} \in D \subset \mathfrak{R}^2\}, \quad (1.3.1)$$

where D is an index set and $Z(\mathbf{s})$ is the attribute of interest at location \mathbf{s} . For simplicity, the dimension of D will be 2, representing observations in the plane. The main difference between (1.1.1) and (1.3.1) is that locational information is not directed as t is. Time flows unidirectionally, whereas there are no equivalents to past, present, or future in a spatial domain. For this reason many of the methods used to analyze time series must be modified to be appropriate in the spatial context and many techniques of spatial data analysis have been developed independently of progress in time series analysis.

In the geostatistical literature $Z(\mathbf{s})$, the attribute of interest observed at location \mathbf{s} , is often viewed in the context of random functions (see, e.g., Journel and Huijbregts 1978, Goovaerts 1997, Chilès and Delfiner, 1999). Briefly, $Z(\mathbf{s}, \omega)$ depends on the realization ω of a random experiment. For a given realization $Z(\cdot, \omega)$ is a function of spatial locations and n observations $Z(\mathbf{s}_1), \dots, Z(\mathbf{s}_n)$ represent an n -dimensional sample of size one from the set of all possible random functions. The stochastic behavior of the attribute Z at location \mathbf{s} is induced by considering all possible realizations of the random experiment at that location $Z(\mathbf{s})$.

1.3.1 Types of Spatial Processes

Viewing spatial processes as stochastic processes according to (1.3.1) is general in that the nature of the index set D permits the definition of different types of spatial data. Three spatial data types are defined as follows, according to Cressie (1993):

1. GEOSTATISTICAL DATA

$Z(\mathbf{s})$ is a random variable observed at locations $\mathbf{s} \in D$, where D is fixed and continuous.

Examples: Random or systematic sampling of a surface, drilling for ore, plant yields across a corn field.

2. LATTICE DATA

$Z(\mathbf{s})$ is a random variable observed at locations $\mathbf{s} \in D$, where D is fixed and discrete.

Examples: Sudden infant deaths by county in North Carolina, field experiments, unemployment rates by census tracts, coloring on remotely sensed pixel images.

3. POINT PATTERNS

$Z(\mathbf{s})$ is a random variable observed at locations $\mathbf{s} \in D$, where D is a random set of indices.

Examples: Positions of lunar craters, locations of trees in a forest, residences that reported break-ins in 1999.

A spatial point process (SPP) differs from the first two types of spatial data in that the domain D is a random set containing location \mathbf{s} of events. Whereas interest with geostatistical and lattice data lies in studying the properties of $Z(\mathbf{s})$ or $E[Z(\mathbf{s})]$, for spatial point processes studying the properties of the set D is the primary focal point.

In terms of the variable $Z(\mathbf{s})$, it is considered a degenerate random variable in a simple point pattern. Drawing on familiar definitions for binary variables we could put

$$Z(\mathbf{s}) = \begin{cases} 1 & \mathbf{s} \in D \\ 0 & \mathbf{s} \notin D \end{cases}, \quad (1.3.2)$$

but since locations not in D are locations without events, this frequently cited definition is somewhat construed. A process where $Z(\mathbf{s}) = 1 \forall \mathbf{s} \in D$ is called a simple point process to emphasize that only the random locations at which events occur are of interest. A second class of point processes allows $Z()$ to vary randomly in addition to the stochastic nature of D . Examples of such marked point processes, that derives its denomination from labelling $Z()$ the mark variable, would be recording the random locations at which trees regenerate (\mathbf{s}) and the height of the trees ($Z()$), or the location and magnitude of earthquakes.

In this dissertation we restrict attention to simple point processes. Furthermore, point processes are considered to be orderly in the sense that

$$\lim_{|ds| \rightarrow 0} P(N(ds) > 1) = 0, \quad (1.3.3)$$

where ds is an infinitesimal disk at location \mathbf{s} with volume $|ds|$ and $N(ds)$ denotes the number of events in the disk. In other words, only those processes are considered where any given location can record at most one event. If the number of possible events at \mathbf{s} exceeds one, $Z()$ could be defined as a discrete mark variable.

For geostatistical and lattice data, a weakly stationary process is defined similarly to a second-order (or weakly) stationary temporal process. Specifically, a spatial process is weakly stationary if

$$E[Z(\mathbf{s})] = \mu$$

and

$$\text{cov}[Z(\mathbf{s}_i), Z(\mathbf{s}_j)] = c(\mathbf{h}), \quad (1.3.4)$$

where $\mathbf{h} = \mathbf{s}_i - \mathbf{s}_j$ is a two-dimensional vector containing the shift in location from site \mathbf{s}_i to site \mathbf{s}_j . This is analogous to weak temporal stationarity in that the stochastic process is location invariant and self-replicating.

For spatial point patterns, weak stationarity is defined through the first- and second-order intensities. Specifically, the first-order intensity is a measure of uniformity and is given by

$$\lambda(\mathbf{s}) = \lim_{|d\mathbf{s}| \rightarrow 0} \frac{E[N(d\mathbf{s})]}{|d\mathbf{s}|},$$

where $N(d\mathbf{s})$ and $d\mathbf{s}$ are defined in (1.3.3). The second-order intensity is a measure of the dependency structure of the events in D and is given by

$$\lambda_2(\mathbf{s}_i, \mathbf{s}_j) = \lim_{|d\mathbf{s}_i|, |d\mathbf{s}_j| \rightarrow 0} \frac{E[N(d\mathbf{s}_i)N(d\mathbf{s}_j)]}{|d\mathbf{s}_i||d\mathbf{s}_j|}.$$

As with the other types of spatial data, a spatial point process is weakly stationary if the process is location invariant. This is equivalent to saying $\lambda(\mathbf{s}) \equiv \lambda$ so that the expected number of events at an arbitrary location \mathbf{s} is constant for all $\mathbf{s} \in D$; and $\lambda_2(\mathbf{s}_i, \mathbf{s}_j) \equiv \lambda_2(\mathbf{h})$ so that the dependence between events at two arbitrary locations \mathbf{s}_i and \mathbf{s}_j depends only on the difference \mathbf{h} . A more thorough discussion of weak stationarity of spatial point patterns is given in Section 2.1.

A spatial process has the distinction from a temporal process in that its observations typically cannot be ordered. However, if a spatial process is weakly stationary, we can write the covariance between any two observations as a function of the distance between them. We will define two types of weakly stationary covariance functions: anisotropic and isotropic ones. An anisotropic process has covariance function defined by (1.3.4) but covariances that differ with direction. In an isotropic process the covariance function does not depend on direction and \mathbf{h} can be replaced by $h = \|\mathbf{s}_i - \mathbf{s}_j\|_2 = [(s_{ix} - s_{jx})^2 + (s_{iy} - s_{jy})^2]^{1/2}$, the Euclidean distance between \mathbf{s}_i and \mathbf{s}_j . An isotropic process is thus invariant under coordinate shifts and rotations.

1.3.2 Spatial Point Processes

Spatial point patterns can be categorized into three classes: a) Regular Processes, b) Aggregated Processes, and c) Complete Spatial Randomness (CSR). All three types can be observed with isotropic or anisotropic covariance functions. Details of these processes can be found in Cressie (1993).

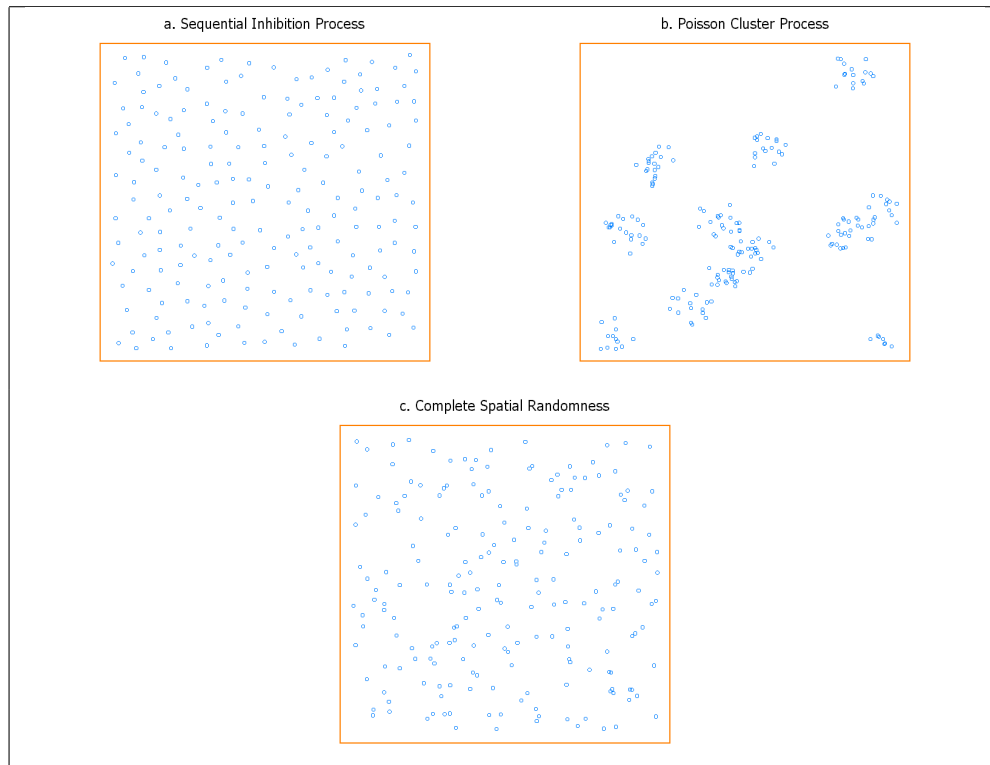


Figure 1.1: Examples of Spatial Point Patterns.

1. REGULAR PROCESSES

The simplest type of regular process is one that disallows two events to be within a distance δ of each other [Cressie, 1993]. Other subclasses of regular processes are listed by Cressie (1993) and credited to Matern (1960), Stoyan and Stoyan (1980), and Bartlett (1974). An example of a regular pattern, a sequential inhibition process [Diggle, 1976], is shown in Figure 1.3.2a. Two hundred events were generated using an inhibition radius of $\delta = 0.05$ on a unit square.

2. AGGREGATED PROCESSES

Aggregated, or clustered, processes include the Poisson cluster process, the Neyman-Scott process, and the Cox process. A general aggregated point pattern can be thought of a parent-child process where children are dispersed around a parent event. The Poisson cluster process is generated in such a manner by first obtaining parent events from an inhomogeneous Poisson process with mean measure μ_p , where μ_p is the expected number of parents. Each parent event produces a random number of offspring positioned around the parent according to some bivariate probability density. The parent events are then removed leaving only the offspring. Figure 1.3.2b shows an example of two-hundred events in a Poisson cluster process on a unit square with $\mu_p = 15$ and a radius of 0.075 for dispersing the child events according to a standard bivariate normal distribution.

3. COMPLETE SPATIAL RANDOMNESS

A Complete Spatial Random (CSR) process is one that generates events uniformly and independently in a region B with area $|B|$. The number of events $N(A)$, $A \subseteq B$, follows a Poisson distribution with mean $\lambda|A|$, where λ is the average number of events per unit area. Further, given n events $\mathbf{s}_i \in A$, the \mathbf{s}_i are independent realizations from a uniform distribution on A . Figure 1.3.2c is a CSR process with $n = 200$. Note that conditioning on n yields a Binomial process.

The importance of the CSR process lies in the fact that it is often used as a null hypothesis for testing a spatial point pattern. Under CSR, a spatial point pattern has no structure and thus failing to reject such a hypothesis warrants no further examination of the data [Diggle, 1983]. Thus, concluding a spatial point pattern is CSR implies uniformity of events ($E[N(A)] = \lambda|A|$) as well as independence ($\text{cov}[N(A), N(B)] = 0$ if $A \cap B = \emptyset$). It follows then that a test for CSR acts as a dividing hypothesis between regular and aggregated processes.

1.4 Spatiotemporal Point Processes

Spatiotemporal point processes will be considered as a hybrid of spatial and temporal components. Extending the definition of $Z(\mathbf{s})$ in (1.3.1) to include time, we obtain the following definition of a spatiotemporal point process:

$$\{Z(\mathbf{s}, t) : \mathbf{s} \in D(t) \subset \mathfrak{R}^2, t \in T\}, \quad (1.4.1)$$

where $D(t)$ is the spatial index at time t . Notice that a spatiotemporal process is not a three-dimensional process, e.g. $\{Z(\mathbf{s}) : \mathbf{s} \in D \subset \mathfrak{R}^3\}$, but a composite of a spatial and temporal process. This distinction is critical, since time flows unidirectionally, whereas space is not directed.

Spatiotemporal point processes have been studied thoroughly in the context of earthquake data. Ogata (1999) wrote a summary paper of parametric, maximum likelihood techniques. Choi and Hall (1999, 2000) added nonparametric estimators of the intensity function using a kernel estimator approach and discuss asymptotic theory for many of the parametric estimators.

Rathbun and Cressie (1994) discuss spatiotemporal point processes in the context of tree growth. In their paper, they present methods of parametric estimation by splitting the process into three components: a spatial birth process, a spatial growth process, and a space-time survival process.

There also exists literature on spatiotemporal processes for lattice and geostatistical data. See, for example, Kooperberg and O'Sullivan (1996) and Haas (1995). Haas (1995) develops the idea of a spatiotemporal covariance function through the construction of spatiotemporal cylinders for use in prediction of wet sulfate deposition (a geostatistical process). Essentially, Haas creates a cylinder centered at location $\mathbf{s}_0 = (x_0, y_0)$ with length $m_T = t_U - t_L$ for a user-defined time interval (t_L, t_U) . He then uses n_c , the number of points located inside the cylinder, to make a prediction of wet sulfate deposition at the location \mathbf{s}_0 . We will take a

similar three-dimensional approach for construction of a spatiotemporal intensity measure. Unfortunately, the literature lacks a more general approach to the analysis of the process (1.4.1). In this dissertation we propose exploratory tools through modifications of the first- and second-order intensity functions. An extension to Ripley's K -function will also be given. Finally, we will provide tools to model the spectra of the temporal and spatial components through an extension of Bartlett's auto-covariance function.

1.4.1 Types of Spatiotemporal Point Processes

Before analyzing a spatiotemporal data set we must classify the process that created the data. We have separated these processes into four distinct scenarios: the earthquake process, the explosion process, the birth-death process, and point patterns sampled in time (Figure 1.4.1). All four occur in nature, but to date no generic methods that incorporate the behaviors of each have been suggested.

1. EARTHQUAKE PROCESSES

The type of data that would be observed from an earthquake process corresponds to the location \mathbf{s} where an event occurred at time t . Characteristic for this process is that it is orderly in both space and time: only one event can occur at a particular location and time. Analysis of earthquake processes are discussed extensively in the geophysical literature [Rathbun 1996; Ogata 1999; Choi and Hall 1999]. Depending on whether we record “when and where” an earthquake occurred or also its magnitude, the process is simple or marked.

Cressie (1993, p. 720) refers to this type of space-time process as a space-time shock process because events occur simultaneously over time and space. The realization of such a process consists of locations $\mathbf{s}_i \in D^*$ at times $t_i \in T^*$, $i = 1, 2, \dots$, where D^* and T^* are realizations of a particular point pattern. Integration of events over a time interval $[0, t]$ results in a spatial point pattern that can be analyzed by standard

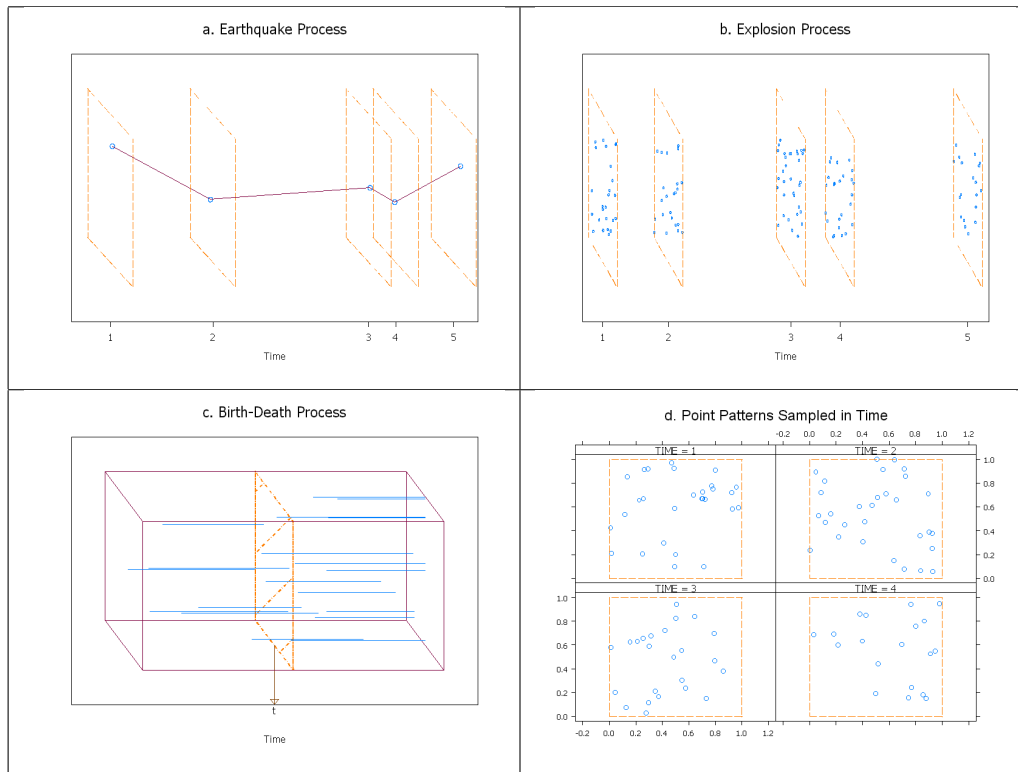


Figure 1.2: Examples of Spatiotemporal Point Patterns.

methods for such data.

Cressie (1993) suggests that this type of space-time process can be viewed as a marked spatial point process with mark space T^* . This in turn suggests a simple method for simulating such processes.

2. EXPLOSION PROCESSES

The basic explosion process combines a point process in space with a point process in time. Realizations of such a process consist of locations $\mathbf{s}_{i1}, \dots, \mathbf{s}_{in_i} \in D^*$ at times $t_i \in T^*$. The name relates to the type of data that might be observed from this process. At each time t a scatter of points with intensity $\lambda(\mathbf{s})$ is observed. Furthermore, the explosions occur as a point process with intensity $\lambda(t)$. In other words, a temporal event triggers the generation of a spatial point pattern. One example of such a process is when temporal events occur completely at random and $Z(\mathbf{s}_i, t_i \in T^*)$ is a sequential

inhibition process.

3. BIRTH-DEATH PROCESSES

This process is typically used to model objects that are born at some random location and live for a random time. Cressie (1993, p. 720) refers to these as space-time survival point processes. See, for example, Rathbun and Cressie's (1994) analysis of longleaf pines in Southern Georgia. Realizations of birth-death processes often consist of locations of events at fixed points in time t_1, \dots, t_n . Key to these processes is that events remain at the same location during their lifetime, in contrast to, e.g., a Brownian motion where particles move through a volume.

4. POINT PATTERNS SAMPLED IN TIME

This process consists of T spatial point patterns observed at equally or unequally spaced time intervals. In contrast to the explosion process where $t_i \in T^*$ represent a complete "mapping" of the time points at which temporal events occurred, the sample times in a sequence of sampled point patterns are fixed by a probability or non-stochastic sample design. At each time point the spatial locations of events are completely recorded in the domain of interest, i.e., the spatial point pattern is mapped.

A sampled point pattern can be indistinguishable from a birth-death process with fixed points in time. Whereas birth-death processes are excellent models to describe the survival of stationary objects, a sampled point pattern can also be thought of as recording the locations of non-stationary objects that move through space and time. If an event is observed at locations \mathbf{s}^* at time t_{i-1} but not at t_i could be due to the death of a stationary object that lived at \mathbf{s}^* at t_{i-1} or the displacement of a non-stationary object that occupies a different location at t_i . Combinations of these processes are obvious. In the study of animals, for example, individuals are born between t_{i-1} and t_i , their locations are observed at times $t_i, t_{i+1}, \dots, t_{j-1}$, die between times t_{j-1} and t_j and are no longer recorded at sample times $t \geq t_j$.

The inference of interest in sampled point patterns depends on the nature of the process

as pure birth-death, continuous motion, or a mixture thereof. Regardless of the genesis, however, studying the inter-relationship among point patterns over time is common to all sampled point patterns.

An extension of the CSR model to include time will be known as the Complete Spatiotemporal Randomness (CSTR) model. As with CSR, the underlying process is void of structure in space as well as time [Cressie, 1993]. The methods we put forth to analyze spatiotemporal point patterns use the CSTR model as a reference in hypothesis testing. Any of these four types of spatiotemporal point patterns described above can be formulated as realizations of suitably chosen CSTR models.

1.4.2 Previous Work in Spatiotemporal Point Processes

Rathbun (1996) gives an expression for what he calls the complete intensity function for use in the analysis of earthquake data which depends on the locations and times of all past events in $(-\infty, t)$. Rathbun further defines a conditional intensity by restricting the intensity measure to include past events occurring in the time interval $(0, t)$.

The intensity measures defined by Rathbun (1996), and also found in Choi and Hall (1999) and Ogata (1999), require the process to be orderly in space and time (e.g. earthquake processes, see Section 1.4.1). As will be shown in Chapter 3, our spatiotemporal intensity measures are similar to those of Rathbun (1996) but apply to a broader class of processes. We further define several spatiotemporal intensities, including different definitions of conditional spatiotemporal intensity.

Choi and Hall (2000) introduce a kernel estimator for spatiotemporal intensity for earthquake data given by

$$\hat{\lambda}_{b_t, b_s}(\mathbf{s}, t) = \frac{1}{b_t b_s^2} \sum_{i=1}^n \kappa_t \left(\frac{t - t_i}{b_t} \right) \kappa_s \left(\frac{\mathbf{s} - \mathbf{s}_i}{b_s} \right), \quad (1.4.2)$$

where b_s and b_t are bandwidths, not necessarily identical, and the kernel functions $\kappa_s(\cdot)$ and

$\kappa_t(\cdot)$ are user-specified, and again, are not necessarily the same for the spatial and temporal component. Choi and Hall do not account for edge effects in their estimator as Cressie (1993) and Diggle (1983) suggest.

Mugglestone and Renshaw (1996a) incorporate a time component into a spatial periodogram through computation of the amplitude, phase, coherency, and gain spectra between two spatial patterns. This approach seem reasonable for two patterns, but is not easily extendable to a series of point patterns. Their subsequent analysis of the co-spectrum related the two point patterns but made no inference about the role of time in the process.

1.5 An Example - The Red-cockaded woodpecker



Figure 1.3: The Red-cockaded Woodpecker.

The methods described in this dissertation will be applied to data collected by the Department of Biology at Virginia Tech. The data collected are on the nesting habits of the red-cockaded woodpecker, an endangered species found in the longleaf pine forests of the southeastern United States (Figure 1.5). The red-cockaded woodpecker is atypical of most woodpeckers in that they build nesting cavities in living pine trees; a process that can take

as many as three years for one cavity. Furthermore, they are known as cooperative breeders because of their tendency to remain in clusters for several years and through several mating seasons [Walters et al., 1998].

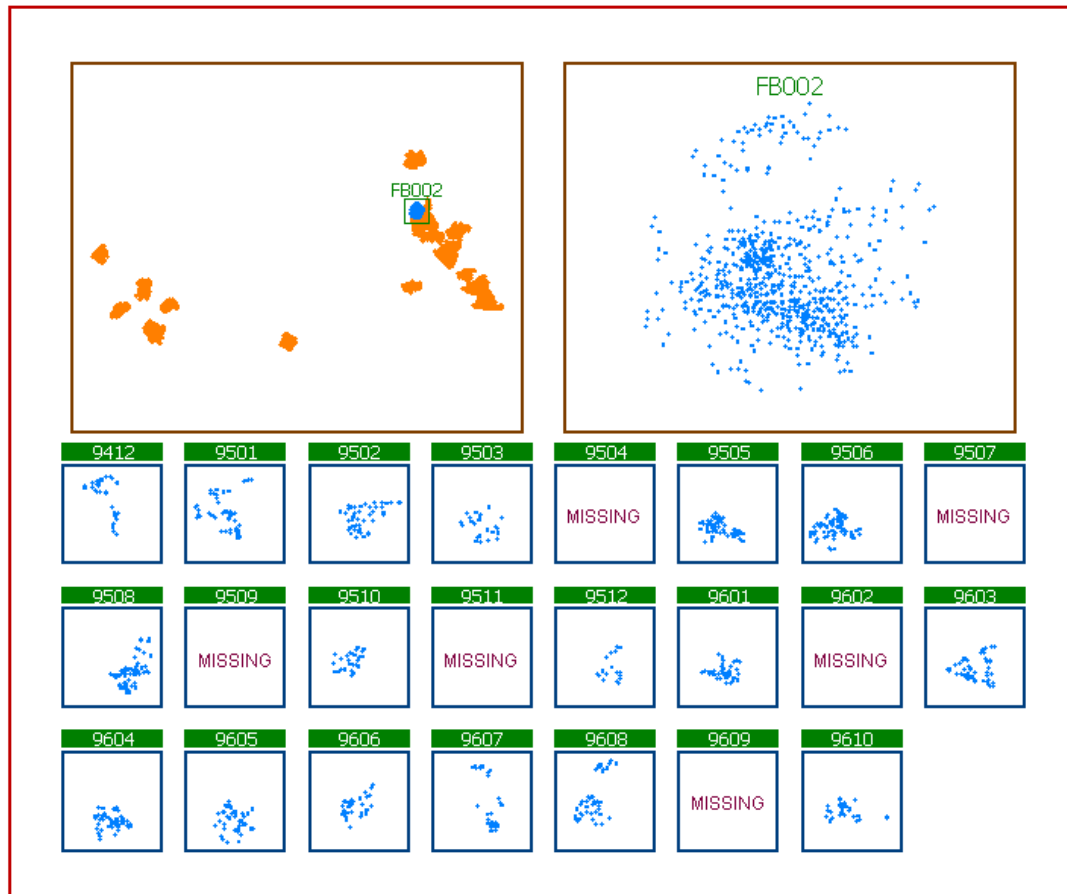


Figure 1.4: Location of birds from FB002 from the Red-cockaded woodpecker data from December 1994 (9412) to October 1996 (9610).

Thirty clusters (families) of birds were followed in the Fort Bragg area of North Carolina over a 23-month period (December 1994 to October 1996) [Figure 1.5, upper left]. For seventeen of the twenty-three months, one bird from each cluster was selected and observed for a day. For six of the months, no data were collected. The location of the identified bird from each cluster was recorded at eight-minute intervals [Figure 1.5, bottom]. This was done in an effort to obtain an estimate of the homerange of the cluster, the area in which an animal

performs its normal activities [Burt, 1943]. Figure 1.5 (upper right) shows the locations at which cluster FB002 was observed integrated over the entire twenty-three month period. In all, 675 events in FB002 were recorded over a 23 month period on an area 3826×4706 ft² in size. However, prior to any analysis the width of the bounding box was extended so that analysis was performed on a 4706×4706 ft² square rather than the latter rectangle. This was done so that a clustering radius could be determined in the final analysis without any concerns for scaling. Comparison of the analyses based on a bounding rectangle versus a bounding square revealed no qualitative differences in the outcomes.

In Chapter 2, we will analyze the FB002 cluster entirely in a spatial context. We will introduce current methods used to explore the first- and second-order properties of a spatial point process using the FB002 cluster as an example. Furthermore, we will build upon these methods to extract more information about isotropic processes. As with most current analyses of this data set, the inherent temporal component will be ignored for the time being in order to highlight some of the methods of analyzing spatial point patterns. After introducing some of the mathematical properties of spatiotemporal point processes in Chapter 3, we will return to the woodpecker data and conduct inferences in both space and time.

Chapter 2

Spatial Point Patterns

This chapter presents some of the theory and methodology of inference for spatial point patterns. Much of the analysis of point patterns found in the literature and texts on spatial statistics places emphasis on the analysis of point patterns in the spatial domain. We introduce this popular approach as well as the less utilized approach of spectral analysis and discuss the comparative merits and demerits. Analysis of first-order properties commonly uses intensity estimators. Second-order analysis of point patterns is explored in both the spatial domain and frequency domains.

2.1 Intensity Measures of Spatial Point Patterns

Analysis of spatial data is covered extensively in the literature. For geostatistical and lattice data where D is fixed, first-order (mean) properties are modeled by $E[Z(\mathbf{s})] = \mu(\mathbf{s})$. Here, estimates of $\mu(\mathbf{s})$ are obtained for example through random field models for geostatistical data or median polishing for lattice data and predictions of $Z(\mathbf{s})$ through kriging methods. For more details on mean estimation or trend analysis of geostatistical and lattice spatial data see Cressie (1993). Second-order (covariance) properties of geostatistical are modeled through

the covariogram function $c(\mathbf{s}_i - \mathbf{s}_j) = \text{cov}[Z(\mathbf{s}_i), Z(\mathbf{s}_j)]$ or the semivariogram $\gamma(\mathbf{s}_i - \mathbf{s}_j) = \frac{1}{2}\text{var}[Z(\mathbf{s}_i) - Z(\mathbf{s}_j)]$. For a weakly stationary spatial process a simple relationship converts $c(\mathbf{s}_i - \mathbf{s}_j)$ to $\gamma(\mathbf{s}_i - \mathbf{s}_j)$, namely,

$$\gamma(\mathbf{s}_i - \mathbf{s}_j) = c(\mathbf{0}) - c(\mathbf{s}_i - \mathbf{s}_j).$$

For lattice data, spatial dependency is modeled through the conditional and simultaneous autoregressive schemes closely related to autoregressive structures in time series.

For point patterns, the first and second-order intensities are used to determine the mean and dependency structure of the data. The intensity of a spatial point process is defined as the expected number of points per unit area,

$$\lambda(\mathbf{s}) = \lim_{|ds| \rightarrow 0} \left\{ \frac{E[N(ds)]}{|ds|} \right\}. \quad (2.1.1)$$

Here ds is an infinitesimal region containing the site \mathbf{s} , $N(ds)$ represents the number of points located in ds , and $|ds|$ is the area (volume) of the region ds . Throughout, the notation $|\cdot|$ will represent the Lebesgue measure on the spatial region D . The second-order intensity $\lambda_2(\mathbf{s}_i, \mathbf{s}_j)$ contains information about the stochastic dependence between events in two regions. Although $\lambda_2()$ is akin to $c()$ defined previously, it is not a covariance function. The second-order intensity function is also defined as a limit,

$$\lambda_2(\mathbf{s}_i, \mathbf{s}_j) = \lim_{|ds_i|, |ds_j| \rightarrow 0} \left\{ \frac{E[N(ds_i)N(ds_j)]}{|ds_i||ds_j|} \right\}. \quad (2.1.2)$$

The notation in (2.1.1) and (2.1.2) is due to Diggle (1983).

2.1.1 Second-Order (Weak) Stationarity

Stationarity of a stochastic process in space implies that the joint probability distribution of a collection of events $\{Z(\mathbf{s}) : \mathbf{s} \in D\}$ is invariant under translation. That is, the distribution

function

$$F_N(\mathbf{s}) \equiv F_N(\mathbf{s} - \mathbf{u})$$

of the counting measure N on a collection of events in A will involve \mathbf{s} only through the differences $\mathbf{s} - \mathbf{u}$. As in time series, this type of stationarity requirement is too strict for most analyses. Instead, in order to make progress with inferences we will only require second-order (or weak) stationarity. Second-order stationarity requires only that the joint probability distributions for any collection of events be identical only up to the first two moments. Thus, stationarity implies second-order stationarity, but not vice versa. (Note: Throughout this dissertation use of the term “stationary” implies “second-order stationary.”)

A spatial point process is second-order stationary if $\lambda(\mathbf{s}) \equiv \lambda$ and $\lambda_2(\mathbf{s}_i, \mathbf{s}_j) \equiv \lambda_2(\mathbf{s}_i - \mathbf{s}_j) = \lambda_2(\mathbf{h}_{ij})$ [Cressie, 1993]. This is analogous to the definition of second-order stationarity in the time series context in that the mean is constant and the covariance function is invariant under translation. If the covariance function is invariant under rotation as well as translation, then the second-order intensity can be written as $\lambda_2(h_{ij})$ where h_{ij} is the Euclidean distance between events \mathbf{s}_i and \mathbf{s}_j . If the latter is true the process is said to be *isotropic*, a concept foreign to time series analysis.

A second-order intensity function is said to exhibit *geometric anisotropy* if

$$\lambda_2(\mathbf{h}) = \lambda_2^0(\|\mathbf{Q}\mathbf{h}\|), \quad (2.1.3)$$

where λ_2^0 is an isotropic second-order intensity function and \mathbf{Q} is a positive definite matrix [Vecchia, 1985]. A more precise definition of (2.1.3) is given in Section 2.3. This is analogous to a transformation of an isotropic semi-variogram for continuous spatial data [Chilès and Delfiner, 1999].

2.1.2 Reduced Second-Order Intensity

The second-order intensity function does not have any physical interpretation as it relates to data. Ripley (1976) offers an interpretable measure for the dependence in isotropic stationary point processes by way of the K -function which is defined by

$$\lambda K(h) = E[\text{number of extra events within a distance } h \text{ of an arbitrary event}]. \quad (2.1.4)$$

Cressie (1993) also refers to a more general K -function as the *reduced second-order measure*.

If we assume the process is completely random then the extra number of events within a distance h will be uniform on a disc. From this we see that

$$\begin{aligned} \lambda K(h) &= \int_0^{2\pi} \int_0^h \{\lambda_2(x)/\lambda\} x dx d\theta \\ &= \frac{2\pi}{\lambda} \int_0^h \lambda_2(x) x dx, \end{aligned} \quad (2.1.5)$$

and as a result,

$$\lambda_2(h) = \frac{\lambda^2}{2\pi h} \frac{\partial K(h)}{\partial h}. \quad (2.1.6)$$

The K -function has many appealing features not shared by $\lambda_2(h)$, such as its invariance to random thinning, physical interpretation, and simple estimation [Cressie, 1993]. Several approaches for estimation and interpretation of the K -function are given by Cressie (1993) and Diggle (1983). However, it must be noted that $K(h)$ is not unique for similar reasons that disallow identification of a distribution from only the first two moments. Different point processes can produce identical K -functions [Baddeley and Silverman, 1984]. Furthermore, though the K -function is used to analyze second-order properties of a spatial point pattern, it cannot distinguish between deviations from CSR due to lack of uniformity or lack of independence of events. However, since $K(h)$ is defined only for first-order stationary processes,

uniformity is a requirement of K -function analysis.

Under CSR, $\lambda_2(h) \equiv \lambda^2$, thus (2.1.5) reduces to

$$K(h) \stackrel{CSR}{=} \pi h^2. \quad (2.1.7)$$

Testing a point pattern for CSR can be accomplished by comparing the empirical K -function to πh^2 . Quite often, inference is based on the L -function defined by

$$L(h) = \sqrt{K(h)/\pi} \stackrel{CSR}{=} h, \quad (2.1.8)$$

and a plot of $L(h) - h$ versus h is obtained.

Because the probability distribution of the K -function (or the L -function) is intractable, inference about a process is based on simulated K -functions. An envelope is constructed by simulating the hypothesized point process B times and constructing the K -function for a set of distances h . For every simulation $(K_{\min}(h), K_{\max}(h))$ is stored. The upper and lower envelopes are then overlaid on the observed K -function $\widehat{K}(h)$.

Inference can be obtained by comparing the observed K -function to the simulated envelope. If $\widehat{K}(h) > \overline{K}_{\text{sim}}(h)$ then the number of events within a distance h of an arbitrary event is greater than expected under the hypothesized process. If the hypothesized process is CSR then this would imply an aggregated process if h is small or a regular process if h is large. Conversely, if $\widehat{K}(h) < \overline{K}_{\text{sim}}(h)$ then the number of events within a distance h of an arbitrary event is less than expected under the hypothesized process. Reversing our conclusion we would infer that the observed process is regular if h is small or aggregated if h is large. If $\widehat{K}(h_0) > K_{\max}(h_0)$ or $\widehat{K}(h_0) < K_{\min}(h_0)$, the hypothesis is rejected for that particular distance.

Alternatively, empirical p-values can be obtained by ranking the statistics calculated from the observed K -function against the B simulations through the Cramér-von Mises-type statistic.

Specifically, if we would like to compare our observed point pattern to CSR we compute

$$k_{\text{obs}} \equiv \int_0^{h_{\text{max}}} \left\{ \sqrt{\widehat{K}(h)} - \sqrt{K_0(h)} \right\}^2 dh, \quad (2.1.9)$$

where \widehat{K} is the estimated K -function of the observed pattern, $K_0(h) = \pi h^2$ is the K -function under the hypothesis of CSR, and h_{max} is the maximum distance for which $\widehat{K}(h)$ is computed [Cressie, 1993]. Thus the statistic k_{obs} leads to a two-sided hypothesis for which large values would be the observed for point pattern exhibiting either regularity or clustering. Similarly, we would compute (2.1.9) for all B simulated processes

$$k_i \equiv \int_0^{h_{\text{max}}} \left\{ \sqrt{\widehat{K}_i^{\text{MC}}(h)} - \sqrt{K_0(h)} \right\}^2 dh \quad i = 1, 2, \dots, B,$$

where $\widehat{K}_i^{\text{MC}}(h)$ is the estimated K -function for the i^{th} simulated process. The observed process deviates from CSR for large values of (2.1.9). An empirical p-value p_{emp} is obtained by ranking k_{obs} with all the k_i and determining the percentage of k_i 's larger than k_{obs} . Namely, if $r_k = \text{rank}(k_{\text{obs}})$ then

$$p_{\text{emp}} = \frac{B + 1 - r_k}{B}. \quad (2.1.10)$$

Thus, we would reject the hypothesis of CSR if (2.1.10) is less than some significance level α [Cressie, 1993]. An example of L -function analysis on the point processes shown in Figure 1.3.2 as well as the FB002 cluster from the woodpecker data is given in Section 2.1.3.

2.1.3 Estimation of Intensities

The three most common techniques for estimating the first-order intensity $\lambda(\mathbf{s})$ are: 1) the Basic estimator, which assumes $\lambda(\mathbf{s}) \equiv \lambda$ for some constant λ ; 2) the Binning estimator, which is simply a smoothed two-dimensional histogram; and 3) the Kernel estimator, that employs methods from kernel density estimation to obtain an estimate of $\lambda(\mathbf{s})$. Estimators

of intensity over a study region A are given by:

$$\text{Basic} : \hat{\lambda} = \frac{n}{|A|} \quad (2.1.11)$$

$$\text{Binning} : \hat{\lambda}(\mathbf{s}) = \sum_{j=1}^{\# \text{ bins}} \kappa \left(\frac{\mathbf{s} - \mathbf{s}_j}{b} \right) \sum_{i=1}^n \frac{I(\mathbf{s}_i \in d\mathbf{s}_j)}{|d\mathbf{s}_j|} \quad (2.1.12)$$

$$\text{Kernel} : \hat{\lambda}_b(\mathbf{s}) = \frac{1}{p_b(\mathbf{s})} \sum_{i=1}^n \kappa \left(\frac{\mathbf{s} - \mathbf{s}_i}{b} \right) \quad (2.1.13)$$

In (2.1.12), $I(\cdot)$ is an indicator function, $|d\mathbf{s}_j|$ the size of the bin centered at \mathbf{s}_j , $\kappa(\cdot)$ is a kernel function, and b is an bandwidth. In (2.1.13), $\kappa(\cdot)$ is a kernel function satisfying standard conditions [Scott, 1992], b is a bandwidth, and p_b is an edge-correction factor given by

$$p_b(\mathbf{s}) = \int_A \kappa \left(\frac{\mathbf{s} - \mathbf{u}}{b} \right) d\mathbf{u} \quad \mathbf{s} \in A.$$

Cressie (1993) and Scott (1992) provide details on the choice of $\kappa(\cdot)$ and suggestions for selecting the bandwidth b .

Cressie (1993) offers five different estimators for the reduced second-order measure, or the K -function, given by (2.1.5). All the estimators are presented with edge-corrections. The version included in the `S+SpatialStats` module is the K -function estimate first proposed by Ripley (1976) [Kaluzny et al. 1998]:

$$\hat{K}(h) = \hat{\lambda}^{-1} \sum_{i=1}^n \sum_{\substack{j=1 \\ i \neq j}}^n w_{ij}^{-1} I(\|\mathbf{s}_i - \mathbf{s}_j\| < h) / n. \quad (2.1.14)$$

Here, $I(\cdot)$ is an indicator function, $\hat{\lambda}$ is obtained by (2.1.11), and w_{ij} is an edge-correction weight defined by the proportion of the circumference of a circle centered at \mathbf{s}_i , passing through \mathbf{s}_j , that is inside the study region. Ripley (1981) showed that (2.1.14) is approximately unbiased if n and \hat{K} are independent, which is true if h is small. Ripley (1981) further suggests making h_{\max} one-half the circumradius of the bounding box so that approximate

unbiasedness is obtained. The latter rule-of-thumb is the default in the `S+SpatialStats` module.

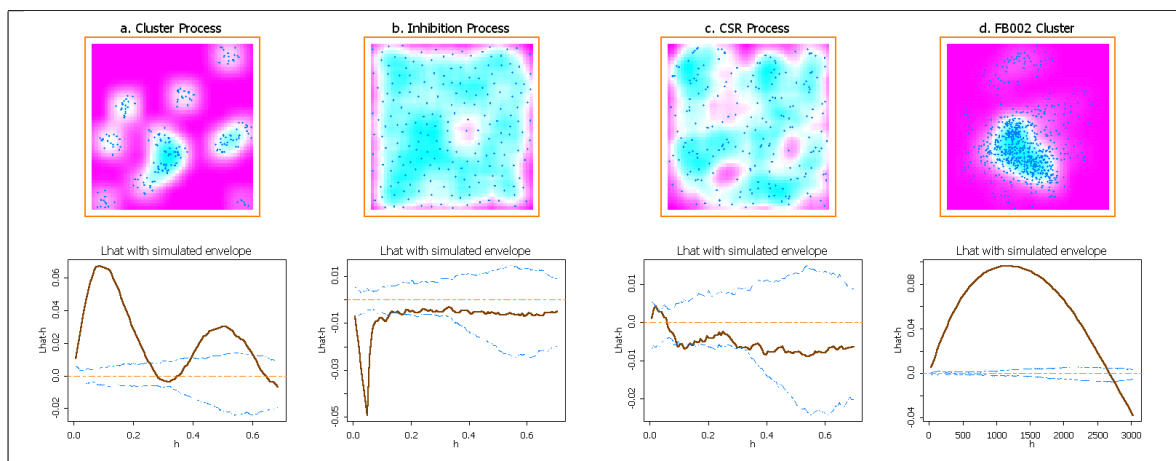


Figure 2.1: Intensity estimates and \widehat{L} -analysis for spatial point patterns for three simulated processes (a-c) and cluster FB002 from the woodpecker data (d).

Figure 2.1.3 shows the analysis of the three simulated processes introduced in Figure 1.3.2 as well as the FB002 cluster of the woodpecker data shown in Figure 1.5. The top row are intensity estimates based on the kernel estimator given by (2.1.13) using

$$\kappa(u_x, u_y) = 0.75(1 - u_x^2)(1 - u_y^2)I(|u_x| \leq 1 \cap |u_y| \leq 1),$$

the bivariate Epanechnikov kernel [Scott, 1992], and bandwidth $b = 0.15$. The bottom row is the L -analysis for each of the point patterns with simulated envelopes based on $B = 100$ CSR point patterns. The empirical p-value based on Cramér-von Mises criteria given in (2.1.9) for testing the hypothesis of CSR for each of the patterns is in Table 2.1. For this analysis, the maximum distance used for estimating the K -function was $\sqrt{2}/2 \approx 0.6$ for the simulated processes and $\sqrt{4706^2 + 4706^2}/2 \approx 3327$ ft for the FB002 cluster. Using a significance level of $\alpha = 0.05$ we see the only pattern that fails to reject the hypothesis of CSR is the CSR process itself. Though the p-value for the CSR process is smaller than would typically expected, this can most likely be attributed to the seed chosen to generate the observed pattern. However, other factors that may arise from use of this statistic are

the choice of h_{\max} or the bias of the K -function due to edge effects.

PROCESS	VALUE	B	r_k	p_{emp}
CLUSTER	0.00215	100	101	0.00
INHIBITION	0.00023	100	100	0.01
CSR	0.00008	100	88	0.13
FB002	0.00811	100	101	0.00

Table 2.1: Results of \hat{L} -analysis for simulated and real point patterns in Figure 2.1.3.

2.1.4 Auto-covariance of an Orderly Spatial Point Process

Bartlett (1964) approached the problem of finding the auto-covariance function of an orderly spatial point process in the following manner. Consider the counting measure $N(A)$ in a spatial point process, where $N(A)$ is the number of points in the region A . For a process to be orderly, in which only one event can occur at any arbitrary location, we require (1.3.3). Thus, for a second-order stationary spatial point process (see Section 2.1.1) we have

$$\lim_{|ds| \rightarrow 0} \frac{E\{[N(ds)]^2\}}{|ds|} = \lim_{|ds| \rightarrow 0} \frac{E\{N(ds)\}}{|ds|} = \lambda, \quad (2.1.15)$$

for some constant intensity λ .

Given the first- and second-order intensities in (2.1.1) and (2.1.2), respectively, and the assumption of second-order stationarity, the complete covariance density function for $N(ds)/|ds|$ is

$$\lim_{|ds_i|, |ds_j| \rightarrow 0} \frac{\text{cov}[N(ds_i), N(ds_j)]}{|ds_i||ds_j|} = v(\mathbf{s}_i - \mathbf{s}_j) + \lambda\delta(\mathbf{s}_i - \mathbf{s}_j), \quad (2.1.16)$$

where $v(\mathbf{s}_i - \mathbf{s}_j)$ is the auto-covariance density function defined by

$$\begin{aligned} v(\mathbf{s}_i - \mathbf{s}_j) &= \lim_{|ds_i|, |ds_j| \rightarrow 0} \frac{E[N(ds_i)N(ds_j)]}{|ds_i||ds_j|} - \left[\lim_{|ds_i| \rightarrow 0} \frac{E[N(ds_i)]}{|ds_i|} \right] \left[\lim_{|ds_j| \rightarrow 0} \frac{E[N(ds_j)]}{|ds_j|} \right] \\ &= \lambda_2(\mathbf{s}_i - \mathbf{s}_j) - \lambda^2 \end{aligned} \quad (2.1.17)$$

and $\delta(\mathbf{x} - \mathbf{x}')$ is the (two-dimensional) Dirac delta-function defined by

$$\delta(\mathbf{x} - \mathbf{x}') = \begin{cases} \infty & \mathbf{x} = \mathbf{x}' \\ 0 & \mathbf{x} \neq \mathbf{x}' \end{cases}. \quad (2.1.18)$$

The complete covariance density given by (2.1.16) is derived from the following

$$\begin{aligned} \lim_{|ds_i|, |ds_j| \rightarrow 0} \frac{\text{cov}[N(ds_i), N(ds_j)]}{|ds_i||ds_j|} &= \begin{cases} \lim_{|ds_i|, |ds_j| \rightarrow 0} \frac{E[N(ds_i)N(ds_j)]}{|ds_i||ds_j|} \\ - \left[\lim_{|ds_i| \rightarrow 0} \frac{E[N(ds_i)]}{|ds_i|} \right] \left[\lim_{|ds_j| \rightarrow 0} \frac{E[N(ds_j)]}{|ds_j|} \right] & \text{for } \mathbf{s}_i \neq \mathbf{s}_j \\ \lim_{|ds_i| \rightarrow 0} \frac{E[N(ds_i)^2]}{|ds_i|^2} - \left[\lim_{|ds_i| \rightarrow 0} \frac{E[N(ds_i)]}{|ds_i|} \right]^2 & \text{for } \mathbf{s}_i = \mathbf{s}_j \end{cases} \\ &= \begin{cases} v(\mathbf{s}_i - \mathbf{s}_j) & \text{for } \mathbf{s}_i \neq \mathbf{s}_j \\ \lim_{|ds_i| \rightarrow 0} \frac{\lambda}{|ds_i|} - \lambda^2 & \text{for } \mathbf{s}_i = \mathbf{s}_j \end{cases}. \end{aligned} \quad (2.1.19)$$

Taking the limit in (2.1.19) yields an infinite variance for $N(ds)/|ds|$ which is the reason behind the Dirac delta notation in (2.1.16).

2.2 Spectral Representation and Spatial Periodogram Analysis

A spectral representation of spatial data similar to (1.1.3) is also used to identify frequencies of occurrences in all three types of spatial data. The relative merits for analyzing spatial data in the frequency domain are similar to those of the frequency domain analysis in time series. One further note is that defining a valid covariogram is not needed, making spectral analysis less parametric.

For second-order stationary spatial process, the spectral representation of the auto-covariance

function, $c(\mathbf{h})$, can be written as

$$c(\mathbf{h}) = \int_{-\infty}^{\infty} e^{i\boldsymbol{\omega}'\mathbf{h}} G(d\boldsymbol{\omega}), \quad (2.2.1)$$

where $\mathbf{h} = \mathbf{s}_i - \mathbf{s}_j$ is the absolute distance between \mathbf{s}_i and \mathbf{s}_j , $\boldsymbol{\omega}'\mathbf{h} = \omega_x h_x + \omega_y h_y$, and $G(\boldsymbol{\omega})$ is the spectral distribution function [Cressie, 1993]. If $G(d\boldsymbol{\omega}) = g(\boldsymbol{\omega})d\boldsymbol{\omega}$ then we can define $g(\boldsymbol{\omega})$ as the spectral density of the auto-covariance function. Note the similarities to (1.1.3) and (1.2.3).

Much of the theory developed for spectral analysis of time series can be used to study the spectrum of a spatial process. However, most of the literature defines the spectral density of a spatial process for lattice or geostatistical data. The literature is sparse for spectral analysis of point patterns.

Given a stationary spatial point process, the inverse Fourier transform of (2.1.16) is given by

$$v(\mathbf{h}) + \lambda\delta(\mathbf{h}) = \int_{-\infty}^{\infty} e^{i\boldsymbol{\omega}'\mathbf{h}} G(d\boldsymbol{\omega}), \quad (2.2.2)$$

where $G(d\boldsymbol{\omega})$ is given by (2.2.1). We can define the Fourier transform of (2.1.16) by

$$\begin{aligned} g(\boldsymbol{\omega}) &= \frac{1}{(2\pi)^2} \left[\int_{-\infty}^{\infty} e^{-i\boldsymbol{\omega}'\mathbf{h}} [v(\mathbf{h}) + \lambda\delta(\mathbf{h})] d\mathbf{h} \right] \\ &= \frac{1}{(2\pi)^2} \left[\int_{-\infty}^{\infty} e^{-i\boldsymbol{\omega}'\mathbf{h}} v(\mathbf{h}) d\mathbf{h} + \lambda \int_{-\infty}^{\infty} e^{-i\boldsymbol{\omega}'\mathbf{h}} \delta(\mathbf{h}) d\mathbf{h} \right] \\ &= \frac{1}{(2\pi)^2} \left[\int_{-\infty}^{\infty} e^{-i\boldsymbol{\omega}'\mathbf{h}} v(\mathbf{h}) d\mathbf{h} + \lambda \right], \end{aligned} \quad (2.2.3)$$

where \int is a two-dimensional integral and $\boldsymbol{\omega}'\mathbf{h} \equiv \omega_x h_x + \omega_y h_y$. This corresponds to the expression given by (1.2.4).

Estimation of the spectral density is obtained through the periodogram. From (2.2.3) the

periodogram can be obtained by $I(\boldsymbol{\omega}_{pq}) = J(\boldsymbol{\omega}_{pq})\bar{J}(\boldsymbol{\omega}_{pq})$, where

$$J(\boldsymbol{\omega}_{pq}) = \frac{1}{2\pi} \sum_{j=1}^n Z(\mathbf{s}_j) \exp \{i\boldsymbol{\omega}'_{pq} \mathbf{L}^{-1} \mathbf{s}_j\}, \quad (2.2.4)$$

$\bar{J}(\boldsymbol{\omega}_{pq})$ is the complex conjugate of $J(\boldsymbol{\omega}_{pq})$, $\boldsymbol{\omega}'_{pq} = [2\pi p \quad 2\pi q]$ for $p = 0, 1, 2, \dots$ and $q = 0, \pm 1, \pm 2, \dots$, \mathbf{s}_k is an arbitrary location, $Z(\mathbf{s}_k)$ is given by (1.3.1), and \mathbf{L} is a scaling matrix given by

$$\mathbf{L} = \begin{bmatrix} L_x & 0 \\ 0 & L_y \end{bmatrix}, \quad (2.2.5)$$

where $A = L_x L_y$ for a rectangular region A [Renshaw and Ford, 1983]. Note that the $\mathbf{L}^{-1} \mathbf{s}_k$ effectively scales the region A to the unit square, thus the estimate of λ under the second-order stationarity assumption is n . Thus the periodogram is given by

$$\begin{aligned} I(\boldsymbol{\omega}_{pq}) &= J(\boldsymbol{\omega}_{pq})\bar{J}(\boldsymbol{\omega}_{pq}) \\ &= \frac{1}{(2\pi)^2} \left(\sum_{k=1}^n \exp \{i\boldsymbol{\omega}'_{pq} \mathbf{L}^{-1} \mathbf{s}_k\} \right) \left(\sum_{j=1}^n \exp \{i\boldsymbol{\omega}'_{pq} \mathbf{L}^{-1} \mathbf{s}_j\} \right) \\ &= \frac{1}{(2\pi)^2} \sum_{j=1}^n \sum_{k=1}^n \exp \{-i\boldsymbol{\omega}'_{pq} \mathbf{L}^{-1} (\mathbf{s}_j - \mathbf{s}_k)\} \\ &= \frac{1}{(2\pi)^2} \sum_{j=1}^n \sum_{k=1}^n \exp \{-i\boldsymbol{\omega}'_{pq} \mathbf{L}^{-1} \mathbf{h}_{jk}\}, \end{aligned} \quad (2.2.6)$$

where $\mathbf{h}_{jk} = \mathbf{s}_j - \mathbf{s}_k$. The spatial periodogram given in (2.2.6) is asymptotically unbiased for (2.2.3) as $n \rightarrow \infty$ [Mugglestone and Renshaw, 1996a].

Analysis of point patterns in the frequency domain requires the study region A to be rectangular. Though this may not be a valid assumption no feasible alternative has ever been suggested. In practice, the study region A is assumed to be the smallest bounding box that contains all observed events.

Because no maximum (Nyquist) frequency exists for unequally spaced data, the choices of

p and q are left to the user. Mugglestone and Renshaw (1996b) suggest that $I(\boldsymbol{\omega}_{pq})$ need only be computed for $p = 0, \dots, 16$ and $q = -15, \dots, 16$ for $n < 100$, which will give details of $1/16$ units in the x - and y -directions. Note that $I(\boldsymbol{\omega}_{n-p,q}) = I(\boldsymbol{\omega}_{p,n-q})$, thus (2.2.6) need only be evaluated for $p > 0$ [Renshaw and Ford, 1983].

2.2.1 Distribution of the Spatial Periodogram

THEOREM 2.1 (DISTRIBUTION OF THE SPATIAL PERIODOGRAM)

Let $Z(\mathbf{s})$ be an orderly, second-order stationary spatial point process with probability distribution F and first two moments given by (2.1.15) and (2.1.16). Furthermore, let $Z(\mathbf{s})$ have a continuous spectral density $g(\boldsymbol{\omega})$ given by (2.2.3). Then, as $n \rightarrow \infty$, the periodogram (2.2.6) has a distribution given by

$$2 \frac{I(\boldsymbol{\omega}_{pq})}{g(\boldsymbol{\omega})} \xrightarrow{d} \chi_2^2 \quad \text{if } \boldsymbol{\omega}_{pq} \neq \mathbf{0} \quad (2.2.7)$$

and

$$2 \frac{I(\boldsymbol{\omega}_{pq}) - \frac{\lambda}{(2\pi)^2}}{g(\mathbf{0})} \xrightarrow{d} \chi_1^2 \quad \text{if } \boldsymbol{\omega}_{pq} = \mathbf{0}, \quad (2.2.8)$$

where \xrightarrow{d} represents convergence in distribution. Furthermore, as $n \rightarrow \infty$,

$$\text{cov}[2I(\boldsymbol{\omega}_{pq}), 2I(\boldsymbol{\omega}_{p'q'})] = \begin{cases} g^2(\boldsymbol{\omega}) & \text{if } \boldsymbol{\omega}_{pq} = \boldsymbol{\omega}_{p'q'} \\ 0 & \text{if } \boldsymbol{\omega}_{pq} \neq \boldsymbol{\omega}_{p'q'} \end{cases}.$$

PROOF OF THEOREM 2.1

Brillinger (1972) provides a proof of Theorem 2.1 for a point process in one-dimension. Mugglestone and Renshaw (1996b) extend the proof to two dimensions. The proof of (2.2.7) and (2.2.8) requires $n \rightarrow \infty$. *Q.E.D.*

COROLLARY 2.1 (DISTRIBUTION OF THE CSR PERIODOGRAM)

If $Z(\mathbf{s})$ is a CSR point pattern then as $n \rightarrow \infty$,

$$E[I(\boldsymbol{\omega}_{pq})] \stackrel{A}{=} \begin{cases} \frac{3}{8\pi^2}\lambda & \text{for } \boldsymbol{\omega}_{pq} = \mathbf{0} \\ \frac{1}{4\pi^2}\lambda & \text{for } \boldsymbol{\omega}_{pq} \neq \mathbf{0} \end{cases}$$

and

$$\text{var}[I(\boldsymbol{\omega}_{pq})] \stackrel{A}{=} \begin{cases} \frac{1}{16\pi^4}\lambda^2 & \text{for } \boldsymbol{\omega}_{pq} = \mathbf{0} \\ \frac{1}{32\pi^4}\lambda^2 & \text{for } \boldsymbol{\omega}_{pq} \neq \mathbf{0} \end{cases},$$

where $\stackrel{A}{=}$ represents asymptotic equality.

PROOF OF COROLLARY 2.1

If we assume the observed events are distributed as Poisson with intensity λ then $\lambda(\mathbf{s}) = \lambda$ and $\lambda_2(\mathbf{s}_i - \mathbf{s}_j) = \lambda^2$. Thus the complete covariance density given by (2.1.16) is

$$v(\mathbf{s}_i - \mathbf{s}_j) + \lambda\delta(\mathbf{s}_i - \mathbf{s}_j) = \underbrace{\lambda_2(\mathbf{s}_i - \mathbf{s}_j) - \lambda^2}_{=\lambda^2} + \lambda\delta(\mathbf{s}_i - \mathbf{s}_j) = \lambda\delta(\mathbf{s}_i - \mathbf{s}_j).$$

This implies the covariance between two events distance $\mathbf{h} \neq \mathbf{0}$ apart is 0. This reduces the spectral density $g(\boldsymbol{\omega})$ to

$$g(\boldsymbol{\omega}) = \frac{1}{(2\pi)^2} \left[\int_{-\infty}^{\infty} \underbrace{[\lambda_2(\mathbf{h}) - \lambda^2] + \lambda\delta(\mathbf{h})}_{=0} e^{-i\boldsymbol{\omega}'\mathbf{h}} d\mathbf{h} \right] \equiv \frac{\lambda}{(2\pi)^2}.$$

Therefore from Theorem 2.1, for $\boldsymbol{\omega}_{pq} \neq \mathbf{0}$, we have

$$E[I(\boldsymbol{\omega}_{pq})] \stackrel{A}{=} \frac{1}{2}g(\boldsymbol{\omega}) \cdot E[\chi_2^2] = \frac{1}{2} \frac{\lambda}{(2\pi)^2} \cdot 2 = \frac{1}{4\pi^2}\lambda$$

and

$$\text{var}[I(\boldsymbol{\omega}_{pq})] \stackrel{A}{=} \frac{1}{4}g^2(\boldsymbol{\omega}) \cdot \text{var}[\chi_2^2] = \frac{1}{4} \left[\frac{\lambda}{(2\pi)^2} \right]^2 \cdot 4 = \frac{1}{16\pi^4}\lambda^2.$$

For $\boldsymbol{\omega}_{pq} = \mathbf{0}$, we have

$$E[I(\boldsymbol{\omega}_{00})] \stackrel{A}{=} \frac{1}{2}g(\mathbf{0}) \cdot E[\chi_1^2] + \frac{\lambda}{(2\pi)^2} = \frac{1}{2} \frac{\lambda}{(2\pi)^2} \cdot 1 + \frac{\lambda}{(2\pi)^2} = \frac{3}{8\pi^2}\lambda$$

and

$$\text{var}[I(\boldsymbol{\omega}_{00})] \stackrel{A}{=} \frac{1}{4}g^2(\mathbf{0}) \cdot \text{var}[\chi_1^2] = \frac{1}{4} \left[\frac{\lambda}{(2\pi)^2} \right]^2 \cdot 2 = \frac{1}{32\pi^4}\lambda^2.$$

Q.E.D.

From Corollary 2.1 we can construct a hypothesis test for CSR using the spatial periodogram. Specifically, for an α -level test we would reject the hypothesis that a point pattern is CSR if

$$2 \frac{I(\boldsymbol{\omega}_{pq})}{\widehat{\lambda}/(2\pi)^2} \notin (\chi_{2,\alpha/2}^2, \chi_{2,1-\alpha/2}^2) \quad \text{for } (pq) \neq \mathbf{0},$$

where $\widehat{\lambda} = n$ is the basic estimator of intensity given by (2.1.11) for analysis on the unit square. Bartlett (1978) used the asymptotic independence and distribution of the periodogram ordinates to construct a goodness-of-fit test. Namely, under CSR,

$$\frac{2}{\widehat{\lambda}/(2\pi)^2} \sum_{(p,q) \neq (0,0)} I(\boldsymbol{\omega}_{pq}) \stackrel{CSR}{\sim} \chi_{2\nu}^2, \quad (2.2.9)$$

where ν is the number of ordinates included in the sum.

In the case of an isotropic spatial point process, the covariance density in (2.1.16) is a function of the Euclidean distance h between two events. Specifically, if $\mathbf{h}' = [h_x \ h_y]$, then the spectral density in (2.2.3) can be converted to polar coordinates by setting $\mathbf{h}' =$

$[r \cos \theta \quad r \sin \theta]$. From this we obtain

$$\begin{aligned}
 g(\boldsymbol{\omega}) &= \frac{1}{(2\pi)^2} \left\{ \int_{-\infty}^{\infty} \int_{-\infty}^{\infty} e^{-i(\omega_x h_x + \omega_y h_y)} v(\|\mathbf{h}\|) dh_x dh_y + \lambda \right\} \\
 &= \frac{1}{(2\pi)^2} \left\{ \int_0^{2\pi} \int_0^{\infty} e^{-ih(\omega_x \cos \theta + \omega_y \sin \theta)} v(h) h dh d\theta + \lambda \right\} \\
 &= \frac{1}{2\pi} \left\{ \int_0^{\infty} J_0(\omega h) v(h) h dh + \lambda \right\}, \tag{2.2.10}
 \end{aligned}$$

where $J_0(x)$ is the (unmodified) Bessel function of the first kind of order zero and $\omega = \|\boldsymbol{\omega}\|$ [Bartlett, 1978].

If isotropy exists then the periodogram is obtained by averaging over (random) angles θ for frequency ω and distance h . An estimate of the spectral density under these conditions is given by

$$I(\omega_p) = \frac{n}{2\pi} + \frac{1}{2\pi} \sum_{j=1}^n \sum_{\substack{k=1 \\ k \neq j}}^n J_0(\omega_p \|\mathbf{s}_j - \mathbf{s}_k\|). \tag{2.2.11}$$

Renshaw and Ford (1983) note that computation of (2.2.11) is no simpler than that of (2.2.4) and that it is a biased estimator of $g(\omega)$.

Because the fast Fourier transform cannot be employed for obtaining exact values of (2.2.4), Renshaw and Ford (1983) and Rigas (1991) suggest an approximation to improve computing time. Their approach places a fine regular grid on the study area. The transform is then calculated on the number of events found in each cell of the lattice.

From Theorem 2.1, we see that the spatial periodogram is an unbiased estimate for $g(\boldsymbol{\omega})$. However, as with the temporal periodogram, the variance of the spatial periodogram does not depend on n and therefore it is not consistent. The problem of consistency is reduced by smoothing $I(\boldsymbol{\omega}_{pq})$. The estimate of the spectral density is obtained by smoothing the periodogram using weights $W(\cdot)$:

$$\hat{g}(\boldsymbol{\omega}) = \sum_p \sum_q W(\boldsymbol{\omega} - \boldsymbol{\omega}_{pq}) I(\boldsymbol{\omega}_{pq}), \tag{2.2.12}$$

where $\boldsymbol{\omega} = [\omega_x \ \omega_y]'$ and $\boldsymbol{\omega}_{pq} = [\omega_p \ \omega_q]'$. Alternatively, one can simply average periodogram ordinates corresponding to ranges of p, q (or ρ, θ), which is the approach suggested below.

2.2.2 Polar Representation of the Spatial Periodogram

The three-dimensional periodogram described above is difficult to interpret graphically. Renshaw and Ford(1983) give a polar representation of the periodogram using

$$I(\boldsymbol{\omega}_{pq}) \equiv P(\boldsymbol{\omega}_{\rho\theta}),$$

where $\rho = \sqrt{p^2 + q^2}$ and $\theta = \tan^{-1}(q/p)$. The R -spectrum plot is constructed by averaging over periodogram ordinates with similar values of ρ :

$$f_R(\rho) = \frac{1}{n_\rho} \sum_{\rho'} \sum_{\theta} P(\omega_{\rho'}, \omega_\theta) \quad \rho = 1, 2, \dots, \quad (2.2.13)$$

where n_ρ are the number of ordinates for which $\rho - 1 < \rho' \leq \rho$.

The Θ -spectrum plot is constructed by averaging over periodogram ordinates with similar values of θ :

$$f_\Theta(\theta) = \frac{1}{n_\theta} \sum_{\rho} \sum_{\theta'} P(\omega_\rho, \omega_{\theta'}) \quad \theta = -85^\circ, -75^\circ, \dots, 85^\circ, \quad (2.2.14)$$

where n_θ are the number of ordinates for which $\theta - 5^\circ < \theta' \leq \theta + 5^\circ$. The ordinate for the (0,0) frequency is not included in either spectrum estimate. Figure 2.2.2 is a graphical representation of how the polar periodograms are obtained.

Under CSR the R - and Θ -spectra have asymptotic distributions

$$\frac{f_R(\rho)}{\lambda/(2\pi)^2} \xrightarrow{d} (2n_\rho)^{-1} \chi_{2n_\rho}^2, \quad \rho = 1, 2, \dots \quad (2.2.15)$$

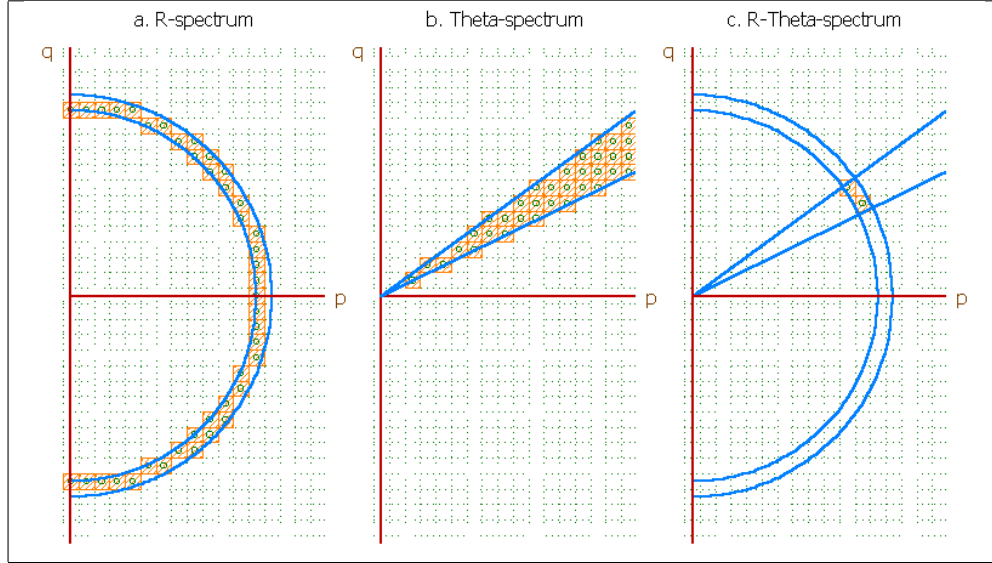


Figure 2.2: Construction of the Polar Spectra from the Spatial Periodogram.

and

$$\frac{f_{\Theta}(\theta)}{\lambda/(2\pi)^2} \xrightarrow{d} (2n_{\theta})^{-1} \chi_{2n_{\theta}}^2, \quad \theta = -85^{\circ}, -75^{\circ}, \dots, 85^{\circ}, \quad (2.2.16)$$

where n_{ρ} and n_{θ} are defined above [Mugglestone and Renshaw, 1996b]. Thus, values of $\frac{f_R(\rho)}{\lambda/(2\pi)^2}$ outside the $(1 - \alpha) \times 100\%$ confidence bounds given by $(2n_{\rho})^{-1} \left(\chi_{2n_{\rho}, \alpha/2}^2, \chi_{2n_{\rho}, 1-\alpha/2}^2 \right)$ suggest nonuniformity or stochastic dependence among events (e.g. clustering or regularity). In addition, values of $\frac{f_{\Theta}(\theta)}{\lambda/(2\pi)^2}$ outside the $(1 - \alpha) \times 100\%$ confidence bounds given by $(2n_{\theta})^{-1} \left(\chi_{2n_{\theta}, \alpha/2}^2, \chi_{2n_{\theta}, 1-\alpha/2}^2 \right)$ suggest a possible anisotropy of the auto-covariance function. The estimate of λ is given by (2.1.11) if second-order stationarity is assumed. Moreover, since periodogram analysis scales the data to the unit square, then $\hat{\lambda} = n$ for $|A| = 1$.

2.2.3 Inference based on the R - and Θ -Spectrum

The polar spectra offer additional inference options not available by direct inspection of the spatial periodogram. As mentioned in the previous section, the R -spectrum reveals the uniformity of events in the spatial point process, while the Θ -spectrum gives insight into the isotropy of the covariance. One can also combine the R - and Θ -spectra to obtain

a complete polar periodogram which may indicate clustering or regularity in a particular direction. The R - Θ -spectrum is calculated by averaging the spatial periodogram ordinates in the intersection of an arc of radius ρ and a ray of angle θ . The R - Θ -spectrum offers finer detail of the second-order properties of the spatial process. See Figure 2.2.2 for construction of the R -spectrum, Θ -spectrum, and R - Θ -spectrum.

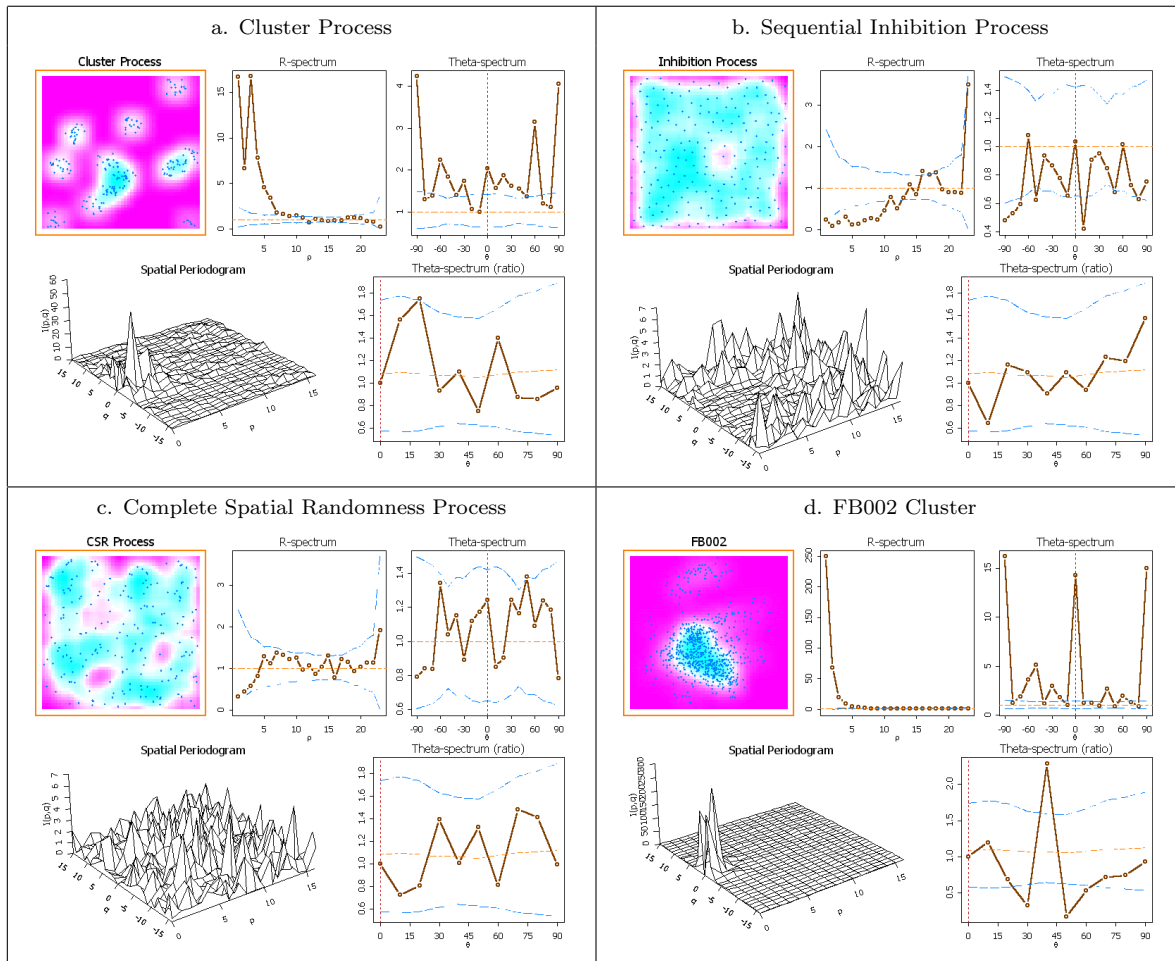


Figure 2.3: Spectral analysis of spatial point patterns for three different processes (a-c) and cluster FB002 from the woodpecker data (d). The intensity estimates are the same as those in Figure 2.1.3. See page 41 for definition of Θ -spectrum ratios.

Hypothesis Tests for Spatial Uniformity and/or Independence

The R -spectrum serves as the frequency domain analog to the K -function described in Section 2.1.3. As with the K -function analysis, use of the R -spectrum does not allow distinguishing between spatial nonuniformity and dependence of events, unless the process is second-order stationary in which case $\lambda(\mathbf{s}) = \lambda$ and derivations for CSR pattern indicate interaction (dependence) of events.

Interpretation of the R -spectrum is identical to that of the K -function: large values of $f_R(\rho)$ for small ρ imply clustering of events while small values of $f_R(\rho)$ for small ρ imply regularity of events. However, the advantage of using the R -spectrum is that simulated inference is not required. Because of the asymptotic distribution of the periodogram ordinates conclusions with respect to the R -spectrum (as well as the Θ -spectrum discussed below) can be based on $(1 - \alpha) \times 100\%$ confidence bands from a scaled χ^2 distribution.

Figure 2.2.3 shows the spectral analysis of the three simulated point patterns introduced in Chapter 1 (Figure 1.3.2) as well as the FB002 cluster from the woodpecker data (Figure 1.5). The R -spectrum for the clustered pattern (Figure 2.2.3a) shows a higher than expected frequency of events under the null hypothesis of CSR for small ρ . Specifically, the large value of $f_R(1)$ captures the clustering radius of each parent cluster. For $\rho = 2$ the spectrum takes a dip before rising again for $\rho = 3$. This phenomenon can be explained by the space between the parent events. Since the data were generated on the unit square, the clustering radius can be easily converted to a distance h in the original units by letting $h = \rho/16$. This assumes we are using $p = 0, 1, \dots, 16$ and $q = -15, \dots, 16$ as suggested in Section 2.2. Comparisons of the analyses of the data in Figures 2.2.3 and 2.1.3 can be found in Chapter 4.

Hypothesis Tests for Anisotropy

A key advantage of analyzing spatial point patterns in the frequency domain is that the assumption of isotropy is not required. The Θ -spectrum indeed allows for investigation

of anisotropy in the spatial point pattern by searching the spatial periodogram for large ordinates in a particular direction θ . While the R -spectrum serves as the frequency domain version of the K -function, there is no analog to the Θ -spectrum in the spatial domain. However, the Θ -spectrum can be difficult to interpret if either clustering or regularity exist. In Figure 2.2.3, the Θ -spectrum is constructed for the spatial point patterns in Figure 1.3.2. For the cluster process, the Θ -spectrum has ordinates that exceed the 95% confidence bounds for $\theta = -90^\circ, -60^\circ, -50^\circ, -40^\circ, -30^\circ, 0^\circ, 10^\circ, 20^\circ, 30^\circ, 40^\circ, 60^\circ, 90^\circ$. But this does not imply that the process is anisotropic in all those directions. The large ordinates in the Θ -spectrum are an artifact of the construction of the spectrum and are present due to the high clustering. Specifically, in a clustered process large ordinates appear for small frequencies, which in turn get averaged over different values of θ in the Θ -spectrum. Thus, the effect of the clustering is clouding any possible anisotropy in the process. A similar phenomenon can be observed in regular spatial processes and possibly even CSR processes (Figure 2.2.3).

For this reason, a ratio of the Θ -spectrum ordinates is used. If a spatial point pattern is isotropic then we would expect

$$f_{\Theta}(\theta) = f_{\Theta}(-\theta), \quad (2.2.17)$$

which implies that the process is invariant under rotation. Because $f_{\Theta}(\theta)$ and $f_{\Theta}(-\theta)$ are asymptotically independent scaled χ^2 distributions, the ratio of the ordinates in (2.2.17) is an F distribution given by

$$\frac{f_{\Theta}(\theta)}{f_{\Theta}(-\theta)} \xrightarrow{d} \frac{(2n_{\theta})^{-1}\chi_{2n_{\theta}}^2}{(2n_{-\theta})^{-1}\chi_{2n_{-\theta}}^2} = F_{2n_{\theta}, 2n_{-\theta}} \quad (2.2.18)$$

whose expected value under the assumption of (2.2.17) is

$$E \left[\frac{f_{\Theta}(\theta)}{f_{\Theta}(-\theta)} \right] \stackrel{A}{=} E [F_{2n_{\theta}, 2n_{-\theta}}] = \frac{2n_{-\theta}}{2n_{-\theta} - 2}. \quad (2.2.19)$$

From (2.2.18) we can construct $(1-\alpha) \times 100\%$ confidence bounds based on the F -distribution.

Specifically, if no anisotropy exists then

$$\frac{f_{\Theta}(\theta)}{f_{\Theta}(-\theta)} \in (F_{2n_{\theta}, 2n_{-\theta}, \alpha/2}, F_{2n_{\theta}, 2n_{-\theta}, 1-\alpha/2}).$$

However, if anisotropy exists in direction θ , then we should see

$$\frac{f_{\Theta}(\theta)}{f_{\Theta}(-\theta)} > F_{2n_{\theta}, 2n_{-\theta}, 1-\alpha/2}.$$

Conversely, if anisotropy exists in direction $-\theta$, then we should see

$$\frac{f_{\Theta}(\theta)}{f_{\Theta}(-\theta)} < F_{2n_{\theta}, 2n_{-\theta}, \alpha/2}.$$

The ratio plots of the Θ -spectrum along with 95% confidence bounds and the value of (2.2.19) for each simulated process in Figure 1.3.2 and the FB002 cluster in Figure 1.5 are shown in Figure 2.2.3. As expected, examination of the Θ -spectrum ratio plots for each of the simulated processes reveal no apparent anisotropy. However, the FB002 cluster appears to be oriented along the -60° angle.

2.3 Geometric Anisotropy for Spatial Point Patterns

From the previous section we saw that the Θ -spectrum can be used to diagnose anisotropy in a spatial point pattern. In this section we explore the properties of the periodogram if the covariance function displays a geometric anisotropy.

Let $Z(\mathbf{s})$ be a stationary, geometrically anisotropic point pattern in \mathfrak{R}^2 with second-order intensity $\lambda_2(\mathbf{h})$. Then we can impose a rotation (by ϕ) and scaling (by σ) of the data to

remove the effect of anisotropy by the following nonlinear transformation:

$$\mathbf{s}^0 = \underbrace{\begin{bmatrix} \cos \phi & -\sin \phi \\ \sin \phi & \cos \phi \end{bmatrix}}_{=\mathbf{Q}} \begin{bmatrix} 1 & 0 \\ 0 & \sigma^{-1} \end{bmatrix} \mathbf{s}, \quad (2.3.1)$$

or

$$\begin{bmatrix} 1 & 0 \\ 0 & \sigma \end{bmatrix} \underbrace{\begin{bmatrix} \cos \phi & \sin \phi \\ -\sin \phi & \cos \phi \end{bmatrix}}_{=\mathbf{Q}^{-1}} \mathbf{s}^0 = \mathbf{s}, \quad (2.3.2)$$

where \mathbf{s}^0 is an event in the isotropic space, \mathbf{s} is an event in the anisotropic space, σ is a scale factor in $(0, 1]$, and ϕ is the direction of anisotropy. Scale factors larger than one can be mapped to the $(0, 1]$ interval by choosing an appropriate value of ϕ . From (2.3.1), we see that distance between two arbitrary events \mathbf{s}_i^0 and \mathbf{s}_j^0 in the isotropic space becomes

$$\mathbf{s}_i^0 - \mathbf{s}_j^0 = \begin{bmatrix} \cos \phi & -\sin \phi \\ \sin \phi & \cos \phi \end{bmatrix} \begin{bmatrix} 1 & 0 \\ 0 & \sigma^{-1} \end{bmatrix} \underbrace{[\mathbf{s}_i - \mathbf{s}_j]}_{=\mathbf{h}} = \mathbf{Q}\mathbf{h}_{ij}. \quad (2.3.3)$$

It follows then that the second-order intensity between events \mathbf{s}_i^0 and \mathbf{s}_j^0 is given by

$$\lambda_2^0(h) = \lambda_2^0(\|\mathbf{Q}\mathbf{h}\|), \quad (2.3.4)$$

where λ_2^0 is an isotropic second-order intensity function determined only by the Euclidean distance h between events \mathbf{s}_i^0 and \mathbf{s}_j^0 in the isotropic space. In terms of the anisotropic events, in which the second-order intensity is a function of \mathbf{h} but is not rotation-invariant, (2.3.4) can be written as

$$\lambda_2(\mathbf{h}) = \lambda_2^0(\|\mathbf{Q}\mathbf{h}\|), \quad (2.3.5)$$

where λ_2 is an anisotropic second-order intensity (Figure 2.3).

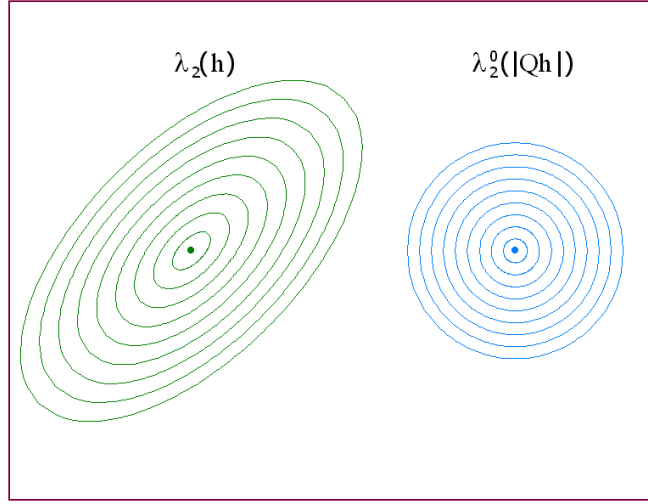


Figure 2.4: Transformation of a geometrically anisotropic second-order intensity function to an isotropic second-order intensity function.

2.3.1 Properties of the Spatial Periodogram Under Geometric Anisotropy

If geometric anisotropy is ignored, this is equivalent to analyzing the transformed events $\mathbf{Q}^{-1}\mathbf{s}_j^0$ on the incorrect bounding box \mathbf{A}^0 rather than a scaled and rotated bounding box $\mathbf{Q}^{-1}\mathbf{A}^0$. The periodogram of the transformed events would be constructed in the same manner as (2.2.6) except for the incorrect scaling matrix \mathbf{L}^0 . Thus, the periodogram is given by

$$\begin{aligned}
 I(\omega_{pq}) &= \frac{1}{(2\pi)^2} \sum_{j=1}^n \sum_{k=1}^n \exp \{ -i\omega'_{pq} (\mathbf{L}^0)^{-1} \mathbf{h}_{jk} \} \\
 &= \frac{1}{(2\pi)^2} \sum_{j=1}^n \sum_{k=1}^n \exp \{ -i\omega'_{pq} (\mathbf{L}^0)^{-1} \mathbf{Q}^{-1} \mathbf{h}_{jk}^0 \} \\
 &= \frac{1}{(2\pi)^2} \sum_{j=1}^n \sum_{k=1}^n \exp \{ -i\omega'_{pq} (\mathbf{Q}\mathbf{L}^0)^{-1} \mathbf{h}_{jk}^0 \}, \tag{2.3.6}
 \end{aligned}$$

where \mathbf{L}^0 is the bounding box of the anisotropic process.

Therefore, \mathbf{QL}^0 becomes the new scaling matrix which has an inverse given by

$$\begin{aligned} (\mathbf{QL}^0)^{-1} &= \left(\begin{bmatrix} \cos \phi & -\sin \phi \\ \sin \phi & \cos \phi \end{bmatrix} \begin{bmatrix} 1 & 0 \\ 0 & \sigma^{-1} \end{bmatrix} \begin{bmatrix} L_x^0 & 0 \\ 0 & L_y^0 \end{bmatrix} \right)^{-1} \\ &= \begin{bmatrix} \cos \phi / L_x^0 & \sin \phi / L_x^0 \\ -\sigma \sin \phi / L_y^0 & \sigma \cos \phi / L_y^0 \end{bmatrix}. \end{aligned} \quad (2.3.7)$$

Expanding the matrices in (2.3.6) we obtain

$$\begin{aligned} I(\omega_{pq}) &= \frac{1}{(2\pi)^2} \sum_{j=1}^n \sum_{k=1}^n \exp \left\{ -i[2\pi p \quad 2\pi q] \begin{bmatrix} \cos \phi / L_x^0 & \sin \phi / L_x^0 \\ -\sigma \sin \phi / L_y^0 & \sigma \cos \phi / L_y^0 \end{bmatrix} \begin{bmatrix} h_{jkx}^0 \\ h_{jky}^0 \end{bmatrix} \right\} \\ &= \frac{1}{(2\pi)^2} \sum_{j=1}^n \sum_{k=1}^n \exp \{ -i[\omega_p^* h_{jkx}^0 + \omega_q^* \sigma h_{jky}^0] \}, \end{aligned} \quad (2.3.8)$$

where

$$\omega_{pq}^* = \begin{bmatrix} \omega_p^* \\ \omega_q^* \end{bmatrix} = \begin{bmatrix} 2\pi p^* \\ 2\pi q^* \end{bmatrix} = \begin{bmatrix} 2\pi(pL_x^{-1} \cos \phi - qL_y^{-1} \sin \phi) \\ 2\pi(pL_x^{-1} \sin \phi + qL_y^{-1} \cos \phi) \end{bmatrix}. \quad (2.3.9)$$

From (2.3.8) we see that the scale factor σ shows up in the rotated, longitudinal frequencies ω_q .

If the analysis of the point pattern is done on the correct bounding box \mathbf{QA} , the periodogram of the transformed events would have the following representation:

$$\begin{aligned} I(\omega_{pq}) &= \frac{1}{(2\pi)^2} \sum_{j=1}^n \sum_{k=1}^n \exp \{ -i\mathbf{L}^{-1} \mathbf{h}_{jk} \} \\ &= \frac{1}{(2\pi)^2} \sum_{j=1}^n \sum_{k=1}^n \exp \{ -i\mathbf{L}^{-1} \mathbf{Q}^{-1} \mathbf{h}_{jk}^0 \} \\ &= \frac{1}{(2\pi)^2} \sum_{j=1}^n \sum_{k=1}^n \exp \{ -i(\mathbf{QL})^{-1} \mathbf{h}_{jk}^0 \} \end{aligned} \quad (2.3.10)$$

where \mathbf{L} is a scaling matrix defined on the anisotropic transformation and is given by

$$\mathbf{L} = \begin{bmatrix} L_x & 0 \\ 0 & L_y \end{bmatrix} = \begin{bmatrix} L_x^0 \cos \phi + \sigma L_y^0 \sin \phi & 0 \\ 0 & -L_x^0 \sin \phi + \sigma L_y^0 \cos \phi \end{bmatrix}. \quad (2.3.11)$$

The lengths (L_x, L_y) and (L_x^0, L_y^0) in (2.3.11) are the lengths of the bounding box in the transformed and naïve spaces, respectively (Figure 2.3.2).

In the case of an isotropic spatial point process, the covariance density is a function of the Euclidean distance h between two events. Specifically, if $\mathbf{h}' = [h_x \ h_y]$, then the spectral density in (2.2.3) can be converted to polar coordinates by setting

$$\mathbf{h}' = [h \cos \phi \ h \sin \phi], \quad (2.3.12)$$

where $h = |\mathbf{h}|$. Combining (2.2.3) and (2.3.12) we obtain (2.2.10) [Bartlett, 1978].

Combining the transformation given by (2.3.1) with the isotropic spectral density in (2.2.10) we see that the spectral density of a geometrically anisotropic process is given by

$$g(\omega) = \frac{1}{2\pi} \left\{ \int_0^\infty J_0(\omega \cdot \|\mathbf{Qh}\|) [\lambda_2^0(\|\mathbf{Qh}\|) - \lambda^2] d\|\mathbf{Qh}\| + \lambda \right\}. \quad (2.3.13)$$

Thus the periodogram is given by

$$I(\omega_p) = \frac{1}{2\pi} \sum_{j=1}^n \sum_{k=1}^n \exp\{-i\omega_p |\mathbf{L}^{-1} \mathbf{Qh}_{jk}| \} \quad p = 0, \pm 1, \pm 2, \dots, \quad (2.3.14)$$

where ω_p is now a single frequency. Therefore, from (2.3.14), we see that if σ and ϕ are known, then we can undo the transformation in (2.3.1) and obtain a one-dimensional periodogram.

2.3.2 Spectral Analysis under Geometric Anisotropy

From the previous section, one major question remains: Can we use the Θ -spectrum to detect ϕ and σ ? One of the main benefits of spectral analysis of spatial point patterns is the assumption of stationarity without requiring isotropy. Therefore, the periodogram analysis can be used to diagnose and possibly remove anisotropy from the process. Specifically, the Θ -spectrum allows us to choose the major and minor axes of alignment for a geometrically anisotropic point pattern.

If geometric anisotropy is present there is one angle to diagnose from the Θ -spectrum: the rotation ϕ of the major axis. However, for larger values of σ the angle ϕ' of the minor axis, which is perpendicular to the major axis, may also be significant. Figure 2.3.2 shows results from two simulation studies. Two hundred Poisson (CSR) processes were generated on a unit square centered at $(0, 0)$. The point patterns were then rotated through the center by angles $\phi = -\pi/10(\pi/5)$ and scaled by $\sigma = 0.2(0.5)$. Thus, geometric anisotropy of covariance density was obtained using the transformation in (2.3.3). Section 2.3.3 has simulations for identical rotations and scalings for cluster and sequential inhibition processes.

For each point pattern in the simulation, the R - and Θ -spectra are computed on the untransformed bounding box A^0 . This is equivalent to a naïve analysis of the point pattern that ignores the rotation and scaling. The polar spectra ordinates were then averaged over all 200 simulations to construct the plots in Figure 2.3.2.

Examination of the Θ -spectrum on the incorrect bounding box (L_x^0, L_y^0) in Figure 2.3.2 reveals the presence of geometric anisotropy, though not where one would expect. Specifically, the ordinates at $\theta = -\pi/4$ for simulation 1 and at $\theta = \pi/4$ for simulation 2 are significant according to the rejection region defined in Section 2.2.2. If we are to use the Θ -spectrum to diagnose a rotation we would expect the ordinates closest to $-\pi/10$ and $\pi/5$ to be significant. However, from Figure 2.3.2 we see that the ratio of the Θ -spectrum ordinates at $\pi/4$ and $-\pi/4$ appears to be a function of σ . Since the appearance of large ordinates at $\pm\pi/4$ rather than at ϕ is puzzling, the functional form relating the Θ -spectrum ordinates to ϕ and σ

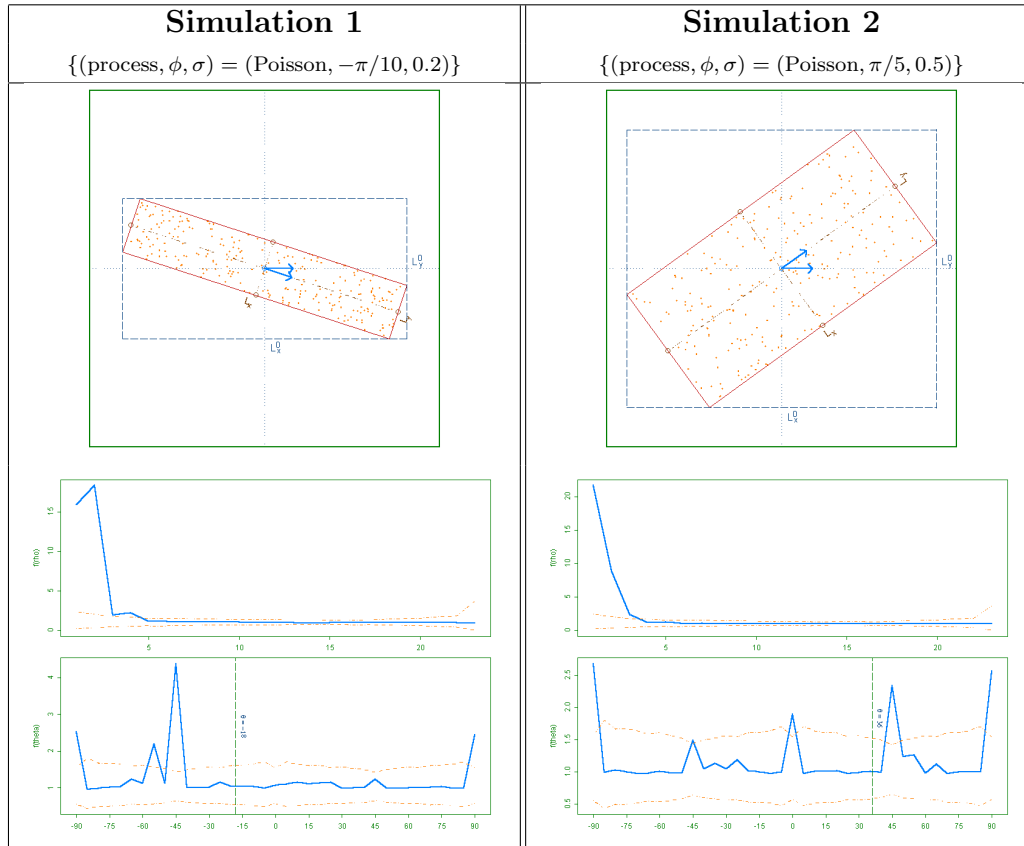
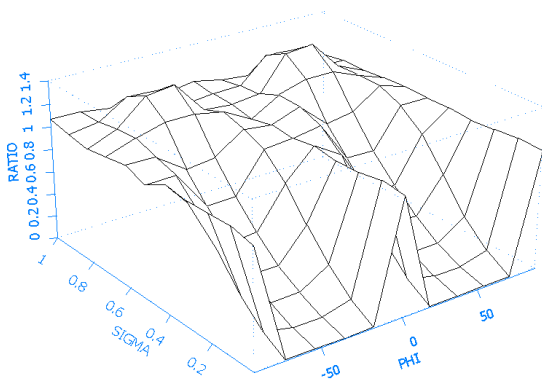


Figure 2.5: Results from two simulations of a rotated Poisson Process. Top figures show rotation and scaling of the bounding box for a Poisson process on the unit square. (L_x, L_y) and (L_x^0, L_y^0) denote the lengths of the sides of the bounding box for the transformed point pattern and a naïve analysis, respectively. Bottom four plots are the R - (second row) and Θ -spectra (third row) for the transformed point patterns, averaged over the 200 simulated point patterns.

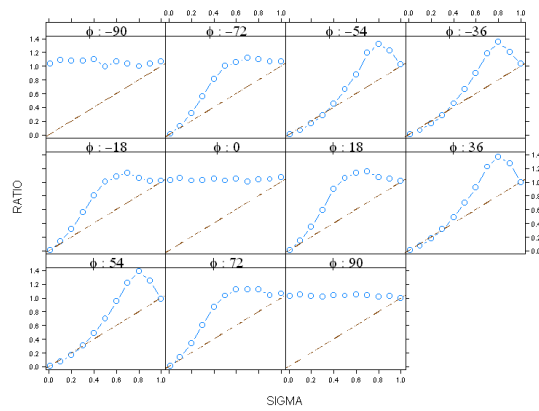
remains unknown at this time. However, one speculation is that the Θ -spectrum is most stable at $\pm\pi/4$ because the most ordinates are being averaged at this angle. At $\pm\phi$, fewer ordinates are being averaged and the Θ -spectrum ordinates may be too erratic to stabilize $f_{\Theta}(\phi)/f_{\Theta}(-\phi)$.

To see the relationship between the Θ -spectrum ordinates and the value of σ another simulation was performed for $\sigma \in (0.01, 0.1, 0.2, \dots, 1.0)$. As before, for each simulation, 200 anisotropic point patterns were obtained for $\phi = -\pi/2 + k\pi/10$ for $k = 0, \dots, 10$. Once the Θ -spectrum was constructed from the 200 simulations, the ratio of the Θ -spectrum ordinate

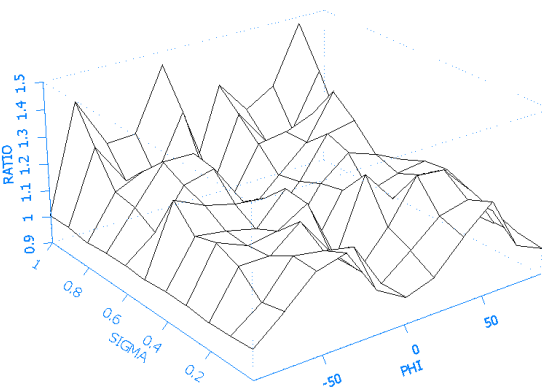
at angle θ to the ratio of the Θ -spectra ordinate at θ' was computed. Figure 2.3.2a is a 3-d plot of the latter ratio for each value of σ and ϕ . Figure 2.3.2c is a profile plot of the ratio versus σ for each value of ϕ and Figure 2.3.2d is profile plot of the ratio versus ϕ for each value of σ . The diagonal line in Figure 2.3.2c is the line $y = x$ and is used only as a reference. Figure 2.3.2b shows the results of using the ratio of the periodogram ordinates from ϕ and $-\phi$. No apparent structure is seen in this plot.



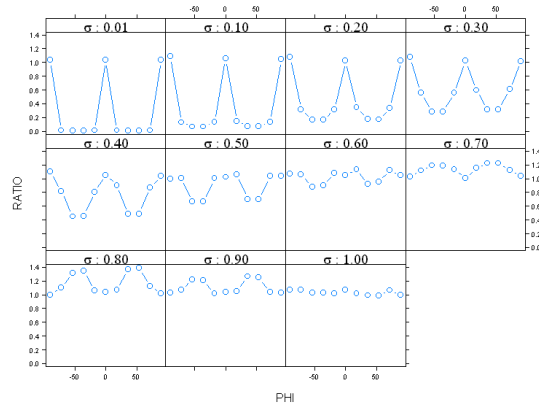
a. 3-d plot of $f_{\Theta}(\pi/4)/f_{\Theta}(-\pi/4)$ vs. ϕ and σ



c. Cross-sections of ratio vs. σ for different values of ϕ .



b. 3-d plot of $f_{\Theta}(\phi)/f_{\Theta}(-\phi)$ vs. ϕ and σ



d. Cross-sections of ratio vs. ϕ for different values of σ .

Figure 2.6: (a,c,d). Ratio of the Θ -spectrum ordinates for $\theta' = -\pi/4$ and $\theta = \pi/4$, versus the true values of ϕ and σ . The angles of rotation are $\phi = -\pi/2, -3\pi/8, \dots, \pi/2$ and the scales are $\sigma = 0.1, 0.2, \dots, 1.0$. The diagonal is the line $y = x$ which is used as a reference. (b). Ratio of the Θ -spectrum ordinates for ϕ and $-\phi$, versus the true values of ϕ and σ .

2.3.3 Simulations for Clustered and Regular Processes

Two more simulations were completed to study the effects of geometric anisotropy for different spatial processes. The Poisson process was studied in Figure 2.3.2 for 200 Monte Carlo point patterns with $\phi = -\pi/10(\pi/5)$ and $\sigma = 0.2(0.5)$. Without changing the values of ϕ and σ a Poisson Cluster process (defined in Section 1.3.2) was generated for 200 point patterns with $\mu_p = 10$ and a dispersion radius of 0.07. Figure 2.3.3 shows the results for $(\phi, \sigma) = (-\pi/10, 0.2)$ and $(\phi, \sigma) = (\pi/5, 0.5)$. Similarly, a simulation was run for a sequential spatial inhibition process (defined in Section 1.3.2) for identical values of ϕ and σ . The results of the simulation can be viewed in Figure 2.3.3.

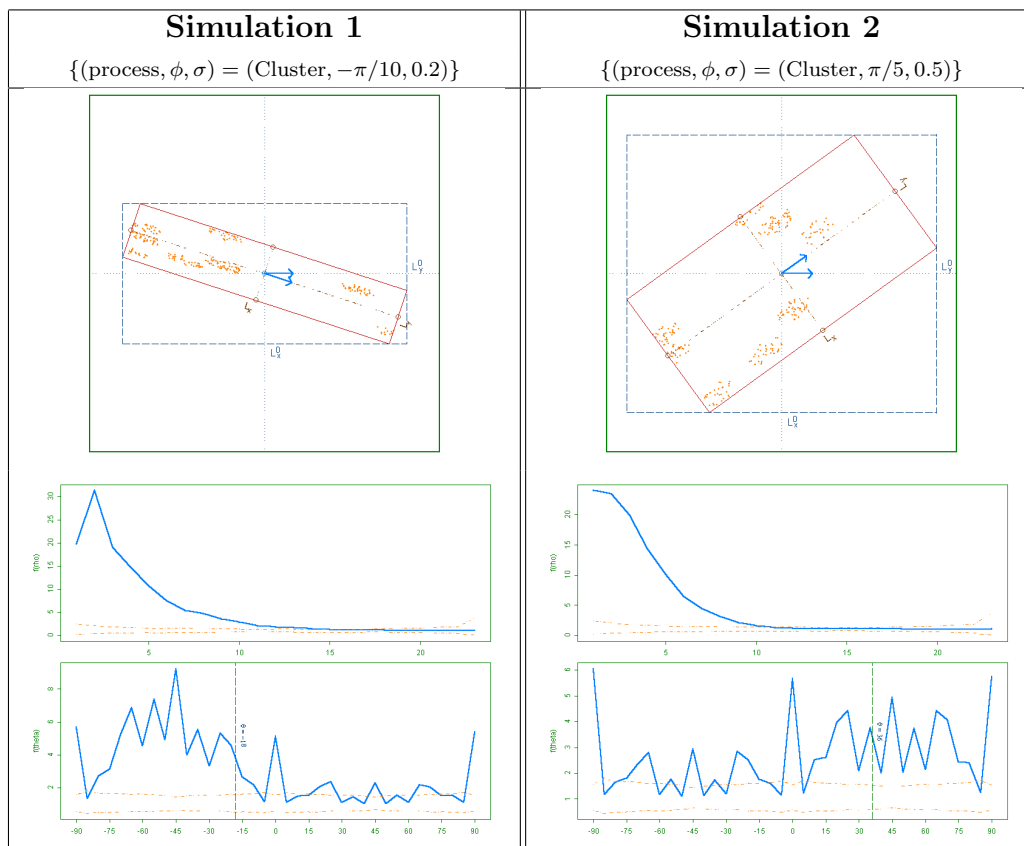


Figure 2.7: Results from two simulations of a rotated Clustered Process where the number of parents are Poisson(10) and the radius of dispersion is 0.07. Top figures show rotation and scaling of the bounding box for a Cluster process on the unit square. Bottom figures are the R - (second row) and Θ -spectra (third row) averaged over the 200 simulated point patterns.

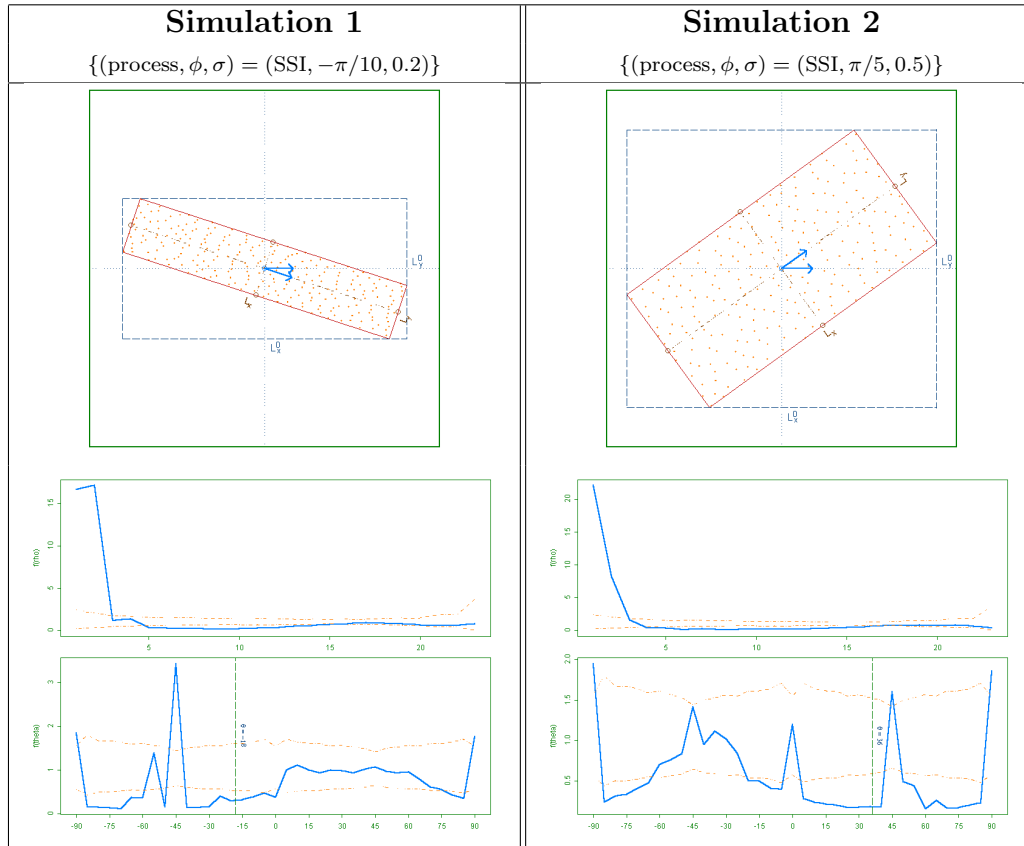


Figure 2.8: Results from two simulations of a rotated Sequential Spatial Inhibition Process where the radius of inhibition is 0.05. Top figures show rotation and scaling of the bounding box for a SSI process on the unit square. Bottom figures are the R - (second row) and Θ -spectra (third row) averaged over the 200 simulated point patterns.

For the Θ -spectrum of the clustered process, the scale parameter seems more apparent. Specifically, the Θ -spectrum reveals some type of scaled symmetry of the ordinates about $\theta = 0$. Moreover, ordinates for $\theta < 0$ appear to be symmetric about $-\pi/4$ and ordinates for $\theta > 0$ appear to be symmetric about $\pi/4$. As with the previous analysis of the CSR processes in the previous section, the angle $\pm\pi/4$ appears to be playing a large but unknown role in the Θ -spectrum if geometric anisotropy is present. The Θ -spectrum for the SSI process has less apparent structure. However, the prominence of the ordinates at $\theta = \pm\pi/4$ is still present.

Chapter 3

Spatiotemporal Point Patterns

Stochastic processes with spatial and temporal components should not be considered as processes in \mathfrak{R}^3 by simply adding a further dimension to a spatial process in \mathfrak{R}^2 . Instead, we define a spatiotemporal point process as

$$\{Z(\mathbf{s}, t) : \mathbf{s} \in D(t) \subset \mathfrak{R}^2, t \in T\}. \quad (3.0.1)$$

As with spatial point patterns the spatial index set $D(t)$ is random but the temporal index set T may or may not be deterministic. We will consider the process in (3.0.1) as a hybrid of the spatial point process and the time series, possibly governed by dependent probability measures.

3.1 Intensity Measures of Spatiotemporal Point Processes

The goal is to express the relationship of points not only by distance but by time lag. Our initial concern is to modify the first- and second-order intensity functions to incorporate temporal and spatial dimensions.

3.1.1 First-Order Intensities

The intensity function $\lambda(\cdot)$ can be modified to include a time component as

$$\lambda(\mathbf{s}, t) = \lim_{|d\mathbf{s}|, |dt| \rightarrow 0} \frac{E[N(d\mathbf{s}, dt)]}{|d\mathbf{s}||dt|}, \quad (3.1.1)$$

where $N(A)$ represents the number of events in volume A , $d\mathbf{s}$ is an infinitesimal disc containing the location \mathbf{s} , and dt is an infinitesimal interval containing time t . Following Haas (1995) we consider A as a cylinder with face $d\mathbf{s}$ and height dt . Note that this is an obvious extension of the first-order intensity in a spatial point process which considers the expected number of points in a disc $d\mathbf{s}$. Thus, $N(d\mathbf{s}, dt)$ represents the number of points in the cylinder. The limit in (3.1.1) shrinks the cylinder around the point (\mathbf{s}, t) .

Define the *marginal spatial intensity* as

$$\lambda(\mathbf{s}, \cdot) = \int_T \lambda(\mathbf{s}, t) dt, \quad (3.1.2)$$

where \int_T represents integration over all time T . Similarly, the *marginal temporal intensity* is defined as

$$\lambda(\cdot, t) = \int_A \lambda(\mathbf{s}, t) d\mathbf{s}, \quad (3.1.3)$$

where \int_A represents integration over the region A . The marginal intensities allow us to view one component, either spatial or temporal, while ignoring the other component. Furthermore, as we will see in Section 3.1.3, if $\lambda(\mathbf{s}, t)$ is equal to either or both of the marginal intensities then the process is said to be first-order stationary in time, space, or both.

Conditioning on either location or time allows us to isolate either component in a spatiotemporal process. Conditioning on t reduces the spatiotemporal intensity defined in (3.1.1) to *conditional spatial intensity*

$$\lambda(\mathbf{s}|t = t^*) = \lim_{|d\mathbf{s}| \rightarrow 0} \frac{E[N(d\mathbf{s}, t^*)]}{|d\mathbf{s}|}. \quad (3.1.4)$$

Similarly, conditioning on \mathbf{s} leads to

$$\lambda(t|\mathbf{s} = \mathbf{s}^*) = \lim_{|dt| \rightarrow 0} \frac{E[N(\mathbf{s}^*, dt)]}{|dt|}, \quad (3.1.5)$$

the *conditional temporal intensity*.

We also define the *average spatial intensity*

$$\lambda(\mathbf{s}, dt) = \lim_{|ds| \rightarrow 0} \frac{E[N(ds, dt)]}{|ds||dt|} \quad (3.1.6)$$

and the *average temporal intensity*

$$\lambda(ds, t) = \lim_{|dt| \rightarrow 0} \frac{E[N(ds, dt)]}{|ds||dt|}. \quad (3.1.7)$$

(3.1.6) represents the average intensity over the interval dt at location \mathbf{s} and (3.1.7) represents the average intensity over the space $|ds|$ at time t . This notation will allow us to collapse (3.1.1) one component at a time: spatially or temporally. Also note that

$$\lambda(\mathbf{s}, t) = \lim_{|dt| \rightarrow 0} \lambda(\mathbf{s}, dt) = \lim_{|ds| \rightarrow 0} \lambda(ds, t).$$

Combining the notation of (3.1.4) and (3.1.5) with the notation of (3.1.6) and (3.1.7), similar expressions for the *average conditional spatial intensity*, $\lambda(ds|t)$, and the *average conditional temporal intensity*, $\lambda(dt|\mathbf{s})$, are obtained as

$$\lambda(ds|t = t^*) = \frac{E[N(ds, t^*)]}{|ds|} \quad (3.1.8)$$

and

$$\lambda(dt|\mathbf{s} = \mathbf{s}^*) = \frac{E[N(\mathbf{s}^*, dt)]}{|dt|}. \quad (3.1.9)$$

These definitions of the different first-order intensity functions are recalled in Table 3.1.

The first-order intensities defined in this section may not be appropriate for all spatiotemporal point patterns. For the earthquake process which is both orderly in space and time the concept of a conditional intensity at time t or location \mathbf{s} has no meaning. However, conditional intensities for earthquake processes can be constructed on intervals in time or regions in space [Rathbun, 1996]. The conditional intensities on intervals in space and/or

Table 3.1: First-Order Intensity Measures.

Notation	Description	Equation No.
$\lambda(\mathbf{s}, t)$	General spatiotemporal intensity	3.1.1
$\lambda(\mathbf{s}, \cdot)$	Marginal spatial intensity	3.1.2
$\lambda(\cdot, t)$	Marginal temporal intensity	3.1.3
$\lambda(\mathbf{s} t)$	Conditional spatial intensity	3.1.4
$\lambda(t \mathbf{s})$	Conditional temporal intensity	3.1.5
$\lambda(\mathbf{s}, dt)$	Average spatial intensity	3.1.6
$\lambda(d\mathbf{s}, t)$	Average temporal intensity	3.1.7
$\lambda(d\mathbf{s} t)$	Average conditional spatial intensity	3.1.8
$\lambda(dt \mathbf{s})$	Average conditional temporal intensity	3.1.9

time are denoted above by the average conditional intensities.

For the other spatiotemporal point processes shown in Figure 1.4.1, all the intensities given in this section can be explicitly defined and utilized in subsequent analyses. For the woodpecker data introduced in Chapter 1, we will exploit the marginal spatial intensity to conduct a strictly spatial analysis disregarding to the temporal component. As a comparison to what may be lost in the spatial analysis we will first incorporate the conditional spatial intensity which will give rise to the full spatiotemporal intensity. However, as we will see in Section 3.1.3, we will require first-order stationarity to make this comparison.

The average spatial and temporal intensities discussed in this section enable focusing on smaller details of a given process. If, for example, we do not have stationarity we can limit our analyses to smaller regions in time and/or space. This is done quite often in spatial and temporal analyses when the process of interest is globally nonstationary but locally stationary.

3.1.2 Second-Order Intensities

The extension of $\lambda(\cdot)$ to include a temporal component leads, by analogy, to the general definition of the second-order spatiotemporal intensity $\lambda_2(\cdot)$ as

$$\lambda_2(\mathbf{s}_{i1}, \mathbf{s}_{j2}, t_1, t_2) = \lim_{|A_{i1}|, |A_{j2}| \rightarrow 0} \frac{E[N(A_{i1})N(A_{j2})]}{|A_{i1}||A_{j2}|}, \quad (3.1.10)$$

where $A_{i1} = d\mathbf{s}_{i1} \times dt_1$ is an infinitesimal cylinder containing the point (\mathbf{s}_{i1}, t_1) and $A_{j2} = d\mathbf{s}_{j2} \times dt_2$ is an infinitesimal cylinder containing the point (\mathbf{s}_{j2}, t_2) . Second-order spatiotemporal intensities will be defined to correspond to the first-order intensities given in Table 3.1.

The *marginal second-order intensity* removes either the spatial or temporal component by integrating over the spatial or temporal space. The *marginal second-order spatial intensity* is defined by

$$\lambda_2(\mathbf{s}_{i*}, \mathbf{s}_{j*}, \cdot, \cdot) = \int_T \int_T \lambda_2(\mathbf{s}_{ik}, \mathbf{s}_{jl}, t_1, t_2) dt_1 dt_2, \quad (3.1.11)$$

where \int_T represents integration over all time. The *marginal second-order temporal intensity* is defined by

$$\lambda_2(\cdot, \cdot, t_1, t_2) = \int_{A_1} \int_{A_2} \lambda_2(\mathbf{s}_1, \mathbf{s}_2, t_1, t_2) d\mathbf{s}_1 d\mathbf{s}_2, \quad (3.1.12)$$

where \int_{A_t} represents integration over the region A at time t .

Conditioning on time in (3.1.10) gives us the *conditional second-order spatial intensity* defined by

$$\lambda_2(\mathbf{s}_{i*}, \mathbf{s}_{j*} | t = t^*) = \lim_{|d\mathbf{s}_{i*}|, |d\mathbf{s}_{j*}| \rightarrow 0} \frac{E[N(d\mathbf{s}_{i*}, t^*)N(d\mathbf{s}_{j*}, t^*)]}{|d\mathbf{s}_{i*}||d\mathbf{s}_{j*}|}. \quad (3.1.13)$$

Similarly, conditioning on location in (3.1.10) yields the *conditional second-order temporal intensity* defined by

$$\lambda_2(t_1, t_2 | \mathbf{s} = \mathbf{s}^*) = \lim_{|dt_1||dt_2| \rightarrow 0} \frac{E[N(\mathbf{s}^*, dt_1)N(\mathbf{s}^*, dt_2)]}{|dt_1||dt_2|}. \quad (3.1.14)$$

As with the first-order conditional intensities, the second-order conditional intensities allow examination of one component, either spatial or temporal, while holding the other component fixed.

Using notation similar to (3.1.6) and (3.1.7) we define the *average second-order spatial intensity* as

$$\lambda_2(\mathbf{s}_{i1}, \mathbf{s}_{j2}, dt_1, dt_2) = \lim_{|\mathbf{ds}_{i1}|, |\mathbf{ds}_{j2}| \rightarrow 0} \frac{E[N(\mathbf{ds}_{i1}, dt_1)N(\mathbf{ds}_{j2}, dt_2)]}{|\mathbf{ds}_{i1}||\mathbf{ds}_{j2}||dt_1||dt_2|} \quad (3.1.15)$$

and the *average second-order temporal intensity* as

$$\lambda_2(\mathbf{ds}_{i1}, \mathbf{ds}_{j2}, t_1, t_2) = \lim_{|dt_1|, |dt_2| \rightarrow 0} \frac{E[N(\mathbf{ds}_{i1}, dt_1)N(\mathbf{ds}_{j2}, dt_2)]}{|\mathbf{ds}_{i1}||\mathbf{ds}_{j2}||dt_1||dt_2|} \quad (3.1.16)$$

Combining the definitions in (3.1.13) and (3.1.15) an expression for *average conditional second-order spatial intensity* is given by

$$\lambda_2(\mathbf{ds}_{i*}, \mathbf{ds}_{j*} | t = t^*) = \frac{E[N(\mathbf{ds}_{i*}, t^*)N(\mathbf{ds}_{j*}, t^*)]}{|\mathbf{ds}_{i*}||\mathbf{ds}_{j*}|} \quad (3.1.17)$$

and an expression for *average conditional second-order temporal intensity* is given by

$$\lambda_2(dt_1, dt_2 | \mathbf{s} = \mathbf{s}^*) = \frac{E[N(\mathbf{s}^*, dt_1)N(\mathbf{s}^*, dt_2)]}{|dt_1||dt_2|} \quad (3.1.18)$$

Definitions for the second-order intensities are listed in Table 3.2.

As with the first-order spatiotemporal intensities, certain second-order spatiotemporal intensities may not be appropriate for all spatiotemporal point processes. We will use similar judgement noted in Section 3.1.1 to determine which second-order intensity should be emphasized for a particular process.

Table 3.2: Second-Order Intensity Measures.

Notation	Description	Equation No.
$\lambda_2(\mathbf{s}_{i1}, \mathbf{s}_{j2}, t_1, t_2)$	General spatiotemporal 2 nd -order intensity	3.1.10
$\lambda_2(\mathbf{s}_i, \mathbf{s}_j, \cdot, \cdot)$	Marginal 2 nd -order spatial intensity	3.1.11
$\lambda_2(\cdot, \cdot, t_1, t_2)$	Marginal 2 nd -order temporal intensity	3.1.12
$\lambda_2(\mathbf{s}_{i*}, \mathbf{s}_{j*} t)$	Conditional 2 nd -order spatial intensity	3.1.13
$\lambda_2(t_1, t_2 \mathbf{s})$	Conditional 2 nd -order temporal intensity	3.1.14
$\lambda_2(\mathbf{s}_{i1}, \mathbf{s}_{j2}, dt_1, dt_2)$	Average 2 nd -order spatial intensity	3.1.15
$\lambda_2(ds_{i1}, ds_{j2}, t_1, t_2)$	Average 2 nd -order temporal intensity	3.1.16
$\lambda_2(ds_{i*}, ds_{j*} t)$	Average conditional 2 nd -order spatial intensity	3.1.17
$\lambda_2(dt_1, dt_2 \mathbf{s})$	Average conditional 2 nd -order temporal intensity	3.1.18

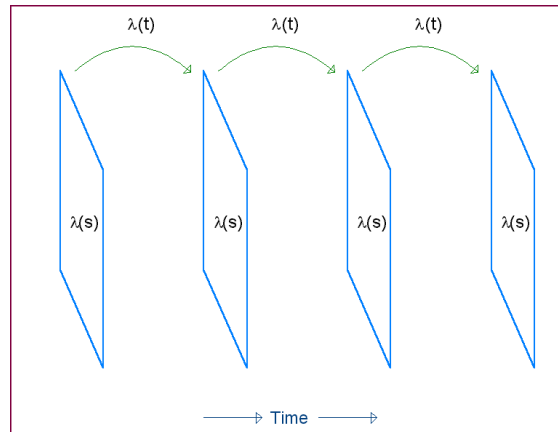


Figure 3.1: Intensities for a spatiotemporal process that is first-order stationary in space $\{\lambda(t|\mathbf{s}) \equiv \lambda(t)\}$ and time $\{\lambda(\mathbf{s}|t) \equiv \lambda(\mathbf{s})\}$. If $\lambda(t) = \lambda(\mathbf{s}) \equiv \lambda$ (constant), then the spatiotemporal process is first-order stationary in both space and time.

3.1.3 Second-Order (Weak) Stationarity

In this section we extend Cressie's (1993) definition of second-order stationarity to a spatiotemporal point pattern.

First-Order Stationarity

DEFINITION 3.1 (FIRST-ORDER STATIONARITY IN SPACE)

A spatiotemporal point pattern $Z(\mathbf{s}, t)$ is first-order stationary in space if (3.1.5) reduces to

$$\lambda(t|\mathbf{s}) \equiv \lambda(t). \quad (3.1.19)$$

Definition 3.1 implies the conditional temporal intensity does not depend on location.

DEFINITION 3.2 (FIRST-ORDER STATIONARITY IN TIME)

A spatiotemporal point pattern $Z(\mathbf{s}, t)$ is first-order stationary in time if (3.1.4) reduces to

$$\lambda(\mathbf{s}|t) \equiv \lambda(\mathbf{s}). \quad (3.1.20)$$

Definition 3.2 implies the conditional spatial intensity does not depend on time.

DEFINITION 3.3 (FIRST-ORDER SPATIOTEMPORAL STATIONARITY)

A spatiotemporal point pattern $Z(\mathbf{s}, t)$ is first-order stationary in space and time if (3.1.1) reduces to

$$\lambda(\mathbf{s}, t) \equiv \lambda. \quad (3.1.21)$$

Definition 3.3 implies that the full spatiotemporal intensity depends on neither time nor location. Theorem 3.1 shows the relationships among the full and conditional intensities. Corollaries 3.1 and 3.2 extends the results of the Theorem to show (3.1.19) and (3.1.20), respectively. Figure 3.1.3 shows the relationship of (3.1.19) and (3.1.20) for a spatiotemporal process.

THEOREM 3.1 (FULL AND CONDITIONAL FIRST-ORDER INTENSITIES)

The expressions for full spatiotemporal and conditional intensity given by (3.1.1) and (3.1.4), respectively, are related through the following integral:

$$\lim_{|dt| \rightarrow 0} \int_{dt} \frac{\lambda(\mathbf{s}|v)}{|dt|} dv = \lim_{|ds| \rightarrow 0} \int_{ds} \frac{\lambda(t|\mathbf{u})}{|ds|} d\mathbf{u} = \lambda(\mathbf{s}, t).$$

PROOF OF THEOREM 3.1

We begin by proving equivalency of the first integral (conditioning on time) to the spatiotemporal intensity. For simplicity of notation we will use $\mu(\cdot, \cdot) = E[N(\cdot, \cdot)]$.

$$\begin{aligned} \lim_{|dt| \rightarrow 0} \int_{dt} \frac{\lambda(\mathbf{s}|v)}{|dt|} dv &= \lim_{|dt| \rightarrow 0} \int_{dt} \lim_{|ds| \rightarrow 0} \frac{\mu(ds, v)}{|ds||dt|} dv \\ &= \lim_{\substack{|ds| \rightarrow 0 \\ |dt| \rightarrow 0}} \frac{1}{|ds||dt|} \int_{dt} \mu(ds, v) dv \end{aligned} \quad (3.1.22)$$

$$= \lim_{\substack{|ds| \rightarrow 0 \\ |dt| \rightarrow 0}} \frac{1}{|ds||dt|} \left\{ \lim_{k \rightarrow \infty} \frac{1}{k} \sum_{j=0}^k \mu \left(ds, t - \frac{\delta}{2} + \frac{\delta j}{k} \right) \right\} \quad (3.1.23)$$

$$\begin{aligned} &= \lim_{\substack{|ds| \rightarrow 0 \\ |dt| \rightarrow 0}} \frac{\mu(ds, dt)}{|ds||dt|} \quad (3.1.24) \\ &= \lambda(\mathbf{s}, t) \end{aligned}$$

The integral in (3.1.22) is replaced by a sum in (3.1.23). The value of each element in the sum represents the expected number of events in the interval $\left(t - \frac{\delta}{2} + \frac{\delta j}{k}, t - \frac{\delta}{2} + \frac{\delta(j+1)}{k} \right]$ (Figure 3.1.3a). Because the sum of the expectations of non-overlapping intervals is the expectation of the sum, (3.1.23) reduces to (3.1.24). The equivalency of the second integral (conditioning on space) can be proved in a similar fashion. *Q.E.D.*

COROLLARY 3.1

For a spatiotemporal point process that is first-order stationary in time,

$$\lambda(\mathbf{s}, t) \equiv \lambda(\mathbf{s}).$$

PROOF OF COROLLARY 3.1

From Theorem 3.1 we have

$$\lambda(\mathbf{s}, t) = \lim_{|dt| \rightarrow 0} \int_{dt} \frac{\lambda(\mathbf{s}|v)}{|dt|} dv. \quad (3.1.25)$$

From the Definition 3.2 we have $\lambda(\mathbf{s}|t) \equiv \lambda(\mathbf{s})$ for first-order temporal stationarity. Substi-

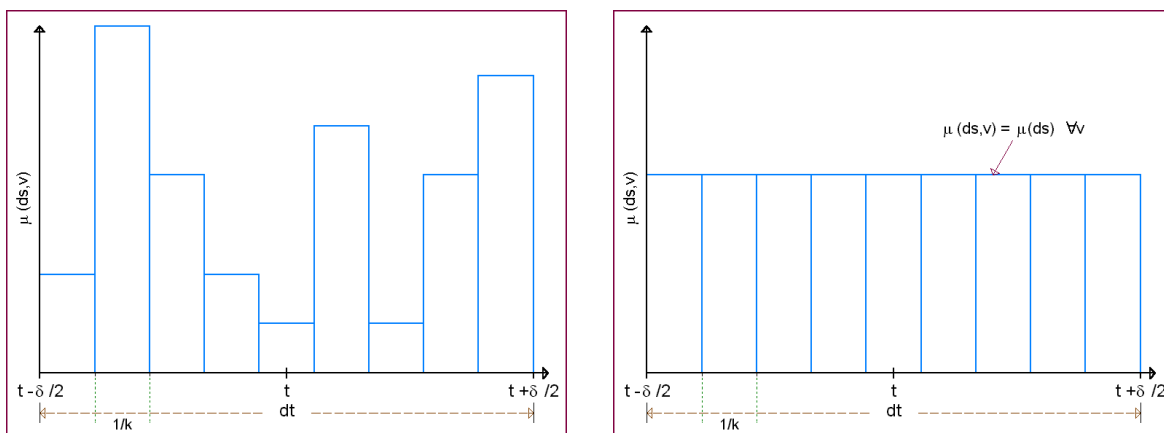


Figure 3.2: Graphical representation of Theorem 3.1 and Corollary 3.1.

- a. Integration of conditional intensity over dt .
- b. Integration of constant conditional intensity over dt .

tuting the latter expression into (3.1.25) we get

$$\lambda(\mathbf{s}, t) = \lim_{|dt| \rightarrow 0} \int_{dt} \frac{\lambda(\mathbf{s})}{|dt|} dv = \lambda(\mathbf{s}) \lim_{|dt| \rightarrow 0} \int_{dt} \frac{1}{|dt|} dv = \lambda(\mathbf{s}).$$

Q.E.D.

COROLLARY 3.2

For a spatiotemporal point process that is first-order stationary in space,

$$\lambda(\mathbf{s}, t) \equiv \lambda(t).$$

PROOF OF COROLLARY 3.2

A similar proof is constructed as in Corollary 3.1 except replacing space with time. *Q.E.D.*

COROLLARY 3.3

For a spatiotemporal point process that is first-order stationary in time,

$$\lambda(\mathbf{s}, \cdot) \equiv |T|\lambda(\mathbf{s}),$$

where $\lambda(\mathbf{s}, \cdot)$ is the marginal spatial intensity given by (3.1.2).

PROOF OF COROLLARY 3.3

Using Corollary 3.1 and Definition 3.2 we substitute $\lambda(\mathbf{s}, t) \equiv \lambda(\mathbf{s})$ into (3.1.2):

$$\lambda(\mathbf{s}, \cdot) = \int_T \lambda(\mathbf{s}) dt = \lambda(\mathbf{s}) \int_T dt = |T| \lambda(\mathbf{s}).$$

Q.E.D.

COROLLARY 3.4

For a spatiotemporal point process that is first-order stationary in space,

$$\lambda(\cdot, t) \equiv |A| \lambda(t),$$

where $\lambda(\cdot, t)$ is the marginal temporal intensity given by (3.1.3).

PROOF OF COROLLARY 3.4

A similar proof is constructed as in Corollary 3.3 except replacing space with time. *Q.E.D.*

Second-Order Stationarity

DEFINITION 3.4 (SECOND-ORDER STATIONARITY IN SPACE)

A spatiotemporal point process $Z(\mathbf{s}, t)$ is second-order stationary in space if (3.1.19) holds and (3.1.13) reduces to

$$\lambda_2(\mathbf{s}_{it}, \mathbf{s}_{jt}|t) \equiv \lambda_2(\mathbf{s}_{it} - \mathbf{s}_{jt}|t) = \lambda_2(\mathbf{h}|t), \quad (3.1.26)$$

so that the second-order conditional spatial intensity depends only on the absolute difference between locations. If a spatiotemporal process is second-order stationary in space and invariant under rotation then (3.1.26) reduces to an isotropic second-order intensity given by

$$\lambda_2(\mathbf{s}_{it}, \mathbf{s}_{jt}|t) \equiv \lambda_2(\|\mathbf{s}_{it} - \mathbf{s}_{jt}\||t) = \lambda_2(h|t), \quad (3.1.27)$$

where h is the Euclidean distance between any two arbitrary locations.

DEFINITION 3.5 (SECOND-ORDER STATIONARITY IN TIME)

A spatiotemporal point process $Z(\mathbf{s}, t)$ is second-order stationary in time if (3.1.20) holds and (3.1.14) reduces to

$$\lambda_2(t_1, t_2 | \mathbf{s}) \equiv \lambda_2(t_1 - t_2 | \mathbf{s}) = \lambda_2(k | \mathbf{s}), \quad (3.1.28)$$

so that the second-order conditional temporal intensity depends only on time lag k . Furthermore, we will require $\lambda_2(k | \mathbf{s}) = \lambda_2(-k | \mathbf{s})$.

DEFINITION 3.6 (SECOND-ORDER SPATIOTEMPORAL STATIONARITY)

A spatiotemporal process $Z(\mathbf{s}, t)$ is second-order stationary in both space in time if (3.1.21) holds and (3.1.10) reduces to

$$\lambda_2(\mathbf{s}_{i1}, \mathbf{s}_{j2}, t_1, t_2) \equiv \lambda_2(\mathbf{h}, k), \quad (3.1.29)$$

so that the full second-order spatial intensity depends only on the absolute difference between locations and the time lag. An isotropic second-order intensity of for a stationary spatiotemporal point process is given by

$$\lambda_2(\mathbf{h}, k) \equiv \lambda_2(h, k).$$

Extending Bartlett's definition of a covariance density function defined by (2.1.16) to a stationary orderly spatiotemporal point process we get

$$\lim_{|A_{i1}|, |A_{j2}| \rightarrow 0} \frac{\text{cov}[N(A_{i1}), N(A_{j2})]}{|A_{i1}| |A_{j2}|} = v(\mathbf{h}, k) + \lambda \delta(\mathbf{h}, k), \quad (3.1.30)$$

where $A_{i1} = d\mathbf{s}_{i1} \times dt_1$, $A_{j2} = d\mathbf{s}_{j2} \times dt_2$, $v(\mathbf{h}, k) = \lambda_2(\mathbf{h}, k) - \lambda^2$, and $\delta(\mathbf{h}, k)$ is a multidimensional Dirac delta-function defined by (2.1.18). As noted this representation assumes we

have an orderly process in space and in time. Specifically, we require

$$\lim_{|ds||dt| \rightarrow 0} P[N(ds, dt) > 1] = 0$$

for all \mathbf{s} and t , so that $E[N(ds, dt)^2] = E[N(ds, dt)]$ in limit.

Intensities under CSTR

The simplest spatiotemporal point process is that of CSTR in which the process is void of spatial and temporal structure (see Section 1.4.1). Under CSTR, the underlying process is assumed to be a Poisson process in space and time or uniform if conditioned on the number of events n (see Diggle (1983) for the CSR analog). In either case, the first- and second-order spatiotemporal intensities reduce to constants. The latter result is proven in Theorem 3.2.

THEOREM 3.2 (SPATIOTEMPORAL POISSON PROCESS)

Let

$$N(A, T) \sim \text{Poisson}(\lambda|A \times T|),$$

where $N()$ is a counting measure on the region A and time T and $|\cdot|$ is Lesbesgue measure. Then, the first-order spatiotemporal intensity reduces to

$$\lambda(\mathbf{s}, t) \equiv \lambda$$

and the second-order spatiotemporal intensity reduces to

$$\lambda_2(\mathbf{s}_{i1}, \mathbf{s}_{j2}, t_1, t_2) \equiv \lambda^2. \quad (3.1.31)$$

PROOF OF THEOREM 3.2

To show the first-order intensity is constant we use the intensity measure of a Poisson process:

$$\lambda(\mathbf{s}, t) = \lim_{|ds|, |dt| \rightarrow 0} \frac{E[N(ds, dt)]}{|ds||dt|} = \lim_{|ds|, |dt| \rightarrow 0} \frac{\lambda|ds||dt|}{|ds||dt|} = \lambda.$$

To show the second-order intensity is constant we must show independence of events in nonoverlapping regions. Let $X = A_1 \times T_1$ and $Y = A_2 \times T_2$ be two disjoint volumes in space-time, and $Z = X \cup Y$ be their union. Then, for $p = |X|/|Z|$ and $q = |Y|/|Z|$ we define the conditional probability of $N(X) + N(Y) = n$ as

$$P[N(X) = x, N(Y) = y | N(Z) = n] = \binom{x+y}{x} p^x q^y \quad \text{for } 0 \leq x \leq n, y = n - x.$$

Thus, the unconditional probability is obtained by

$$\begin{aligned} P[N(X) = x, N(Y) = y] &= P[N(X) = x, N(Y) = y | N(Z) = n] \cdot P[N(Z) = n] \\ &= \left\{ \binom{x+y}{x} p^x q^y \right\} \left\{ \frac{e^{-\lambda|Z|} (\lambda|Z|)^n}{n!} \right\} \\ &= \frac{1}{x!y!} \left(\frac{|X|}{|Z|} \right)^x \left(\frac{|Y|}{|Z|} \right)^y e^{-\lambda(|X|+|Y|)} (\lambda|Z|)^x (\lambda|Z|)^y \\ &= \left\{ \frac{e^{-\lambda|X|} (\lambda|X|)^x}{x!} \right\} \left\{ \frac{e^{-\lambda|Y|} (\lambda|Y|)^y}{y!} \right\} \\ &= P[N(X) = x] \cdot P[N(Y) = y]. \end{aligned}$$

Therefore, if we have a spatiotemporal Poisson process, $N(X)$ and $N(Y)$ are independent for $X \cap Y = \emptyset$. It follows then, for infinitesimal regions $A_{i1} = d\mathbf{s}_{i1} \times dt_1$ and $A_{j2} = d\mathbf{s}_{j2} \times dt_2$, that

$$\begin{aligned} \lambda_2(\mathbf{s}_{i1}, \mathbf{s}_{j2}, t_1, t_2) &= \lim_{|A_{i1}|, |A_{j2}| \rightarrow 0} \frac{E[N(A_{i1})N(A_{j2})]}{|A_{i1}||A_{j2}|} \\ &= \lim_{|A_{i1}|, |A_{j2}| \rightarrow 0} \frac{E[N(A_{i1})]}{|A_{i1}|} \frac{E[N(A_{j2})]}{|A_{j2}|} \\ &= \lambda^2. \end{aligned} \tag{3.1.32}$$

Since A_{i1} and A_{j2} are infinitesimally small, we can assume that $A_{i1} \cap A_{j2} = \emptyset$. It follows then that the expectation of the product becomes the product of the expectations in (3.1.32) by independence. *Q.E.D.*

Because the first- and second-order intensities are constants, it is clear that the spatiotemporal Poisson process meets the requirements for second-order stationarity defined in this section. Furthermore, from (3.1.31) we see that (3.1.30) reduces to

$$v(\mathbf{h}, k) + \lambda\delta(\mathbf{h}, k) = [\lambda_2(\mathbf{h}, k) - \lambda^2] + \lambda\delta(\mathbf{h}, k) = \lambda\delta(\mathbf{h}, k)$$

so that the covariance is 0 among all the events in the process.

3.1.4 Reduced Second-Order Intensity

In this section, the K -function introduced in Section 2.1.2 is extended to incorporate both distance and time lag. We will use the second-order spatiotemporal intensities defined in Section 3.1.2 to construct conditional K -functions as well as a full spatiotemporal K -function. The conditional K -functions will be useful when the full spatiotemporal K -function is unattainable due to the stationarity assumption that will be required.

We first extend Ripley's K -function to a spatiotemporal point process through the conditional second order intensities defined in Section 3.1.2. Conditioning on time we obtain the *conditional spatial K -function* given by

$$\begin{aligned} \lambda(t)K(h|t) &= E[\text{number of extra events within a distance } h \\ &\quad \text{of an arbitrary event at time } t] \\ &= \int_0^{2\pi} \int_0^h \{\lambda_2(x|t)/\lambda(t)\} x dx d\theta \\ &= \frac{2\pi}{\lambda(t)} \int_0^h \lambda_2(x|t) x dx, \end{aligned} \tag{3.1.33}$$

where $\lambda(t)$ and $\lambda_2(h|t)$ are given in (3.1.19) and (3.1.27), respectively. As with the spatial K -function given by (2.1.4) we require the process to be second-order stationary in space and isotropic. (3.1.33) is identical to (2.1.4) constructed for all $t \in T$. Thus, it follows that if the point pattern is CSR at time t , then $\lambda(h|t) \equiv [\lambda(t)]^2$, where $\lambda(t)$, and the conditional

spatial K -function reduces to

$$K(h|t) = \frac{2\pi}{[\lambda(t)]^2} \int_0^h \underbrace{\lambda_2(x|t)}_{[\lambda(t)]^2} x dx \stackrel{CSR}{\equiv} \pi h^2.$$

Conditioning on space we obtain the *conditional temporal K -function* given by

$$\begin{aligned} \lambda(\mathbf{s})K(k|\mathbf{s}) &= E[\text{number of extra events within time lag } k \\ &\quad \text{of an arbitrary event at location } \mathbf{s}] \\ &= \int_{-k/2}^{k/2} \frac{\lambda_2(v|\mathbf{s})}{\lambda(\mathbf{s})} dv \\ &= \frac{1}{\lambda(\mathbf{s})} \int_{-k/2}^{k/2} \lambda_2(v|\mathbf{s}) dv, \end{aligned} \tag{3.1.34}$$

where $\lambda(\mathbf{s})$ and $\lambda_2(k|\mathbf{s})$ are defined by (3.1.20) and (3.1.28), respectively. Similarly to the spatial K -function, the conditional temporal K -function requires the process to be second-order stationary in time.

The conditional temporal K -function will only be useful for cases in which the temporal component is stochastic (e.g. earthquake or explosion processes). Calculating (3.1.34) may also require that the location \mathbf{s} be a region, say $d\mathbf{s}$, rather than a single event. This is because for locations \mathbf{s} with continuous coordinates, the probability of observing an event at location \mathbf{s} for times t_1 and t_2 is zero. If such is the case the spatial intensity $\lambda(\mathbf{s})$ can be replaced with the average spatial intensity $\lambda(d\mathbf{s})$.

If events occur at location \mathbf{s} (or region $d\mathbf{s}$) according to a Poisson process, then the second-order temporal intensity reduces to the squared first-order temporal intensity: $\lambda_2(k|\mathbf{s}) \equiv [\lambda(\mathbf{s})]^2$ [Daley and Vere-Jones, 1988]. Thus, it follows that the conditional temporal K -function becomes

$$K(k|\mathbf{s}) = \frac{1}{[\lambda(\mathbf{s})]^2} \int_{-k/2}^{k/2} \underbrace{\lambda_2(v|\mathbf{s})}_{=[\lambda(\mathbf{s})]^2} dv \equiv k.$$

The extension of the estimator (2.1.14) to the general spatiotemporal K -function requires second-order stationarity in both space and time as well as an isotropic second-order intensity function. In order to define the K -function for both time and space we require that the process be second-order stationary and have an isotropic covariance density. We define two types of spatiotemporal K -functions depending on the type of process being studied. We distinguish among spatiotemporal point processes which have stochastic temporal components (earthquake and explosion processes) and deterministic temporal components (birth-death and sampled point patterns in time). Although in nature the birth-death process has an inherently stochastic temporal component in that events live for a random amount of time, the sampling structure of a birth-death process imposes a deterministic quality.

1. TYPE I (FOR EARTHQUAKE PROCESSES AND EXPLOSION PROCESSES)

The temporal component of earthquake and explosion processes is a stochastic process. For this reason, the spatiotemporal K -function to capture events over intervals of time rather than at discrete points. The spatiotemporal K -function defined by (3.1.35) counts all events in a cylinder with radius h (distance) and length k (time lag).

$$\begin{aligned}
 \lambda K_I(h, k) &= E[\text{number of extra events within a distance } h \\
 &\quad \text{within time lag } k \text{ of an arbitrary event}] \\
 &= \int_{-k/2}^{k/2} \int_0^{2\pi} \int_0^h \{\lambda_2(x, v)/\lambda\} x dx d\theta dv \\
 &= \frac{2\pi}{\lambda} \int_{-k/2}^{k/2} \int_0^h \lambda_2(x, v) x dx dv. \tag{3.1.35}
 \end{aligned}$$

2. TYPE II (FOR BIRTH-DEATH PROCESSES AND SAMPLED POINT PATTERNS IN TIME)

For birth-death processes and sampled point patterns in time, the temporal component is not a stochastic process and is usually discrete. For cases in which the temporal component is stochastic, the spatiotemporal K -function given by (3.1.35) should be used instead of the following K -function that counts all events distance h and time lag

k away from an arbitrary event.

$$\begin{aligned}
 \lambda K_{II}(h, k) &= E[\text{number of extra events within a distance } h \\
 &\quad \text{at time lag } k \text{ of an arbitrary event}] \\
 &= \int_0^{2\pi} \int_0^h \{\lambda_2(x, k)/\lambda\} x dx d\theta \\
 &= \frac{2\pi}{\lambda} \int_0^h [\lambda_2(x, k)] x dx.
 \end{aligned} \tag{3.1.36}$$

The fundamental difference between K_I and K_{II} is that K_I counts the number of events within a cylinder of length k and radius h , whereas K_{II} counts the number of events within a radius h at a chosen time lag k from an arbitrary event. The definition of $K_{II}(h, k)$ is similar in construction to the bivariate K -function given by Hanisch and Stoyan (1979) and Lotwick and Silverman (1982). The conceptual difference between K_I and K_{II} are illustrated in Figure 3.1.4.

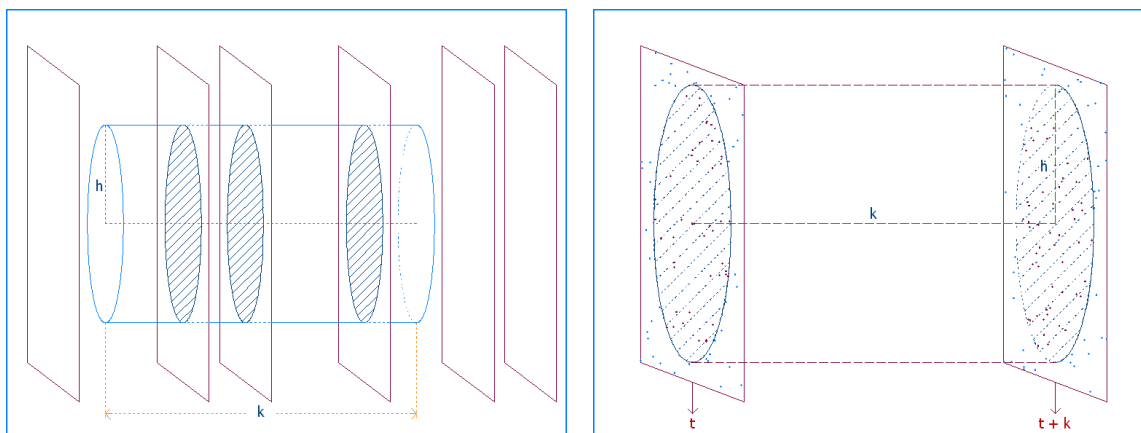


Figure 3.3: Illustrations of how spatiotemporal K functions are obtained. $K_I(h, k)$ (left) counts the number of points in a cylinder of length k and radius h . $K_{II}(h, k)$ (right) counts the number of points distance h and time lag k away from an arbitrary event.

From Theorem 3.2 we see that $\lambda_2(h, k) \equiv \lambda^2$ if the spatiotemporal process is CSTR. In this

case we have

$$K_I(h, k) = \frac{2\pi}{\lambda^2} \int_{-k/2}^{k/2} \int_0^h \underbrace{\lambda_2(x, v)}_{=\lambda^2} dx dv \stackrel{CSTR}{\equiv} \pi h^2 k \quad (3.1.37)$$

and

$$K_{II}(h, k) = \frac{2\pi}{\lambda^2} \int_0^h \underbrace{\lambda_2(x, k)}_{=\lambda^2} dx \stackrel{CSTR}{\equiv} \pi h^2. \quad (3.1.38)$$

3.1.5 Estimation of Intensities

Extending the estimation of $\lambda(\cdot)$, $\lambda_2(\cdot)$, and $K(\cdot)$ from the spatial to the spatiotemporal case is a matter of taking expected values over a volume as opposed to an area. However, since there may exist different intensities for the spatial and temporal components, estimates must be constructed individually. Furthermore, a requirement for estimation of $K(\cdot)$ will be that the process is stationary both spatially and temporally as well as spatially isotropic.

First-order Intensity

Intensity estimators for spatiotemporal point processes are extensions of the Basic estimator (2.1.11), the Binning estimator (2.1.12), and the Kernel estimator (2.1.13, 1.4.2). The basic estimator assumes the spatiotemporal intensity is constant for all time and space: $\lambda(\mathbf{s}, t) \equiv \lambda$.

Hence,

$$\hat{\lambda} = \frac{n}{|A \times T|}, \quad (3.1.39)$$

where $n = \sum_t n_t$, T is the length of observed time, and A is the study region. Throughout, we assume the size of the study region A is constant for all $t \in T$. If a spatiotemporal point process is second-order stationary in both space and time (3.1.39) is an unbiased estimate of the first-order spatiotemporal intensity λ .

The spatiotemporal binning estimator is a direct three-dimensional analog of the (2.1.12).

$$\widehat{\lambda}(\mathbf{s}, t) = \sum_{j=1}^{\# \text{ bins}} \kappa_{\mathbf{s}} \left(\frac{\mathbf{s} - \mathbf{s}_j}{b_{\mathbf{s}}} \right) \kappa_t \left(\frac{t - t_j}{b_t} \right) \sum_{t^* \in T} \sum_{i=1}^{n_t} \frac{I[(\mathbf{s}_i, t^*) \in (d\mathbf{s}, dt)_j]}{|(d\mathbf{s}, dt)_j|}, \quad (3.1.40)$$

where $I(\cdot)$, $\kappa(\cdot)$, and b are as before and $|(d\mathbf{s}, dt)_j|$ is the size of the bin centered at $(\mathbf{s}, t)_j$.

Essentially, (3.1.40) is smoothed three-dimensional histogram.

An extension of (1.4.2) to incorporate all spatiotemporal point processes is given by

$$\begin{aligned} \widehat{\lambda}_{b_t, b_{\mathbf{s}}}(\mathbf{s}, t) &= \frac{1}{p_{b_{\mathbf{s}}}(\mathbf{s})p_{b_t}(t)} \sum_{t^* \in T} \sum_{i=1}^{n_{t^*}} \kappa_{\mathbf{s}} \left(\frac{\mathbf{s} - \mathbf{s}_{it^*}}{b_{\mathbf{s}}} \right) \kappa_t \left(\frac{t - t^*}{b_t} \right) \\ &= \frac{1}{p_{b_t}(t)} \sum_{t^* \in T} \kappa_t \left(\frac{t - t^*}{b_t} \right) \left[\frac{1}{p_{b_{\mathbf{s}}}(\mathbf{s})} \sum_{i=1}^{n_{t^*}} \kappa_{\mathbf{s}} \left(\frac{\mathbf{s} - \mathbf{s}_{it^*}}{b_{\mathbf{s}}} \right) \right] \\ &= \frac{1}{p_{b_t}(t)} \sum_{t^* \in T} \kappa_t \left(\frac{t - t^*}{b_t} \right) \widehat{\lambda}(\mathbf{s}|t^*), \end{aligned} \quad (3.1.41)$$

where $\kappa_*(\cdot)$, b_* , and $p_*(\cdot)$ are as before. From (3.1.41) we see that an estimate of the general spatiotemporal intensity is obtained by smoothing the smoothed conditional spatial intensity $\lambda(\mathbf{s}|t)$. Again, note that there is no reason for either the kernel functions or the bandwidths to be the same for the temporal and spatial components.

As with any kernel-type estimator, the choice of kernel is not as important as the choice of bandwidth [Scott, 1992]. At this time we leave these decisions to the user. Further research is required to make bandwidth selection a less subjective matter.

Reduced Second-Order Intensity

The extension of (2.1.14) to the K -functions defined by (3.1.33) and (3.1.34) are straightforward. Specifically, the conditional spatial K -function will be estimated in the same fashion

as (2.1.14):

$$\widehat{K}(h|t) = \widehat{\lambda}(t)^{-1} \sum_{i=1}^{n_t} \sum_{\substack{j=1 \\ i \neq j}}^{n_t} w_{ij}^{-1} \frac{I(\|\mathbf{s}_{it} - \mathbf{s}_{jt}\| < h)}{n_t}, \quad (3.1.42)$$

where

$$\widehat{\lambda}(t) = \frac{n_t}{|A|},$$

w_{ij} are edge-correction weights defined as before, n_t is the number of points observed at time t , and A is the study region. Because (3.1.42) is identical to (2.1.14) it follows that $\widehat{K}(h|t)$ is approximately unbiased for $K(h|t)$ for small h [Ripley, 1976]. The weights w_{ij} are also explicitly defined if A is a rectangular or circular region [Diggle, 1983].

The conditional temporal K -function will be similar in its construction:

$$\widehat{K}(k|\mathbf{s}) = \widehat{\lambda}(\mathbf{s})^{-1} \sum_{l=1}^{T-k} w_k \frac{I(\{\mathbf{s}_{*l} \in A_l\} \cap \{\mathbf{s}_{*(l+k)} \in A_{l+k}\})}{(T-k)n_{\mathbf{s}}} \quad (3.1.43)$$

where $\widehat{\lambda}(\mathbf{s})$ is given by

$$\widehat{\lambda}(\mathbf{s}) = \frac{1}{T} \sum_{t=1}^T \widehat{\lambda}(\mathbf{s}, t), \quad (3.1.44)$$

$n_{\mathbf{s}}$ is the number of points at location \mathbf{s} over the interval $0 \leq t \leq T$, and $\widehat{\lambda}(\mathbf{s}, t)$ is some estimator of the spatiotemporal intensity (e.g. kernel). Because the estimate of $\lambda(\mathbf{s})$ depends on a possibly biased estimate of the spatiotemporal intensity, (3.1.43) may be biased.

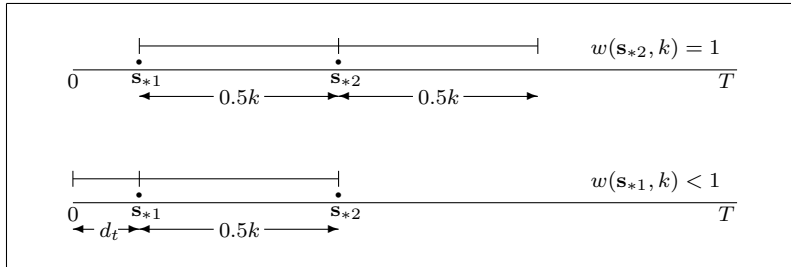


Figure 3.4: Determining w_k for the conditional temporal K -function.

The edge-correction weight is a one-dimensional analog to the weights defined by Diggle (1983) for two-dimensional point processes. Specifically, $w_k = w(\mathbf{s}, k)$ is defined as the

proportion of a line of length k centered at \mathbf{s} , with an endpoint passing through \mathbf{s}_{*k} and inside the study region $(0, T)$ (Figure 3.1.5). An explicit definition of w_k is given by

$$w(\mathbf{s}, k) = \frac{0.5k + \min(d_t, 0.5k)}{k}, \quad (3.1.45)$$

where $d_t = \min(t, T - t)$ is the distance (in time) \mathbf{s} is away from the edge.

For both spatiotemporal K -functions given by (3.1.35) and (3.1.36), an edge-correction factor w_{ijlm} is used. The weights need to be defined differently for each K -function, though they are both extensions of the weights used in (2.1.14). Both estimates of the spatiotemporal K -functions use the arguments provided by Diggle (1983) to build an approximately unbiased estimate of the spatial K -function.

1. TYPE I (FOR EARTHQUAKE PROCESSES AND EXPLOSION PROCESSES)

If the process is second-order stationarity then the expected number of points in region $A \times T$ is $\lambda|A \times T|$ where λ is the first-order spatiotemporal intensity. It follows then that the expected number of ordered pairs of events at most distance h apart and k time lag away is

$$\lambda|A \times T|[\lambda K_I(h, k)] = \lambda^2|A \times T|K_I(h, k). \quad (3.1.46)$$

Thus, an estimate of (3.1.46) counts all the ordered pairs less than h distance apart and within k time lags away and is given with an edge correction weight w_{ijlm} by

$$\lambda^2|A \times T|\widehat{K}_I(h, k) = \frac{1}{|T|} \sum_{l=1}^T \sum_{m \in (l \pm k/2)} \sum_{i=1}^{n_l} \sum_{j=1}^{n_m} w_{ijlm}^{-1} I(\|\mathbf{s}_{il} - \mathbf{s}_{jm}\| < h), \quad (3.1.47)$$

where $(il) \neq (jm)$.

The estimator given by (3.1.47) counts the number of points within a cylinder centered at \mathbf{s}_{it} with radius h and length k . Solving (3.1.47) for $\widehat{K}_I(h, k)$ and replacing λ with

the basic spatiotemporal estimate given by (3.1.39) we get

$$\begin{aligned}\widehat{K}_I(h, k) &= n^{-2} \frac{|A \times T|}{|T|} \sum_{l=1}^T \sum_{m \in (l \pm k/2)} \sum_{i=1}^{n_l} \sum_{j=1}^{n_m} w_{ijlm}^{-1} I(\|\mathbf{s}_{il} - \mathbf{s}_{jm}\| < h) \\ &= \widehat{\lambda}^{-1} \sum_{l=1}^T \sum_{m \in (l \pm k/2)} \sum_{i=1}^{n_l} \sum_{j=1}^{n_m} w_{ijlm}^{-1} \frac{I(\|\mathbf{s}_{il} - \mathbf{s}_{jm}\| < h)}{n|T|},\end{aligned}\quad (3.1.48)$$

where n is the total sample size and w_{ijlm} are edge-correction weights.

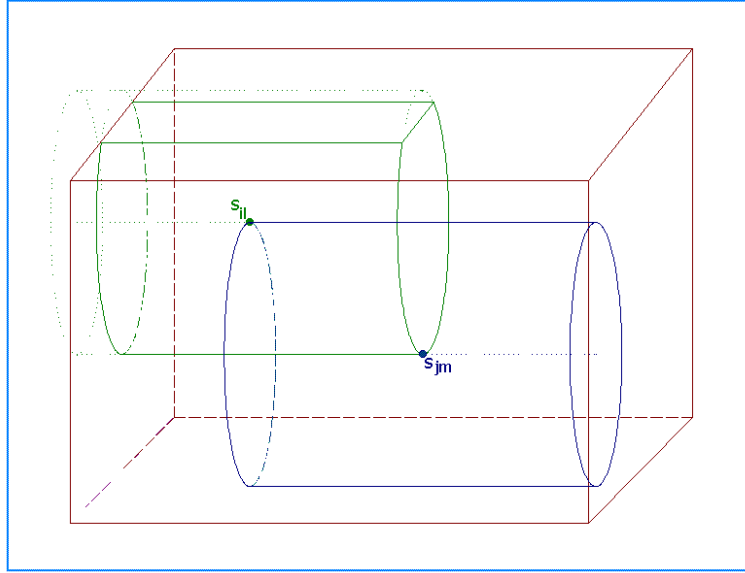


Figure 3.5: Determining w_{ijlm} for the Type I spatiotemporal K -function.

The edge-correction weights for $\widehat{K}_I(h, k)$ are defined by the proportion of the surface area of a cylinder centered at \mathbf{s}_{il} , passing through \mathbf{s}_{jm} , and inside the study region $A \times T$ (Figure 1). As with the weights for the spatial K -function, the w_{ijlm} 's can be determined explicitly when the study region A is rectangular. We will restrict ourselves to A rectangular as this will be a requirement of the periodogram analysis of spatiotemporal point processes introduced in Section 3.2.

For a rectangular study region A with coordinates $(0, L_x) \times (0, L_y)$, let $d_x = \min(s_x, L_x - s_x)$ and $d_y = \min(s_y, L_y - s_y)$, for some event $\mathbf{s} = (s_x, s_y) \in A \times T$. Thus, d_x and d_y are distances from \mathbf{s} to the nearest vertical and horizontal (spatial) edges of A . We

further define, for temporal region $(0, T)$, $d_t = \min(t, T - t)$ as the distance in time \mathbf{s} is separated from the (temporal) edge. Combining the weights for the conditional temporal K -function given by (3.1.45) and the weights for the spatial K -function given by Diggle (1983) we define $w_{ijlm} = w(\mathbf{s}, h, k)$ as the weight determined for location \mathbf{s} . As in Diggle (1983), we consider two cases:

(a) For $h^2 \leq d_x^2 + d_y^2$:

$$w(\mathbf{s}, h, k) = w(\mathbf{s}, k) \left\{ 1 - \pi^{-1} [\cos^{-1} \{ \min(d_x, h)/h \} + \cos^{-1} \{ \min(d_y, h)/h \}] \right\}$$

(b) For $h^2 > d_x^2 + d_y^2$:

$$w(\mathbf{s}, h, k) = w(\mathbf{s}, k) \left\{ 0.75 - (2\pi)^{-1} \{ \cos^{-1}(d_x/h) + \cos^{-1}(d_y/h) \} \right\},$$

where $w(\mathbf{s}, k)$ is given by (3.1.45).

2. TYPE II (FOR BIRTH-DEATH PROCESSES AND SAMPLED POINT PATTERNS IN TIME)

Although the temporal sampling for the birth-death process and sampled point patterns in time are typically deterministic, the second-order stationarity assumption allows us to find an estimate for $K_{II}(h, k)$ in the same fashion as for $K_I(h, k)$. Specifically, extending Diggle's argument for the spatial K -function we note that the expected number of points in the space-time region $A \times T$ is still $\lambda|A \times T|$ where λ is the first-order spatiotemporal intensity. As with $K_I(h, k)$, we expect the number of ordered pairs of events at most distance h apart and at time lag k to be

$$\lambda|A \times T|[\lambda K_{II}(h, k)] = \lambda^2|A \times T|K_{II}(h, k). \quad (3.1.49)$$

Thus, an estimate of (3.1.49) counts all the ordered pairs less than h distance apart

and k time lags away and is given with an edge correction weight w_{ijlm} by

$$\lambda^2 |A \times T| \widehat{K}_{II}(h, k) = \sum_{\substack{m=1 \\ l=m+k}}^{T-k} \sum_{i=1}^{n_l} \sum_{j=1}^{n_m} w_{ijlm}^{-1} \frac{I(\|\mathbf{s}_{il} - \mathbf{s}_{jm}\| < h)}{(T-k)}, \quad (3.1.50)$$

where $(il) \neq (jm)$. The estimator given by (3.1.50) counts the number of points on the face of a cylinder centered at \mathbf{s}_{im} with radius h and height k . Solving (3.1.50) for $\widehat{K}_{II}(h, k)$ and replacing λ with the basic spatiotemporal estimate given by (3.1.39) we get

$$\begin{aligned} \widehat{K}_{II}(h, k) &= \frac{n^{-2}}{|A \times T|} \sum_{\substack{m=1 \\ l=m+k}}^{T-k} \sum_{i=1}^{n_l} \sum_{j=1}^{n_m} w_{ijlm}^{-1} \frac{I(\{\|\mathbf{s}_{il} - \mathbf{s}_{jm}\| < h\})}{(T-k)} \\ &= \widehat{\lambda}^{-1} \sum_{\substack{m=1 \\ l=m+k}}^{T-k} \sum_{i=1}^{n_l} \sum_{j=1}^{n_m} w_{ijlm}^{-1} \frac{I(\{\|\mathbf{s}_{il} - \mathbf{s}_{jm}\| < h\})}{n(T-k)}, \end{aligned} \quad (3.1.51)$$

where n is the total sample size.

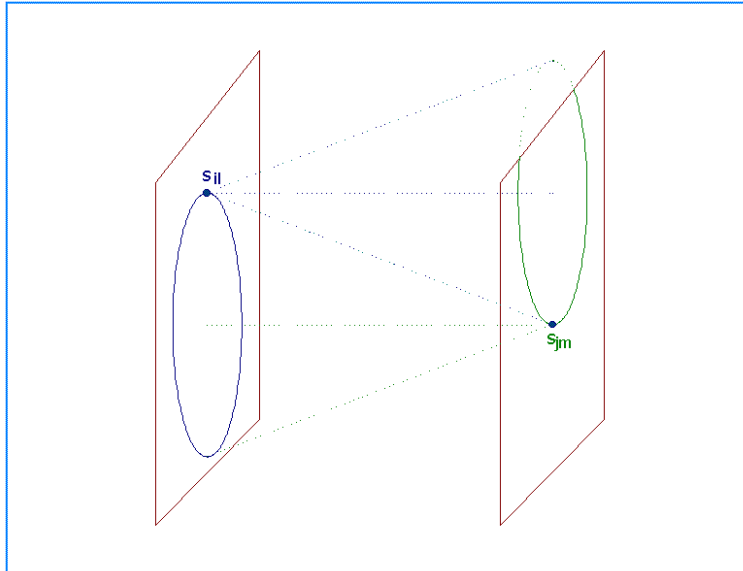


Figure 3.6: Determining w_{ijlm} for the Type II spatiotemporal K -function.

The edge-correction weights for $\widehat{K}_{II}(h, k)$ are defined by the proportion of the area of

a disc centered at \mathbf{s}_{il} , passing through \mathbf{s}_{jm} , and inside the study region A (Figure 2). Since we are not considering volumes for $K_{II}(h, k)$ but rather surface areas of discs, a temporal edge-correction is not required. For this reason, the weights are identical to the weights defined in Section 2.1.3.

As noted above, if the process is assumed to be first-order stationary in both space and time, the most natural estimator for the intensity λ is the basic spatiotemporal estimator given by (3.1.39). Furthermore, the estimates in (3.1.47) and (3.1.50) are divided by the factor $|T|$ and $(T - k)$ to average over all possible lags.

\widehat{K}_I and \widehat{K}_{II} are approximately unbiased for K_I and K_{II} , respectively, for small h and k provided K_I and K_{II} are independent of n , the total number of events in the point pattern. Unbiasedness is shown in Theorems 3.3 and 3.4.

THEOREM 3.3 (EXPECTED VALUE OF K_I)

For some $h < h_{\max}$ and $k < k_{\max}$, if n is independent of $K_I(h, k)$, $\widehat{K}_I(h, k)$ is an unbiased estimator for $K_I(h, k)$. In other words, if n is independent of $K_I(h, k)$ then

$$E[\widehat{K}_I(h, k)] = K_I(h, k)$$

for small h and k .

PROOF OF THEOREM 3.3

To show the approximate unbiasedness of $\widehat{K}_I(h, k)$ we extend the proof by Ripley (1976) for spatial point patterns. Let $\widehat{K}_I(h, k)$ be defined by (3.1.47), then

$$\begin{aligned} E[\widehat{K}_I(h, k)] &= E\left[\widehat{\lambda}^{-1} \sum_{m=1}^T \sum_{l \in (m \pm k/2)} \sum_{i=1}^{n_l} \sum_{j=1}^{n_m} w_{ijlm}^{-1} \frac{I(\|\mathbf{s}_{il} - \mathbf{s}_{jm}\| < h)}{n|T|}\right] \\ &= E\left[\frac{1}{n\widehat{\lambda}}\right] E\left[\sum_{m=1}^T \sum_{l \in (m \pm k/2)} \sum_{i=1}^{n_l} \sum_{j=1}^{n_m} w_{ijlm}^{-1} \frac{I(\|\mathbf{s}_{il} - \mathbf{s}_{jm}\| < h)}{|T|}\right] \\ &= \frac{|A \times T|}{\lambda^2 |A \times T|^2} \{\lambda^2 |A \times T| K_I(h, k)\} \quad \text{by (3.1.46)} \\ &= K_I(h, k). \end{aligned}$$

The requirement for h and k to be small comes from $w_{ijlm}^{-1} = 1$ when \mathbf{s}_{il} and \mathbf{s}_{jm} are sufficiently far from the edge of the study region $A \times T$. However the weights w_{ijlm}^{-1} are unbounded as h and k increase. For small h and k , the unbiasedness is exact, whereas for large h and k , the unbiasedness is approximate. Q.E.D.

THEOREM 3.4 (EXPECTED VALUE OF K_{II})

For some $h < h_{\max}$ and $k < k_{\max}$, if n is independent of $K_{II}(h, k)$, $\widehat{K}_{II}(h, k)$ is an unbiased estimator for $K_{II}(h, k)$. In other words, if n is independent of $K_I(h, k)$ then

$$E[\widehat{K}_{II}(h, k)] = K_{II}(h, k)$$

for small h and k .

PROOF OF THEOREM 3.4

The proof is similar to the proof of Theorem 3.3. To show the approximate unbiasedness of $\widehat{K}_{II}(h, k)$ we extend the proof by Ripley (1976) for spatial point patterns. Let $\widehat{K}_{II}(h, k)$ be defined by (3.1.50), then

$$\begin{aligned} E[\widehat{K}_{II}(h, k)] &= E\left[\widehat{\lambda}^{-1} \sum_{l=m+k}^{T-k} \sum_{i=1}^{n_l} \sum_{j=1}^{n_m} w_{ijlm}^{-1} \frac{I(\{\|\mathbf{s}_{il} - \mathbf{s}_{jm}\| < h\})}{n(T-k)}\right] \\ &= E\left[\frac{1}{n\widehat{\lambda}}\right] E\left[\sum_{l=m+k}^{T-k} \sum_{i=1}^{n_l} \sum_{j=1}^{n_m} w_{ijlm}^{-1} \frac{I(\{\|\mathbf{s}_{il} - \mathbf{s}_{jm}\| < h\})}{n(T-k)}\right] \\ &= \frac{|A \times T|}{\lambda^2 |A \times T|^2} \{\lambda^2 |A \times T| K_{II}(h, k)\} \quad \text{by (3.1.49)} \\ &= K_{II}(h, k). \end{aligned}$$

As before, the requirement for h and k to be small comes from $w_{ijlm}^{-1} = 1$ when \mathbf{s}_{il} and \mathbf{s}_{jm} are sufficiently far from the edge of the study region $A \times T$. For small h and k , the unbiasedness is exact, whereas for large h and k , the unbiasedness is approximate. Q.E.D.

Inference based on the spatiotemporal K -function

In Theorems 3.3 and 3.4 we proved that the estimated spatiotemporal K -functions are approximately unbiased. Therefore it follows that if the spatiotemporal point process is CSTR then

$$E[\widehat{K}_I(h, k)] \stackrel{CSTR}{=} \pi h^2 k \quad \text{for } k > 0 \quad (3.1.52)$$

and

$$E[\widehat{K}_{II}(h, k)] \stackrel{CSTR}{=} \pi h^2. \quad (3.1.53)$$

Under CSTR the points are evenly distributed over time and space, without any interactions among spatiotemporal point patterns.

From (3.1.52) and (3.1.53) two spatiotemporal L -functions are given by

$$\widehat{L}_I(h, k) = \sqrt{\widehat{K}_I(h, k)/(\pi k)} \quad (3.1.54)$$

and

$$\widehat{L}_{II}(h, k) = \sqrt{\widehat{K}_{II}(h, k)/\pi} \quad (3.1.55)$$

so that $L_I(h, k) = h$ and $L_{II}(h, k) = h$ under the hypothesis of CSTR. As with the spatial L -function, L_I and L_{II} provide finer detail for analyzing a spatiotemporal point pattern.

To test a particular spatiotemporal pattern for CSTR using K -analysis, a simulated inference approach is taken. Specifically, the observed K -function (either Type I or II) is compared to the K -functions of B simulated CSTR patterns. Rejection of the CSTR hypothesis would follow if $K_{\text{obs}}(h_0, k_0) < K_{\text{min}}(h_0, k_0)$ or $K_{\text{obs}}(h_0, k_0) > K_{\text{max}}(h_0, k_0)$, where $(K_{\text{min}}(h_0, k_0), K_{\text{max}}(h_0, k_0))$ are the minimum and maximum obtained from the B simulated patterns for some distance h_0 and time lag k_0 . Generating CSTR patterns for the four types of spatiotemporal point patterns is discussed in Chapter 4.

3.2 Spectral Representation and Spatiotemporal Periodogram Analysis

In this section we will propose a periodogram of a spatiotemporal point process as an extension of Section 2.2. The methodology developed in this section is for regularly spaced time intervals, though extensions to irregularly spaced time (such as with earthquake and explosion processes) are straightforward.

As with the spatial periodogram, we require that the spatiotemporal point process be second-order stationary but not necessarily isotropic. We begin by extending the complete covariance function of Bartlett (1964). For $\lambda(\mathbf{s}, t) = \lambda$ and $\lambda_2(\mathbf{s}_{i1}, \mathbf{s}_{j2}, t_1, t_2) = \lambda_2(\mathbf{h}, k)$ the auto-covariance function for a spatiotemporal point process is defined by

$$v(\mathbf{h}, k) = \lambda_2(\mathbf{h}, k) - \lambda^2. \quad (3.2.1)$$

Thus the complete covariance function is defined by

$$\lim_{|A_{i1}|, |A_{j2}| \rightarrow 0} \frac{\text{cov}[N(A_{i1}), N(A_{j2})]}{|A_{i1}| |A_{j2}|} = v(\mathbf{h}, k) + \lambda \delta(\mathbf{h}, k), \quad (3.2.2)$$

where $A_{i1} = d\mathbf{s}_{i1} \times dt_1$, $A_{j2} = d\mathbf{s}_{j2} \times dt_2$, and $\delta(\mathbf{h}, k)$ is a multivariate Dirac delta function given by

$$\delta(\mathbf{h}, k) = \begin{cases} \infty & \mathbf{h} = 0, k = 0 \\ 0 & \text{otherwise} \end{cases}.$$

Based on (3.2.2) the inverse Fourier transform of $v(\mathbf{h}, k) + \lambda \delta(\mathbf{h}, k)$ is

$$\lambda_2(\mathbf{h}, k) + \lambda \delta(\mathbf{h}, k) = \int_{-\infty}^{\infty} \int_{-\infty}^{\infty} e^{i(\boldsymbol{\omega}'\mathbf{h} + \gamma k)} G \circ F(d\boldsymbol{\omega}, d\gamma), \quad (3.2.3)$$

where $G \circ F$ represents a convolution of spectral distribution functions. The Fourier transform

of $v(\mathbf{h}, k) + \lambda\delta(\mathbf{h}, k)$ is defined by

$$\begin{aligned} g \circ f(\boldsymbol{\omega}, \gamma) &= \frac{1}{(2\pi)^3} \left\{ \int_{-\infty}^{\infty} \int_{-\infty}^{\infty} e^{-i(\boldsymbol{\omega}'\mathbf{h} + \gamma k)} [v(\mathbf{h}, k) + \lambda\delta(\mathbf{h}, k)] d\mathbf{h} dk \right\} \\ &= \frac{1}{(2\pi)^3} \left\{ \int_{-\infty}^{\infty} \int_{-\infty}^{\infty} e^{-i(\boldsymbol{\omega}'\mathbf{h} + \gamma k)} v(\mathbf{h}, k) d\mathbf{h} dk + \lambda \right\}, \end{aligned} \quad (3.2.4)$$

where $g \circ f$ represents the convolution of the spectral densities for the spatial and temporal component, respectively.

Note that if the spatial and temporal components of the process are independent of each other then (3.2.3) reduces to

$$\begin{aligned} v(\mathbf{h}, k) + \lambda\delta(\mathbf{h}, k) &= \int_{-\infty}^{\infty} \int_{-\infty}^{\infty} e^{i(\boldsymbol{\omega}'\mathbf{h} + \gamma k)} G \circ F(d\boldsymbol{\omega}, d\gamma) \\ &= \int_{-\infty}^{\infty} \int_{-\infty}^{\infty} e^{i(\boldsymbol{\omega}'\mathbf{h} + \gamma k)} G(d\boldsymbol{\omega}) F(d\gamma) \\ &= \int_{-\infty}^{\infty} e^{i\boldsymbol{\omega}'\mathbf{h}} G(d\boldsymbol{\omega}) \int_{-\infty}^{\infty} e^{i\gamma k} F(d\gamma). \end{aligned} \quad (3.2.5)$$

DEFINITION 3.7 (SEPARABLE PROCESSES)

If (3.2.5) holds we refer to the spatial and temporal components of the process as *separable*.

Spatiotemporal point processes that are separable allow for analysis of the spatial component disregarding to the temporal component or of the temporal component disregarding the spatial component. In such cases, the data can be analyzed in terms of the marginal intensities given in Section 3.1.

Estimation of the spectral density is obtained through the periodogram. From (2.2.3) the periodogram can be obtained by computing the Fourier coefficients $J(\boldsymbol{\omega}_{pq}, \gamma_r)$ where

$$J(\boldsymbol{\omega}_{pq}, \gamma_r) = \frac{1}{\sqrt{(2\pi)^3 \cdot T}} \sum_{t=1}^T \sum_{j=1}^{n_t} Z(\mathbf{s}_j, t) \exp \{i(\boldsymbol{\omega}'_{pq} \mathbf{L}^{-1} \mathbf{s}_{jt} + \gamma_r t/T)\}. \quad (3.2.6)$$

$\boldsymbol{\omega}_{pq} = [2\pi p \ 2\pi q]$ are the spatial frequencies for $p = 0, 1, 2, \dots$, $q = 0, \pm 1, \pm 2, \dots$, and $\gamma_r = 2\pi r$ are the temporal frequencies for $r = -\lfloor \frac{T-1}{2} \rfloor, \dots, \lfloor \frac{T}{2} \rfloor$. The matrix \mathbf{L} is given by (2.2.5) and is assumed to be independent of t . Furthermore, for simplicity, we also assume that p and q do not depend on t .

Factoring out the temporal index in (3.2.6) yields

$$\begin{aligned} J(\boldsymbol{\omega}_{pq}, \gamma_r) &= \frac{1}{\sqrt{T \cdot 2\pi}} \sum_{t=1}^T \exp\{i\gamma_r t/T\} \left[\frac{1}{2\pi} \sum_{j=1}^{n_t} Z(\mathbf{s}_j, t) \exp\{i\boldsymbol{\omega}'_{pq} \mathbf{L}^{-1} \mathbf{s}_{jt}\} \right] \\ &= \frac{1}{\sqrt{2\pi \cdot T}} \sum_{t=1}^T \exp\{i\gamma_r t/T\} J_t(\boldsymbol{\omega}_{pq}), \end{aligned} \quad (3.2.7)$$

where $J_t(\boldsymbol{\omega}_{pq})$ is the spatial Fourier coefficient defined by (2.2.4) at time t . The formula given by (3.2.7) suggests a computationally efficient approach using the fast Fourier transform to obtain the spatiotemporal periodogram. Furthermore, (3.2.7) represents the Fourier transform of the spatial frequencies (p, q) over time. We expect that if p or q are periodic over time, there should be a large periodogram ordinate for some temporal frequency r .

The spatiotemporal periodogram is obtained from (3.2.6) and given by

$$\begin{aligned} I(\boldsymbol{\omega}_{pq}, \gamma_r) &= J(\boldsymbol{\omega}_{pq}, \gamma_r) \bar{J}(\boldsymbol{\omega}_{pq}, \gamma_r) \\ &= \left[\frac{1}{\sqrt{2\pi \cdot T}} \sum_{u=1}^T \exp\{i\gamma_r u/T\} J_u(\boldsymbol{\omega}_{pq}) \right] \left[\frac{1}{\sqrt{2\pi \cdot T}} \sum_{t=1}^T \exp\{i\gamma_r t/T\} J_t(\boldsymbol{\omega}_{pq}) \right] \\ &= \frac{1}{2\pi \cdot T} \sum_{t=1}^T \sum_{u=1}^T \bar{J}_t(\boldsymbol{\omega}_{pq}) J_u(\boldsymbol{\omega}_{pq}) \exp\{-i\gamma_r(t-u)/T\} \\ &= \frac{1}{2\pi \cdot T} \sum_{t=1}^T \sum_{u=1}^T \bar{J}_t(\boldsymbol{\omega}_{pq}) J_u(\boldsymbol{\omega}_{pq}) \exp\{-i\gamma_r k/T\} \end{aligned} \quad (3.2.8)$$

where $k = t - u$ is the time lag.

We conjecture that the spatiotemporal periodogram, as with the temporal and spatial periodograms (1.1.5, 2.2.4), is inconsistent and requires smoothing $I(\boldsymbol{\omega}_{pq}, \gamma_r)$. Incorporating a

smoothing factor $W(\cdot)$, an estimate of the spatiotemporal spectral density is given by

$$\widehat{g \circ f}(\boldsymbol{\omega}, \gamma) = \sum_{r=-\lfloor(T-1)/2\rfloor}^{\lfloor T/2 \rfloor} \sum_p \sum_q W(\boldsymbol{\omega} - \boldsymbol{\omega}_{pq}, \gamma - \gamma_r) I(\boldsymbol{\omega}_{pq}, \gamma_r). \quad (3.2.9)$$

Alternatively, we can do some simple averaging of the ordinates.

3.2.1 Distribution of the Spatiotemporal Periodogram

THEOREM 3.5 (DISTRIBUTION OF THE SPATIOTEMPORAL PERIODOGRAM)

Let $N(ds, dt)$ be a orderly, second-order stationary spatial point process with some probability distribution F and first two moments given by (3.1.21) and (3.2.1), respectively. Furthermore let $N(ds, dt)$ have a continuous spectral density $g \circ f(\boldsymbol{\omega}, \gamma)$ defined through (3.2.2). Then, as $n \rightarrow \infty$, the periodogram given by (3.2.8) has a distribution given by

$$2 \frac{I(\boldsymbol{\omega}_{pq}, \gamma_r)}{g \circ f(\boldsymbol{\omega}, \gamma_r)} \xrightarrow{d} \chi_2^2 \quad \text{if } (\boldsymbol{\omega}_{pq}, \gamma_r) \neq \mathbf{0} \quad (3.2.10)$$

and

$$2 \frac{I(\boldsymbol{\omega}_{pq}, \gamma_r) - \lambda}{g \circ f(\boldsymbol{\omega}, \gamma_r)} \xrightarrow{d} \chi_1^2 \quad \text{if } (\boldsymbol{\omega}_{pq}, \gamma_r) = \mathbf{0}, \quad (3.2.11)$$

where \xrightarrow{d} represents convergence in distribution. Furthermore, as $n \rightarrow \infty$,

$$\text{cov}[2I(\boldsymbol{\omega}_{pq}, \gamma_r), 2I(\boldsymbol{\omega}_{p'q'}, \gamma_{r'})] \stackrel{A}{=} \begin{cases} [g \circ f(\boldsymbol{\omega}, \gamma)]^2 & \text{if } (\boldsymbol{\omega}_{pq}, \gamma_r) = (\boldsymbol{\omega}_{p'q'}, \gamma_{r'}) \\ 0 & \text{if } (\boldsymbol{\omega}_{pq}, \gamma_r) \neq (\boldsymbol{\omega}_{p'q'}, \gamma_{r'}) \end{cases},$$

where $\stackrel{A}{=}$ represents asymptotic equality.

PROOF OF THEOREM 3.5

Brillinger (1972) provides a proof of Theorem 3.5 for a point process in one-dimension. Mugglestone and Renshaw (1996b) extend the proof to two dimensions (see Theorem 2.1). We now extend these results to include a third dimension in time.

We begin by writing the spatiotemporal Fourier coefficients given by (3.2.6) as

$$J(\boldsymbol{\omega}_{pq}, \gamma_r) = a_{pqr} + ib_{pqr},$$

where $a(p, q, r)$ is the real part and b_{pqr} is the imaginary part of J . Then, according to Brillinger (1972), as $n \rightarrow \infty$,

$$\begin{aligned} a_{pqr} &\xrightarrow{d} N(0, g \circ f(\boldsymbol{\omega}, \gamma)/2) \\ b_{pqr} &\xrightarrow{d} N(0, g \circ f(\boldsymbol{\omega}, \gamma)/2) \end{aligned} \quad (3.2.12)$$

for $(\boldsymbol{\omega}, \gamma) \neq \mathbf{0}$. For the case when $(\boldsymbol{\omega}, \gamma) = \mathbf{0}$, as $n \rightarrow \infty$, we have

$$a_{000} \xrightarrow{d} N(\lambda, g \circ f(\mathbf{0}, 0)/2)$$

and the imaginary part $b_{pqr} \equiv 0$. We also have a_{pqr} , b_{pqr} and $a_{p'q'r'}$, $b_{p'q'r'}$ are asymptotically independent for $p \neq p'$, $q \neq q'$, and/or $r \neq r'$.

Construction of the periodogram is given by

$$I(\boldsymbol{\omega}_{pq}, \gamma_r) = J(\boldsymbol{\omega}_{pq}, \gamma_r) \bar{J}(\boldsymbol{\omega}_{pq}, \gamma_r) = a_{pqr}^2 + b_{pqr}^2.$$

Because the estimates of a_{pqr} and b_{pqr} are asymptotically independent Gaussian, the periodogram ordinates have asymptotic distribution

$$2 \frac{I(\boldsymbol{\omega}_{pq}, \gamma_r)}{g \circ f(\boldsymbol{\omega}, \gamma)} \xrightarrow{d} \chi_2^2 \quad \text{for } (\boldsymbol{\omega}, \gamma) \neq \mathbf{0}$$

and

$$2 \frac{I(\mathbf{0}, 0) - \lambda}{g \circ f(\mathbf{0}, 0)} \xrightarrow{d} \chi_1^2.$$

Q.E.D.

COROLLARY 3.5 (DISTRIBUTION OF THE CSTR PERIODOGRAM)

If $N(ds, dt)$ is a CSTR point pattern then as $n \rightarrow \infty$,

$$(2\pi)^3 E[I(\boldsymbol{\omega}_{pq}, \gamma_r)] \stackrel{A}{=} \begin{cases} 3\lambda/2 & \text{for } (\boldsymbol{\omega}_{pq}, \gamma_r) = \mathbf{0} \\ \lambda & \text{for } (\boldsymbol{\omega}_{pq}, \gamma_r) \neq \mathbf{0} \end{cases}$$

and

$$(2\pi)^6 \text{var}[I(\boldsymbol{\omega}_{pq}, \gamma_r)] \stackrel{A}{=} \begin{cases} \lambda^2/2 & \text{for } (\boldsymbol{\omega}_{pq}, \gamma_r) = \mathbf{0} \\ \lambda^2 & \text{for } (\boldsymbol{\omega}_{pq}, \gamma_r) \neq \mathbf{0} \end{cases}.$$

PROOF OF COROLLARY 3.5

If we assume the observed events are distributed as Poisson with intensity λ then $\lambda(\mathbf{s}, t) = \lambda$ and $\lambda_2(\mathbf{h}, k) = \lambda^2$. Thus the complete covariance density given by (3.2.1) is

$$v(\mathbf{h}, k) + \lambda\delta(\mathbf{h}, k) = \underbrace{\lambda_2(\mathbf{h}, k)}_{=\lambda^2} - \lambda^2 + \lambda\delta(\mathbf{h}, k) = \lambda\delta(\mathbf{h}, k).$$

This implies the covariance between two events a distance $\mathbf{h} \neq \mathbf{0}$ and time lag $k \neq 0$ apart is 0. This reduces the spectral density to

$$g \circ f(\boldsymbol{\omega}, \gamma) = \frac{1}{(2\pi)^3} \left[\int_{-\infty}^{\infty} \int_{-\infty}^{\infty} \underbrace{[\lambda_2(\mathbf{h}, k) - \lambda^2]}_{=0} e^{-i(\boldsymbol{\omega}'\mathbf{h} + \gamma k)} d\mathbf{h} dk + \lambda \right] \equiv \frac{\lambda}{(2\pi)^3}.$$

Therefore from Theorem 3.5, for $(\boldsymbol{\omega}_{pq}, \gamma_r) \neq \mathbf{0}$, we have

$$E[I(\boldsymbol{\omega}_{pq}, \gamma_r)] \stackrel{A}{=} \frac{1}{2} [g \circ f(\boldsymbol{\omega}, \gamma)] \cdot E[\chi_2^2] = \frac{1}{2} \frac{\lambda}{(2\pi)^3} \cdot 2 = \frac{\lambda}{(2\pi)^3}$$

and

$$\text{var}[I(\boldsymbol{\omega}_{pq}, \gamma_r)] \stackrel{A}{=} \frac{1}{4} [g \circ f(\boldsymbol{\omega}, \gamma)]^2 \cdot \text{var}[\chi_2^2] = \frac{1}{4} \left[\frac{\lambda}{(2\pi)^3} \right]^2 \cdot 4 = \left[\frac{\lambda}{(2\pi)^3} \right]^2.$$

Q.E.D.

As with the spatial periodogram, we can use Corollary 3.5 to test our spatiotemporal point

pattern for CSTR. Specifically, for an α -level test we would reject the hypothesis that at spatiotemporal point pattern is CSTR if

$$2 \frac{I(\boldsymbol{\omega}_{pq}, \gamma_r)}{\widehat{\lambda}/(2\pi)^3} \notin (\chi_{2,\alpha/2}^2, \chi_{2,1-\alpha/2}^2) \quad \text{for } (pqr) \neq \mathbf{0},$$

where $\widehat{\lambda} = n/T$ is the basic intensity estimator given by (3.1.39) for analysis on the unit square ($|A| = 1$).

3.2.2 Polar Representation of the Spatiotemporal Periodogram

No direct graphical representation of the spatiotemporal periodogram can be given as it would be a plot in four dimensions: $\{p, q, r, I(\boldsymbol{\omega}_{pq}, \gamma_r)\}$. The R - and Θ -spectra given by (2.2.13) and (2.2.14), respectively, can also be extended to the spatiotemporal case for interpretability. Converting the spatial frequencies in (3.2.7) from rectangular ($\boldsymbol{\omega}_{pq}$) to polar coordinates ($\boldsymbol{\omega}_{\rho\theta}$) we define the R_γ -spectrum at temporal frequency γ_r as

$$f_R(\rho, \gamma_r) = n_\rho^{-1} \sum_{\rho'} \sum_{\theta} P(\boldsymbol{\omega}_{\rho'\theta}, \gamma_r) \quad \rho = 1, 2, \dots, \quad (3.2.13)$$

where n_ρ are the number of spatial periodogram ordinates in the summation, $P(\boldsymbol{\omega}_{\rho\theta}, \gamma_r) \equiv I(\boldsymbol{\omega}_{pq}, \gamma_r)$, and $\rho - 1 < \rho' \leq \rho$. Similarly, the Θ_γ -spectrum at temporal frequency γ_r is defined by

$$f_\Theta(\theta, \gamma_r) = n_\theta^{-1} \sum_{\rho} \sum_{\theta'} P(\boldsymbol{\omega}_{\rho\theta'}, \gamma_r) \quad \theta = -85^\circ, -80^\circ, \dots, 85^\circ \quad (3.2.14)$$

where n_θ are the number of spatial periodogram ordinates in the summation and $\theta - 5^\circ < \theta' \leq \theta + 5^\circ$. From Theorem 3.5, the periodogram ordinates are asymptotically independent and converge to scaled χ_2^2 distributions (for $(\boldsymbol{\omega}, \gamma) \neq \mathbf{0}$). Therefore, the asymptotic behavior of the R_γ - and Θ_γ -spectra ordinates will also be scaled χ^2 distributions with $2n_\rho$ and $2n_\theta$ degrees of freedom, respectively. The latter construction would render two three-dimensional

plots. Extending the test for CSTR from Corollary 3.5 to the R_γ - and Θ_γ -spectra, we have an α -level test where the point process deviates from CSTR if

$$\frac{(2n_\rho)f_R(\rho, \gamma_r)}{\widehat{\lambda}/(2\pi)^3} \notin \left(\chi_{2n_\rho, \alpha/2}^2, \chi_{2n_\rho, 1-\alpha/2}^2 \right)$$

or

$$\frac{(2n_\theta)f_\Theta(\theta, \gamma_r)}{\widehat{\lambda}/(2\pi)^3} \notin \left(\chi_{2n_\theta, \alpha/2}^2, \chi_{2n_\theta, 1-\alpha/2}^2 \right).$$

Though we have not proposed any parametric models for spatiotemporal point processes, inference can still be obtained using the polar spectra.

Inference based on the Temporal Polar spectra

From the decomposition of the spatiotemporal Fourier coefficients in (3.2.7), we see that temporal periodicities of spatial frequencies are determined through periodogram analysis. Conversion of the spatiotemporal periodogram into polar coordinates does not change this relationship. Specifically, to determine whether clustering is periodic over time we would examine $f_R(\rho, \gamma)$ for different values of ρ . If $f_R(\rho, \gamma)$ is large for temporal frequency γ , then the periodicity of the clustering radius ρ is $\gamma/(2\pi|T|)$. Similarly, if orientation is periodic over time we would examine $f_\Theta(\theta, \gamma)$ for different values of θ . If $f_\Theta(\theta, \gamma)$ is large for temporal frequency γ , then the periodicity of the orientation θ is $\gamma/(2\pi|T|)$.

Chapter 4

Simulation and Case Study

This chapter brings together much of the methodology described in the previous two chapters. We will describe methods of simulating spatial and spatiotemporal point processes. The simulations will provide supporting evidence for the Theorems presented in this dissertation. Specifically, we will show the properties of CSR, aggregated, and regular point processes in the spatial domain as well as in the frequency domain.

The case study to which we apply the methods is that of the bird data introduced in Chapter 1. We will first study the data ignoring its temporal component. The point pattern will be analyzed using the K -function as well as the periodogram analysis discussed in Chapter 2. Both analyses will compare the observed point pattern to the CSR model.

The spatiotemporal methods from Chapter 3 will also be applied in this chapter. Algorithms for simulating CSTR patterns from the four types of spatiotemporal point patterns introduced in Chapter 1 will be included. The spatiotemporal K -function analysis will be applied to the latter simulation results along with the simulated envelopes to test observed patterns for CSTR. The spatiotemporal periodogram analysis from Chapter 3 will also be demonstrated to analyze the sampled point patterns in time simulations.

Finally, the woodpecker data will conclude the discussion. The temporal component will be

reintroduced and the analyses will be based on the spatiotemporal intensity and periodogram estimation discussed in Chapter 3.

4.1 Simulated and Real Spatial Point Patterns

4.1.1 Simulations

The simulated point patterns in this section are those shown in Figure 1.3.2. \widehat{L} -analysis is shown in Figure 2.1.3a-c (p. 28) . Periodogram analysis is shown in Figure 2.2.3a-c (p. 39). The observed patterns were generated with the S-Plus function `make.pattern` [Kaluzny et al. 1998].

```

CSR:    make.pattern(n=n,process="binomial")
Regular: make.pattern(n=n,process="SSI",radius=0.05)
Aggregated: make.pattern(n=n,process="cluster",radius=0.075,cpar=15)

```

Table 4.1: `make.pattern` calls for generating simulated data ($n = 200$).

The size of the point patterns was fixed for $n = 200$. This number was chosen to adequately fill the region of interest. Other parameters, such as the radius of inhibition for the regular process and the parent rate parameter (`cpar`) for the aggregated process, were chosen arbitrarily.

The \widehat{L} -analyses in Section 2.1.3 are shown with simulated envelopes to provide evidence whether the spatial point pattern is CSR. Other hypotheses can be constructed from simulated envelopes by generating other, non-CSR patterns with user-defined parameters. However, the Cramér-von Mises statistic becomes more complicated and is not as reliable as that of the CSR hypothesis [Diggle, 1983]. Simulations for K -function analysis are excluded from this dissertation due to the large amounts of literature on the subject [cf. Diggle (1983), Ripley (1988), Cressie (1993)].

As expected, the \widehat{L} -analysis and the periodogram analysis agree for these simulated data sets

since all events were generated with isotropic covariance functions. In particular, we notice that the plots of $\widehat{L}(h)$ for each of the patterns have qualitative similarities to their analogous R -spectrum. This should always be true, regardless of whether anisotropy is present or not. For the clustered process, the $\widehat{L}(h)$ has two peaks corresponding to first the clustering radius of the children to the parents and then the clustering radius of the parents to each other. This phenomenon is also apparent in the R -spectrum with significant peaks at $\rho \leq 6$ corresponding to clustering radii of 0.375 units. Though the R -spectrum ordinate is significant for $\rho = 2$ when the pattern is compared to CSR, it reveals that there are two clustering radii to diagnose: the radius of child to parent and the radius of parent to parent. For the inhibition and CSR process, similar comparisons between the two analyses can also be made.

As noted in Chapter 2, the main advantage of periodogram analysis over the K -function analysis is that the former does not require simulated inference. Theorem 2.1 shows that the distribution of the periodogram is asymptotically χ^2 scaled by the spectral density. Figure 4.1 demonstrates Theorem 2.1 (or more specifically Corollary 2.1) when the point pattern is CSR. Two-hundred point patterns each with $n = 200$ were generated. For each point pattern, the spatial periodogram was constructed for frequencies $p = 0, \dots, 16$ and $q = -15, \dots, 16$. The periodogram ordinates were then averaged over the 200 simulations to obtain the simulated spatial periodogram (lower left). As proven in the corollary, the averaged ordinates for all p and q are close to one when the pattern is CSR. Similar results are seen in the polar spectra (upper right and left).

The ratio plot for the Θ -spectra (lower right) suggests a possible bias incurred. Theoretically, the ratio of two independent χ^2 distributions divided by their degrees of freedom is an F distribution. The plot reveals that the ratio of the Θ -spectra ordinates is below the theoretical mean of an F . This may be an artifact of the simulation in that the ordinates are determined from the ratio of the means rather than from the mean of ratio of two χ^2 . Other possible factors for the bias may include choice of n since all distributional results are asymptotic.

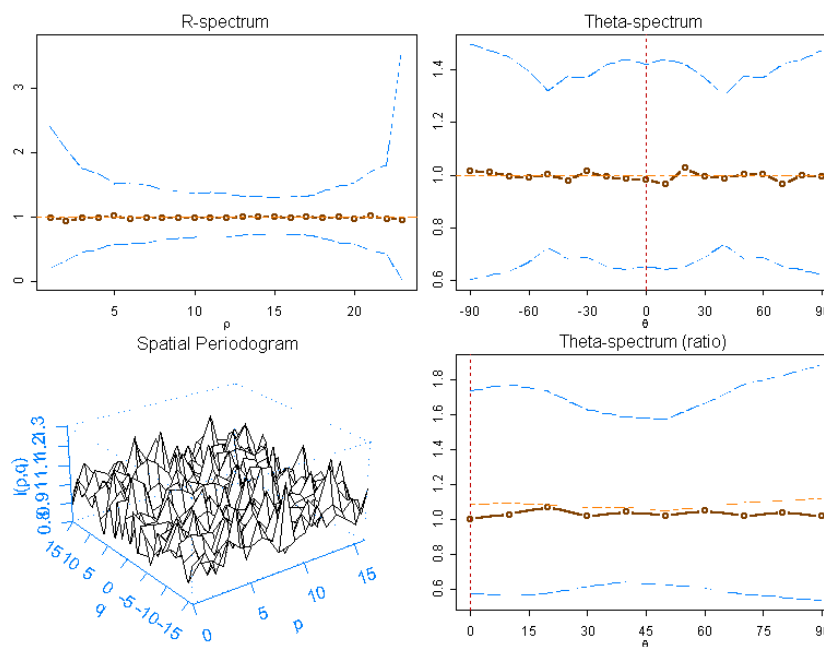


Figure 4.1: Spatial periodogram and polar spectra for simulated CSR point patterns. 200 simulated point patterns with $n = 200$ were generated under CSR. Under CSR, the periodogram ordinates are asymptotically independent scaled- χ_2^2 random variables (See Corollary 2.1). The horizontal dashed-lines for the polar spectra represent the theoretical expected value and 95% confidence limits of the polar spectra under CSR.

4.1.2 Woodpecker Data

The spatial analysis of the woodpecker data is also given in Chapter 2. Both the \widehat{L} -analysis (Figure 2.1.3d, p. 28) and the periodogram analysis (Figure 2.2.3d, p. 39) revealed the FB002 family of woodpeckers to be highly clustered. When compared to CSR patterns, both analyses strongly rejected the independence hypothesis.

One benefit of periodogram analysis, and specifically, the polar spectra, is that estimation of the clustering radius and the angle of orientation is possible. As discussed in Section 2.2.3, the large ordinates in the R -spectrum for $\rho < 5$ suggests a clustering radius of $5/16$ (scaled) units. The original events were obtained on a bounding box of 4706×4706 feet, thus the estimated clustering radius becomes $(5/16) \cdot 4706 = 1471$ feet or about 0.28 miles. This is

interpreted as a high frequency of events within 1471 feet from any arbitrary event in the sample. Specifically, if a woodpecker is observed at location \mathbf{s} , there is a high likelihood that the same woodpecker will be observed again within 1471 feet.

Furthermore, an angle of orientation is apparent from the Θ -spectrum. The largest ordinate is observed for $\theta = -60^\circ$. Thus, if a woodpecker is observed at location \mathbf{s} , there is a high likelihood of observing the same woodpecker again in a southeasterly direction. The possible anisotropy can be seen in the intensity estimate (Figure 2.2.3d, p. 39). The biological significance for the observed anisotropy is unknown at this time.

Figure 4.2 shows how the analysis is applied to the actual data. Each concentric circle corresponds to a value of ρ in the R -spectrum. The arrow shows the orientation obtained from the Θ -spectrum.

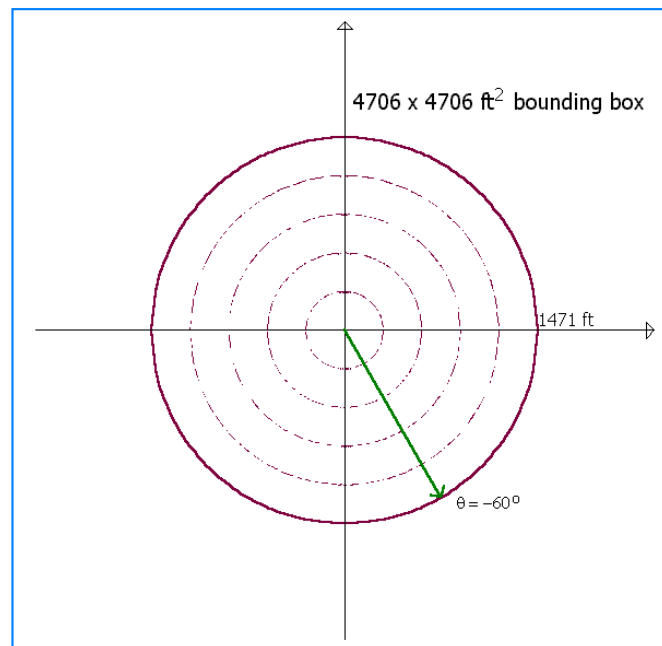


Figure 4.2: Clustering radius and angle of rotation for FB002 family. From Figure 2.2.3d we see a clustering radius of $\rho < 5$, which translates into 1471 feet, and an orientation of $\theta = -60^\circ$.

4.2 Simulated and Real Spatiotemporal Point Patterns

This section will demonstrate the theory developed in Chapter 3 for analysis of spatiotemporal point patterns. The only parametric model considered in the simulations is that of CSTR due to the lack of explicitly defined parametric spatiotemporal point processes.

4.2.1 Simulating Spatiotemporal Point Patterns

Before a discussion of the methodology for analyzing spatiotemporal point patterns can be given, an outline for simulating data sets must be provided. The four types of spatiotemporal point patterns introduced in Chapter 1 are: the Earthquake Process, the Explosion Process, the Birth-Death Process, and Point Patterns Sampled in Time.

Of the four processes, the first three allow for a stochastic temporal component. For this reason, the process we are attempting to generate may be affected by whether we generate the spatial and temporal events marginally or jointly. However, as stated above, we are only considering simulation of the CSTR model for which the spatial and temporal components are independent. Thus, the algorithms described below for these processes will generate spatial events followed by temporal events. Although, when the temporal component is not stochastic, the algorithms simply generate spatial point patterns at regularly spaced intervals.

1. EARTHQUAKE PROCESS:

For fixed n the CSTR earthquake process is considered to be a Uniform process in space and time, therefore generating an earthquake process will rely on much of this theory. We will consider the case where the sample size n is fixed. Therefore the spatial point pattern obtained is Uniform on the region A . Simulating a CSTR earthquake process with n events is demonstrated in the following algorithm:

ALGORITHM I

- i. Generate n ordered pairs from a two-dimensional Uniform distribution in some region A .
- ii. Generate n events from a Uniform distribution on the interval $(0, T)$.
- iii. Create the triplet (s_x, s_y, t) where (s_x, s_y) is obtained from Step i and t is obtained from Step ii.
- iv. Sort the n triplets in ascending order by the value t .

2. EXPLOSION PROCESS:

The CSTR Explosion process is obtained in a similar fashion to that of the Earthquake process except at every time t , a sample size of n_t events is generated. Again, the underlying spatial distribution will be Uniform on A for all time t as well as Uniform on $(0, T)$. Simulating a CSTR explosion process with $\sum_t n_t$ events is demonstrated in the following algorithm:

ALGORITHM II

- i. Generate n_t ordered pairs from a two-dimensional Uniform distribution in some region A .
- ii. Repeat Step i t times.
- iii. Generate t events from a Uniform distribution on the interval $(0, T)$.
- iv. Create the triplet (s_{xt}, s_{yt}, t) where (s_{xt}, s_{yt}) is obtained from Step i and t is obtained from Step iii.
- v. Sort the $\sum_t n_t$ events in Step iv in ascending order by the value t .

3. BIRTH-DEATH PROCESS:

The CSTR Birth-Death process has an inherent temporal component related to the life time of each observed event. If we are to treat the birth-death process as a spatiotemporal point pattern in the context of this dissertation, we will ignore the survival time. Instead the birth-death process can be thought of an explosion process if sampling

intervals are random or as a sampled point pattern in time if the sampling intervals are fixed. For this reason, we defer the simulation of birth-death processes to either Algorithm II or Algorithm III.

4. SAMPLED POINT PATTERNS IN TIME:

Since Sampled Point Patterns in Time treat time as fixed, this is perhaps the simplest pattern to simulate. Algorithm III outlines the simulation of a sampled point pattern in time:

ALGORITHM III

- i. Define $t = 0, 1, 2, \dots, T$.
- ii. For every time t , generate n_t ordered pairs from a two-dimensional Uniform distribution in some region A .

4.2.2 Spatiotemporal K -analysis Simulation

The spatiotemporal K -functions have limited use until non-CSTR spatiotemporal point patterns have been parametrically defined. Furthermore, large amounts of data are required to use $K_I(h, k)$ so that temporal “white-space” is negligible. The CSTR point pattern studied in this section utilizes $K_{II}(h, k)$.

The simulation generates a CSTR pattern according to Algorithm III. Each point pattern in the simulation consists of eight time periods with 100 observations uniformly distributed over the unit square. A simulated envelope is constructed by generating 100 CSTR patterns with the same parameters and computing $\widehat{K}_{II}(h, k)$. As suggested in Section 3.1.5, the observed \widehat{K} -function and the simulated \widehat{K} -functions were transformed to the spatiotemporal \widehat{L} -function. Figure 4.3 shows the results of the simulation.

The simulated envelope in Figure 4.3 reveals the bias incurred for large distances h . This is expected under the construction of the spatiotemporal K -function in Section 3.1.5. Under

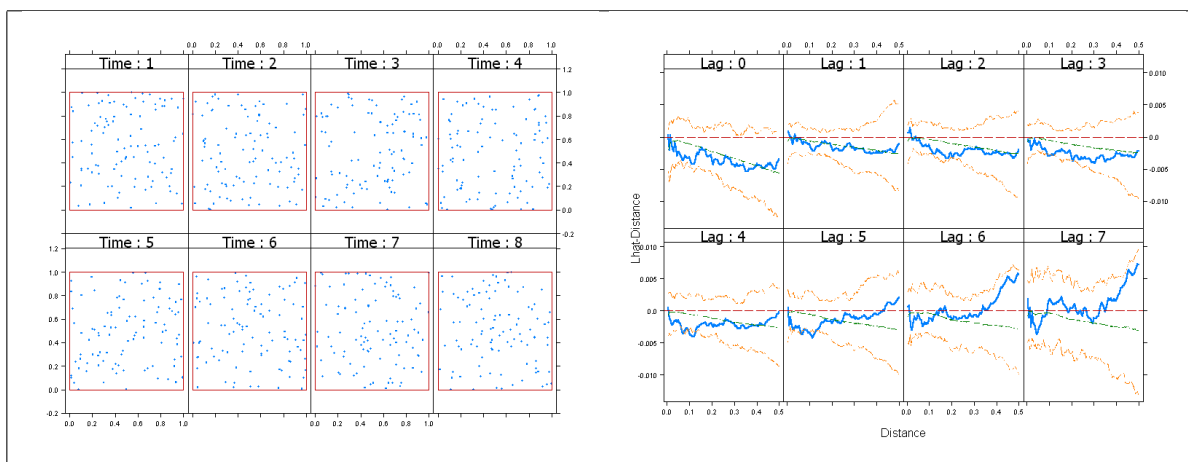


Figure 4.3: Results of simulated \widehat{L}_{II} -functions. Left plot is the simulated CSTR pattern. Right plot is observed \widehat{L}_{II} with simulated envelope. The envelope is based on 100 CSTR point patterns with the same parameters as the observed pattern.

the hypothesis of CSTR the spatiotemporal L -function should be h . Clearly, for all lags k , the spatiotemporal L -function minus h becomes more negative as h increases. However, the simulated envelope still allows us to conclude the observed process is CSTR.

4.2.3 Spatiotemporal Periodogram Simulations

As noted in Chapter 3, the spatiotemporal periodogram analysis in this dissertation considers only spatial point patterns regularly spaced in time. However, analysis of other types of spatiotemporal point patterns in the frequency domain is straightforward by replacing integer time with continuous time. Alternatively, as in the case of the earthquake process for which data are sparse, the point pattern can be discretized in space and/or time with subsequent analyses performed on the aggregated data.

For the purposes of the simulation, 200 CSTR processes were obtained using the Algorithm III with the intent of verifying the results from Corollary 3.5. Each point pattern in the simulation consists of eight time periods with 100 observations uniformly distributed over the unit square. The spatiotemporal periodogram as well as the polar spectra were then constructed for each pattern and averaged over the entire simulation. Since there are eight

time periods then the temporal frequencies are $\gamma_r = 2\pi r$ for $r = -3, -2, \dots, 3, 4$. Plots of the polar spectra obtained from the simulation are shown in Figure 4.4. As proven in the theorem, the ordinates for all frequencies are close to essentially one under CSTR.

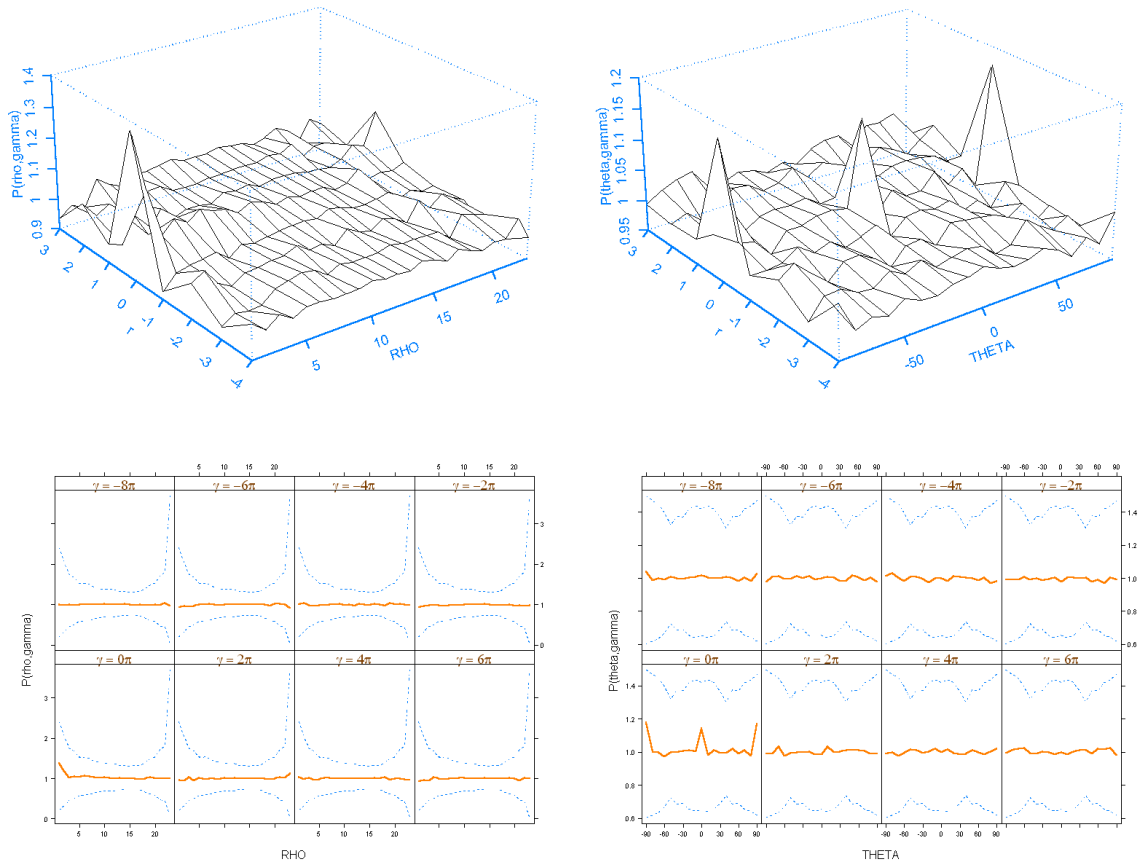


Figure 4.4: Simulation to demonstrate the distributional properties of the spatiotemporal periodogram under CSTR. 200 CSTR point patterns with $n = 100$ were generated according to Algorithm III. The left and right plots are the R_γ - and Θ_γ -spectra, respectively, averaged over the 200 point patterns. The upper plots are R_γ and Θ_γ , while the lower plots are cross-sectional plots of the upper plots for different values of γ . The dashed lines on the lower plots are 95% confidence bounds from a scaled- χ^2 based on the CSTR model (see Corollary 3.5).

The deviation of the R_γ -spectrum for $\rho = 1$ also reveals a bias for frequencies close to zero. This is a known problem that is usually overcome by smoothing of the periodogram [Bartlett, 1964]. Even though the polar spectra provide some smoothing by averaging neigh-

boring ordinates, the R_γ -spectrum suffers for small ρ since only few ordinates are close to the zero frequency.

4.2.4 Woodpecker Data

We now complete the analysis of the woodpecker data by incorporating the temporal component. Figure 4.5a shows the locations, a kernel intensity estimate, and the 95% homorange contour of FB002 from December 1994 (9412) to October 1996 (9610). Data for six of the months were not collected for unknown reasons. The estimates of intensity are for $\lambda(\mathbf{s}|t)$ and thus incorporate time in a conditional sense. Figure 4.5b incorporates the temporal component using the kernel estimator given by (3.1.41, p. 71). The six missing months are estimated by interpolation.

The 95% homorange contours are also estimated using the method from Worton (1989). Specifically, for each time period a kernel estimate of intensity is obtained. Then, a plane is placed over the region such that approximately 95% of the intensity volume is above the plane. The contour is obtained from where the plane intersects the intensity estimate and the 95% homorange is computed by calculating the area of the contour. As with the intensity estimate, the calculation of the homorange is highly dependent on the bandwidth of the kernel estimator as well the number locations \mathbf{s} at which the intensity is estimated.

The temporal dimension, which is measured in months, was scaled to unit length with zero being the first month and one being the last month. Figure 4.5a is an estimate of the spatial intensity at each month using the Epanechnikov kernel with bandwidth $b = 0.15$ which corresponds to about 705.9 feet. Figure 4.5b is an estimate of spatiotemporal intensity using the Epanechnikov kernel with bandwidths $b_s = 0.15$ and $b_t = 0.15$ which correspond to about 705.9 feet spatially and 3.45 months temporally.

Figure 4.6 shows the area within the 95% homorange contours shown in Figure 4.5 over the 23 month period. The bottom line is the homorange estimate based on $\hat{\lambda}(\mathbf{s}|t)$. The top line

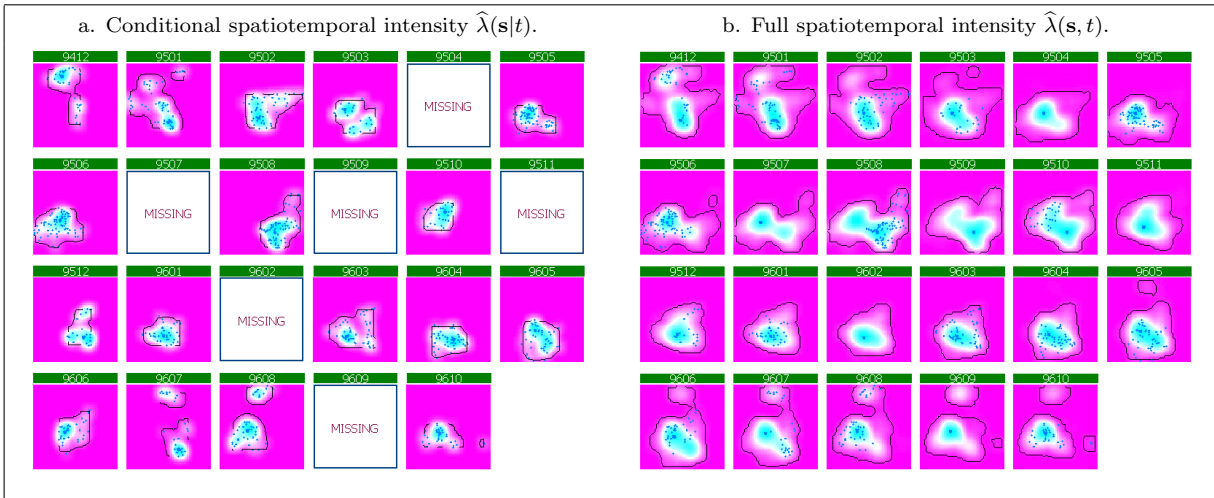


Figure 4.5: Kernel estimates of intensity for cluster FB002 with 95% homerange contour from December 1994 (9412) to October 1996 (9610). Figure (a) is the spatial kernel estimates at each month, $\hat{\lambda}(s|t)$. Figure (b) uses the spatiotemporal kernel estimate, $\hat{\lambda}(s, t)$. The data were scaled both spatially and temporally to unit length for simplicity. The spatial bandwidth for each estimate is $b_s = 0.15$ which corresponds to about 705.9 feet. The temporal bandwidth for the spatiotemporal estimate is $b_t = 0.15$ which corresponds to about 3.45 months. The Epanechnikov kernel was used for both estimates.

is the homerange estimate based on $\hat{\lambda}(s, t)$. As expected, the areas based on the spatiotemporal intensity are greater because the temporal averages are included in the smoothing. Furthermore, both a periodicity and a downward trend in homerange area is apparent from the spatiotemporal intensity which is overlooked by the conditional intensity. The downward trend is may be the reason for the red-cockaded woodpeckers listing as a federally endangered species. The reduction in homerange due to either human or environmental factors may be causing the population to decline. Because of the woodpecker's peculiar habitation (see Section 1.5), deforestation due to human encroachment is one possible reason for the homerange decreasing [Walters et al., 1998].

One must note that this analysis of the spatiotemporal intensity may be an artifact of the smoothing technique and should be analyzed with caution. As with density estimation, intensity estimates rely heavily on bandwidth selection. Since no automatic bandwidth selection was used to obtain the intensities, inference based on these results is limited.

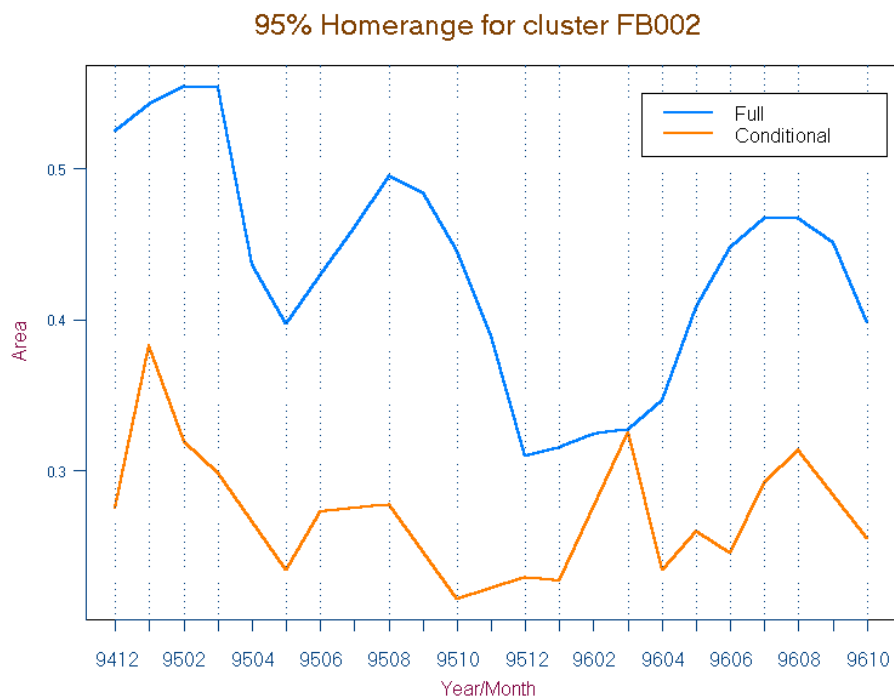


Figure 4.6: Time series of 95% homorange areas for cluster FB002 based on $\hat{\lambda}(\mathbf{s}|t)$ and $\hat{\lambda}(\mathbf{s}, t)$. The lower curve is the homorange areas based on $\hat{\lambda}(\mathbf{s}|t)$ shown in Figure 4.5a. The upper curve is the homorange areas based on $\hat{\lambda}(\mathbf{s}, t)$ shown in Figure 4.5b.

The periodicity of the homorange can be explored by the spatiotemporal periodogram defined by (3.2.8). Spatial frequencies are computed from $p = 0, \dots, 16$ and $q = -15, \dots, 16$ as recommended by Renshaw and Ford (1983). Temporal frequencies are computed for $r = -11, \dots, 11$ for the 23 months. Missing months are removed by setting $J(\omega_{pqt}) = 0$ if $t \notin T$. The latter construction of the periodogram is a valid estimate of the spatiotemporal spectral density though it introduces bias [Dunsmuir and Robinson, 1983].

The spatiotemporal periodogram is converted to polar coordinates for interpretation. Figures 4.8 and 4.9 show the Θ_γ - and R_γ -spectra for $\gamma_r = 2\pi r$. The confidence bands on each plot are based on the 95% quantiles from a scaled χ^2 distribution (see Section 3.2.2). The Θ_γ -spectrum in Figure 4.8 reveals no apparent periodic anisotropy. However, the R_γ -spectrum in Figure 4.9 reveals an expected behavior exhibited by the birds. Figure 4.7 provides a

better view of the R_γ -spectrum by extracting the ordinates corresponding to $\rho = 2$.

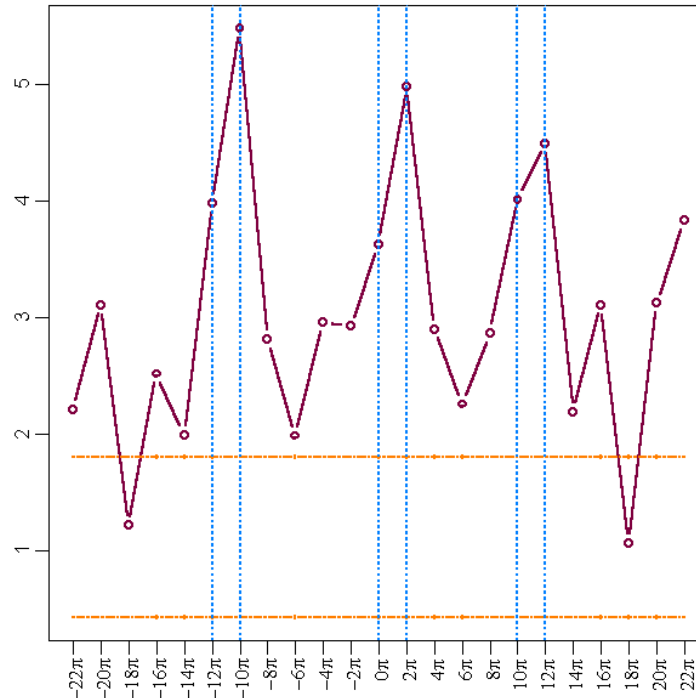


Figure 4.7: R_γ -spectrum for $\rho = 2$ for the woodpecker data. The horizontal lines are the 95% confidence bands based on a scaled- χ^2 distribution (see Corollary 3.5). The vertical lines are references for $\gamma = -12\pi, -10\pi, 0, 2\pi, 10\pi, 12\pi$. The clustering radius for $\rho = 2$ corresponds to 588 feet and appears to have a seasonal periodicity of approximately 6 months.

Because the spatiotemporal point pattern was observed over monthly intervals, the temporal frequencies correspond roughly to 4-5 week dependencies. Therefore, a large periodogram ordinate at $\gamma_r = 2\pi r$ represents a temporal periodicity of $r/23$ months. We further see that the clustering radius is periodic. Specifically, for $\rho = 2$ (or clustering radius of 588 feet), the R -spectrum in Figure 4.9 exhibits large ordinates at temporal frequencies $\gamma_{-5}, \gamma_{-6}, \gamma_1, \gamma_5,$ and γ_6 . A cross-section of the R_γ -spectrum for $\rho = 2$ is shown in 4.7 and is revealing. The large ordinates at frequencies $\gamma_1, \gamma_5,$ and γ_{-5} suggest a monthly autoregressive nature of the birds' clustering. The large ordinates at frequencies γ_{-6} and γ_6 suggest a 6-month seasonal clustering periodicity. Thus we can conclude that the woodpecker's clustering radius over the year is approximately 588 feet and is periodic with period 6 months. Specifically,

if a woodpecker is observed at location \mathbf{s} and month t , then there is a high likelihood of observing the same woodpecker within 588 feet of \mathbf{s} this month (γ_0), next month ($\gamma_{-5}, \gamma_1, \gamma_5$), and approximately 6 months (γ_{-6}, γ_6) from t . The biological significance of this analysis is unknown, though some explanation can be attributed to the woodpecker's yearly mating season.

The second-order analysis given by the spatiotemporal periodogram reveals the clustering periodicity, but at the cost of assuming second-order stationarity. As defined in Section 3.1.3, the latter assumption requires the spatiotemporal intensity be constant regardless of location and time. However, as noted in the analysis of the spatiotemporal kernel intensity estimates (Figure 4.6), a downward trend in the homerange estimates is present. Unfortunately, the spatiotemporal periodogram analysis does not allow us to explore this phenomenon. Periodogram analysis for nonstationary spatiotemporal point patterns will be left for future research.

The spatiotemporal K -analysis is invalid since we determined the point pattern exhibits anisotropy. Note that even though we concluded the anisotropy is not periodic, its presence is still revealed by Figure 2.2.3d. The K -function is limited to processes which are spatially isotropic, which we clearly do not have here.

4.2.5 Remarks

Until now no methods have been proposed for analyzing spatial point patterns sampled in time such as the woodpecker data. In this dissertation, we have presented sound methods of capturing the first- and second-order properties of stationary spatiotemporal point processes. Furthermore, the techniques we have laid out do not require specification of a parametric model. Through the kernel estimate of intensity we are able to gather information of the process intensity as it changes over time; and through the spatiotemporal periodogram, we capture the properties of the covariance function.

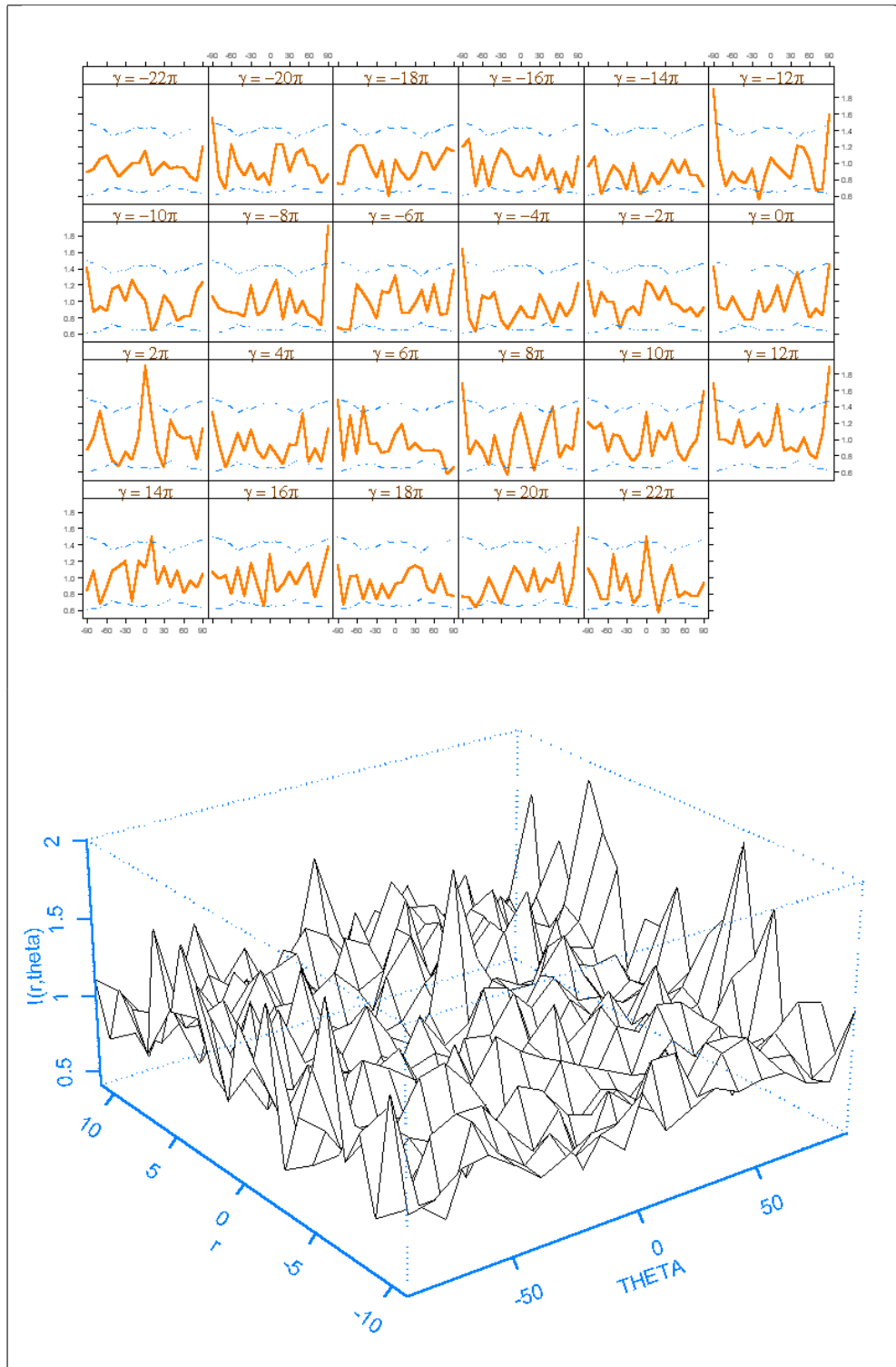


Figure 4.8: Θ_γ -spectrum obtained from $I(\omega_{pq}, \gamma_r)$ for the woodpecker data.

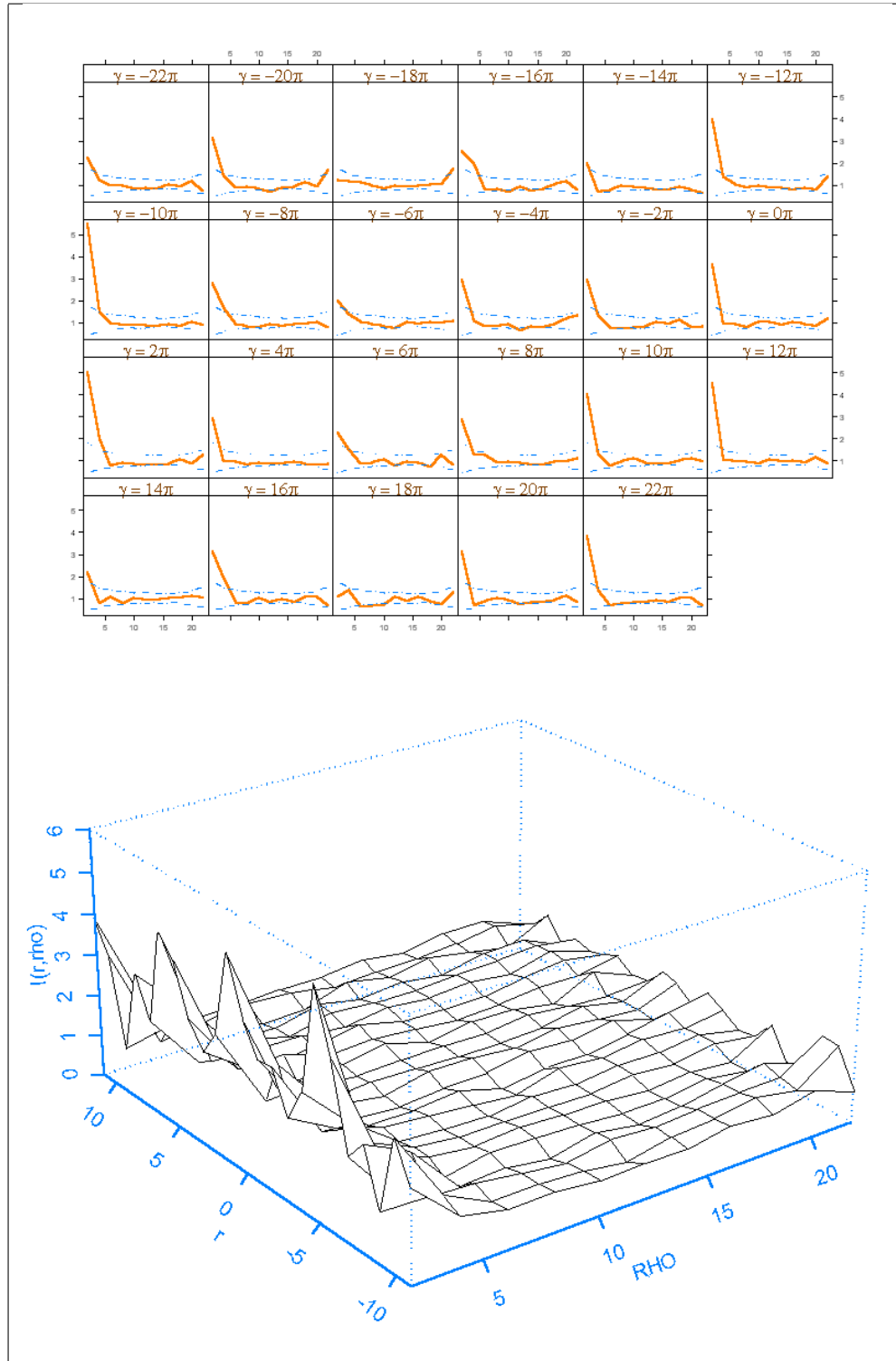


Figure 4.9: R -spectrum obtained from $I(\omega_{pq}, \gamma_r)$ for the woodpecker data. See Figure 4.7 for a cross-section of $\rho = 2$.

Chapter 5

Conclusion and Discussion

Statistics for spatial data is a rapidly growing field. Only recently has more methodology for analyzing spatial dependencies been proposed in the literature; and on a smaller scale, methods for analyzing spatiotemporal dependencies are emerging. However, there is more to be done.

In this dissertation we began by examining the current methodology for analyzing spatial point patterns. We explored the previous research in this area, found room for improvement, and pointed out where future research is required. Then, using the framework of the spatial point process, explicitly defined the spatiotemporal point process and associated first- and second-order intensity measures and further presented useful methods for analyzing different types of spatiotemporal point processes. However, at the same time as answering our original questions on how to analyze spatiotemporal point patterns, we have created new and open questions in this field.

In this chapter, I recall the work originally proposed and expound on the work accomplished. I will further summarize what has been learned about spatiotemporal point processes from my research in this area. Finally, I will close by presenting questions that were raised as a result of this research.

5.1 Proposed Work

In this dissertation, new tests for analyzing spatial point patterns were proposed. Although Renshaw and Ford (1983) first proposed the polar spectra for analyzing spatial point patterns, their subsequent use for constructing and testing hypotheses was neglected. The ratio test for anisotropy defined in Chapter 2 elaborates on the Θ -spectrum for clearly identifying the angle of rotation.

Though not originally proposed, we also explored the effects of geometric anisotropy on the spatial periodogram. I did not make any definitive conclusion on how rotating and scaling a spatial point pattern can be realized through direct examination of the Θ -spectrum. However, I have discovered some relationship that will require further research in this area.

Also considered were new methods for analyzing spatiotemporal point patterns. Through direct extensions of spatial point patterns analysis, tools were developed to study the first- and second-order properties of a spatiotemporal point process. Definitions of full, marginal, and conditional intensity measures led to an explicit definition of weak stationarity in space and/or time. Then, based on these definitions, I provided theorems and corollaries that related our first-order intensity measures under certain conditions.

The formulation of the intensity measures also led to extensions of Ripley's K -function to the general spatiotemporal K -function to include both distance h and time lag k . The definition of the K -function and the proof of its approximate unbiasedness represents the space-time analysis of the dissertation.

Also proposed was a frequency analysis of spatiotemporal point patterns through the spatiotemporal periodogram. It revealed the intuitive construction of the periodogram as a decomposition of the spatial Fourier frequencies over time. This allowed an obvious interpretation of the spatiotemporal periodogram as a tool for simultaneously capturing dependency structures in space and time.

5.2 Accomplishments

The proposed work has been accomplished. Beginning with the definitions of the four types of spatiotemporal point processes, I established encompassing methods to analyze all spatiotemporal point patterns. However, during this process, I determined that some methods would not be appropriate for all processes (e.g $K_I(h, k)$ and $K_{II}(h, k)$).

I have constructed tests for diagnosing anisotropy in spatial point patterns (Section 2.2.3, p. 38). Theorems were proved relating the intensity measures defined for spatiotemporal point patterns based on a weak stationarity assumption (Section 3.1.3). Through the results of the theorems conditions were given under which particular intensity measures can be examined.

I also determined methods of first-order and reduced second-order intensity estimation of spatiotemporal point patterns (Section 3.1.5, p. 70). Kernel estimators of the first-order spatiotemporal intensity provide glimpses of intensity trends over time. Reduced second-order analyses of spatiotemporal point patterns determine spatiotemporal dependencies. I further showed that if the process is weakly stationary, the estimators of the spatiotemporal K -functions are approximately unbiased (Theorems 3.3 and 3.4, p. 77-78).

I then extended the spectral analysis of spatial point patterns to that of spatiotemporal point patterns. Furthermore, the latter extension has a clear mathematical and practical interpretation (Equation 3.2.7, p. 82). Theorems were proved to show that the spatiotemporal periodogram remained an unbiased estimator for the spatiotemporal spectral density (Theorem 3.5, p. 83). I then showed both mathematically (Corollary 3.5, p. 84) and graphically (Figure 4.4, p. 97) the properties of the spatiotemporal periodogram under CSTR.

I finally was able to apply our methods to a real data set and obtain clear and reasonable results. The inferences based on the analysis of the red-cockaded woodpecker cluster FB002 revealed biologically significant answers that up to now have been unattainable. Through the study of this data, I have further made a reasonable case that if time is an important factor in a spatial point pattern it should not be ignored. Rather, we as statisticians should convince

practitioners that spatiotemporal analysis will lead to more constructive and meaningful results.

5.3 What has been learned

This dissertation contributes research to an emerging area in spatial statistics. I have shown that if anisotropy is present, current methods of analysis are lacking. Furthermore, I have answered the question of how to analyze weakly stationary spatiotemporal point patterns as well as how to compare test a point pattern against the CSTR hypothesis. However, this only scratches the surface and I leave with many open questions.

Though sound in mathematical foundation, the tools I have provided are more exploratory than model building. Without parametric models for spatiotemporal point patterns, I offer only a basis of the inferential tools required. However, I remain undeterred that the work presented here is an important step. Much of the future research in this area will require the methods put forth in this dissertation.

5.4 Future research

As noted in the previous section, my research in spatiotemporal point patterns leaves many questions unanswered. However, I believe that future studies will lead researchers through the questions I have raised.

The following list contains the open questions derived from this dissertation. The items in the list are not specific to strictly spatiotemporal point patterns. In fact, most of the questions not answered in this dissertation came about from research in the spatial domain. The list in no particular order includes:

- Automatic bandwidth selection for kernel estimation of intensities.

- Data tapering for periodogram analysis.
- Wavelet analysis of point patterns.
- Analysis of nonstationary point patterns.
- Construction of parametric spatiotemporal point processes.
- Temporal trend analysis of spatiotemporal point patterns.
- Determining angle of rotation and scaling factors in the presence of geometric anisotropy through periodogram analysis.

Appendix A

Programs

Software for analyzing spatial data has recently been added to prominent statistical software packages such as S-Plus[®] and SAS[®]. However, software for spatiotemporal analyses, and in particular point pattern analysis, is nonexistent. For this reason, a majority of the code was written specifically for the analyses discussed in this dissertation.

The programming language chosen was S-Plus. This choice was first based on the `S+SpatialStats` module provided as an add-on package. The module has built-in functions for spatial point pattern analysis, such as the K -function and inferential envelopes. The second reason for choosing S-Plus is that it is very customizable. Its object-oriented design allows for creating one function to handle many different data types. This makes code design somewhat more complicated but at the same time more versatile in a variety of applications.

The single drawback for using S-Plus over a lower level programming language such as C or Fortran is its poor memory management during large simulations. For this reason, many of the Monte Carlo simulations provided in this dissertation took days to complete and required manual memory management on the part of the user. Future simulation research in this area would greatly benefit from code that is written in a more efficient language.

Below are the necessary S-Plus functions to perform all the analyses in this dissertation.

A.1: `anisotropy.mc()`
 A.2: `anisotropy.pattern()`
 A.3: `anisotropy.rotation()`
 A.4: `hr.analysis()`
 A.5: `kern.hr()`
 A.6: `kern3d()`
 A.7: `Lenv.mc()`
 A.8: `Lhat.II()`
 A.9: `make.stpp.pattern()`
 A.10: `pgram.rho()`
 A.11: `pgram.theta()`
 A.12: `pgram.sp()`
 A.13: `pgram.stp()`
 A.14: `pgram.theta.htest()`

A.1 `anisotropy.mc()`

This function is used to simulate B anisotropic point patterns for given ϕ and σ . The Θ -spectrum is constructed for each pattern. The function returns the ratio of the ordinates at ϕ and $-\phi$.

```
anisotropy.mc <- function(phi,sigma,
                        spp.params=list(process="binomial",
                                       n=200,
                                       boundary=bbox(x=c(-0.5,0.5),y=c(-0.5,0.5))),
                        B=200,write.to) {
theta <- seq(-92.5,92.5,5)*pi/180
phi.j <- c(cut(phi,theta))
cphi.j <- c(cut(-phi,theta))

for(i in 1:B) {
  mc.pattern <- as.matrix(do.call("make.pattern",spp.params))
```

```

mc.ani <- anisotropic.pattern(pattern=mc.pattern,sigma=sigma,theta=phi,plot.it=F)
mc.ani$pgram <- pgram.sp(spp(mc.ani$pattern),freq=list(p=0:16,q=-16:15))
mc.ani$pgram.theta <- pgram.theta(mc.ani$pgram,theta=theta)
mc.ani$pgram.theta$ftheta <- mc.ani$pgram.theta$ftheta

if(i==1) {
  mc.pgram.theta <- mc.ani$pgram.theta
  # get maximum ordinate at phi
  max.phi <- mc.ani$pgram.theta[phi.j,]
  # get minimum ordinate at -phi
  min.phi <- mc.ani$pgram.theta[cphi.j,]
}
else {
  # get maximum ordinate at phi
  max.phi <- rbind(max.phi,mc.ani$pgram.theta[phi.j,])
  # get minimum ordinate at phi
  min.phi <- rbind(min.phi,mc.ani$pgram.theta[cphi.j,])

  mc.pgram.theta$ftheta <- mc.pgram.theta$ftheta + mc.ani$pgram.theta$ftheta
}
}

row.names(max.phi) <- 1:B
row.names(min.phi) <- 1:B
est.scale <- data.frame(theta=max.phi$theta,comp.
                        theta=min.phi$theta,
                        scale=min.phi$ftheta/max.phi$ftheta)
mc.pgram.theta$ftheta <- mc.pgram.theta$ftheta/B

results <- list()
results$theta <-
  round(data.frame(
    result=c(
      mean(max.phi$theta,na.rm=T),
      mean(est.scale$scale,na.rm=T),
      mean(min.phi$ftheta,na.rm=T),
      mean(max.phi$ftheta,na.rm=T),B),
    row.names=c("theta","scale","min.phi","max.phi","B")),4)
results$max.phi<- max.phi
results$min.phi<- min.phi
results$est.scale <- est.scale
results$pgram.theta <- mc.pgram.theta
invisible(results)
}

```

A.2 anisotropy.pattern()

This function takes a point pattern as its argument and returns a point pattern with geometric anisotropy.

```
anisotropic.pattern <- function(pattern,theta=0,sigma=1) {
  center <- c(0,0)
  sides <- matrix(c(-1,-1,1,-1,1,1,-1,1),4,2,byrow=T)*.5
  Q.inv <- anisotropy.rotation(theta,sigma)
  pattern <- pattern%*%Q.inv
  center <- center%*%Q.inv
  sides <- sides%*%Q.inv
  invisible(list(pattern=pattern,center=center,sides=sides,sigma=sigma))
}
```

A.3 anisotropy.rotation()

This function returns the transformation matrix for rotating and scaling a point pattern.

```
anisotropy.rotation <- function(theta=0,sigma=1,inverse=T) {
  rotate <- matrix(c(cos(theta),-sin(theta),sin(theta),cos(theta)),2,2)
  scale <- diag(c(1,sigma))
  Q.inv <- scale%*%rotate
  if(inverse) return(Q.inv)
  solve(Q.inv)
}
```

A.4 hr.analysis()

This function obtains a homerange analysis for a woodpecker cluster. Image plots of kernel intensity estimates with 95% homerange contours are obtained as well as time series plots of 95% homerange areas.

```
hr.analysis <- function(cluster="FB002",
  plot.it=T,
  legend.par=list(x=0.7,y=0.55),
  kernfun=epanechnikov,
```

```

        par.list=list(mfrow=c(4,6),mar=c(0,1,0,1)) {
oldpar <- par()
cat(paste("\nStarting HR analysis for cluster:",cluster,"\n"))
clus <- GetCluster(cluster)
clus$YMNTH.scale <- convert.date(clus$YMNTH)
boundary <- bbox(as.spp(clus[,c("X.scale","Y.scale")]))
clus.df <- data.frame(clus[,c("X.scale","Y.scale","YMNTH")])
names(clus.df) <- c("x","y","date")
clus.months <- unique(clus$YMNTH)
clus.missing <- get.missing(clus.months)
nmissing <- length(clus.missing)
nmonths <- length(clus.months)+nmissing
months <- sort(c(unique(clus.months),clus.missing))
clus.missing <- data.frame(x=rep(-1,nmissing),y=rep(-1,nmissing),date=clus.missing)
clus.df <- rbind(clus.df,clus.missing)
clus.df <- clus.df[order(clus.df$date),]
hr.list <- list()

if(length(plot.it)==1) plot.it <- rep(plot.it,3)
if(plot.it[1]) {
  cat("Plotting 2d intensities...\n")
  par(par.list)
  for(i in 1:length(months)) {
    month <- months[i]
    clus.2d <- clus.df[which(clus.df$date==month),c("x","y")]
    if(nrow(clus.2d)>1) {
      pp <- data.frame(x=clus.2d$x,y=clus.2d$y)
      lambda.s <- intensity(pp,
                           method="kernel",
                           kernfun=kernfun,
                           bw=0.15,nx=50,ny=50,
                           boundary=boundary)
      if(!color) lambda.s$z <- -lambda.s$z
      scaled.image(lambda.s,axes=F,ylim=c(0,1))
      points(x=clus.2d[,1],y=clus.2d[,2],pch=".",col=6)
      kern.hr(pp,kernfun=kernfun,bw=0.15,n=c(50,50),print.it=F)
      extend <- 0.01
    }
  }
  else {
    scaled.plot(x=0:1,y=0:1,xlim=c(0,1),ylim=c(0,1),type="n",xlab="",ylab="",axes=F)
    polygon(x=c(0,1,1,0),y=c(0,0,1,1),density=F,col=2,lwd=3)
    text(x=.5,y=0.5,label="MISSING",cex=1,col=3,font=4)
    extend <- 0
  }
}

```

```

    }
    polygon(x=c(0,1+extend,1+extend,0),y=c(1.035,1.035,1.145,1.145),col=4,lwd=3)
    text(x=.5,y=1.103,label=month,cex=1,col=0,font=4)
  }
  cat("\n\n")
}

clus.kern3d <- kern3d(clus[,c("X.scale","Y.scale","YMNTH.scale")],
                    n=c(50,50,nmonths),lims=c(0,1,0,1,0,1),
                    bw.sp=0.15,bw.t=0.15,
                    kernfun.sp=kernfun,kernfun.t=kernfun)

if(plot.it[2]) {
  cat("Plotting 3d intensities...\n")
  par(par.list)
  for(i in 1:length(months)) {
    month <- months[i]
    clus.2d <- clus.df[which(clus.df$date==month),c("x","y")]
    lambda.s <- list(x=clus.kern3d$x,y=clus.kern3d$y,z=clus.kern3d$z[[i]])
    scaled.image(lambda.s,axes=F)
    kern.hr(x=lambda.s$x,y=lambda.s$y,z=lambda.s$z,print.it=F,plot.it=T)
    if(nrow(clus.2d)>1) points(x=clus.2d[,1],y=clus.2d[,2],pch=".",col=6)
    polygon(x=c(-0.01,1.01,1.01,-0.01),y=c(1.035,1.035,1.145,1.145),col=4)
    text(x=.5,y=1.103,label=month,cex=ifelse(max(par.list$mar)>5,3,1),col=0,font=4)
  }
  cat("\n\n")
}

cat("Computing homeranges...\t")
hr3d <- unlist(lapply(clus.kern3d$z,
                    function(x,xx,yy) kern.hr(x=xx,y=yy,z=x,print.it=F,plot.it=F)$area,
                    xx=clus.kern3d$x,yy=clus.kern3d$y))
hr.list$hr3d <- data.frame(time=seq(0,1,length=length(hr3d)),hr3d=hr3d,row.names=NULL)

clus.kern2d <- list()
clus.time <- unique(clus$YMNTH)
hr2d <- unlist(lapply(split(clus[,c("X.scale","Y.scale")],clus[, "YMNTH"]),
                    function(x,K) {
                      kern.hr(x=x,n=c(50,50),lims=c(0,1,0,1),bw=0.15,kernfun=K,print.it=F,plot.it=F)$area
                    },K=kernfun))
hr.list$hr2d <- data.frame(time=names(hr2d),hr2d=hr2d,row.names=NULL)

if(plot.it[3]) {
  par(mar=c(5,4,3,2)+.1,mgp=c(3,1.5,0),mfrow=c(1,1))

```

```

cat("Plotting homeranges...\n\n")
ylim <- c(min(hr2d),max(hr3d))
plot(x=c(0,1),type="n",xlim=c(0,1),ylim=ylim,axes=F,xlab="Year/Month",ylab="Area",col=3)
box()
axis(side=2,at=seq(0.0,0.5,0.1),labels=seq(0.0,0.5,0.1),cex=0.75,crt=0,col=2,font=6)
clus.len <- length(unique(clus.df[,3]))
axis(side=1,at=seq(0,1,length=clus.len),labels=unique(clus.df[,3]),line=0,cex=1,col=2,font=6)
title(main=paste("95% Homerange for cluster",cluster),col=7,font=6)
lines(x=unique(clus$YMNTH.scale),y=hr2d,col=5,lwd=3)
lines(x=seq(0,max(clus$YMNTH.scale),length=nmonths),y=hr3d,col=6,lwd=3)
abline(v=unique(clus$YMNTH.scale),lty=2,col=2)
legend(x=legend.par$x,y=legend.par$y,legend=c("Full","Conditional"),lty=c(1,1),col=c(6,5),lwd=c(3,3))
}
cat("\n\n")

par(oldpar)
invisible(hr.list)
}

```

A.5 kern.hr()

This function calculates the $(1 - \alpha) \times 100\%$ homerange for a given intensity estimate.

```

kern.hr <- function(x,y,z,bw,n=c(25,25),lims,alpha=0.05,
                    kernfun=epanechnikov,
                    plot.it=T,print.it=T,addmode=T,symbol=6,...) {
# check if x,y,z is the density estimate
if(!missing(z) || (is.list(x) && !is.null(x$z))) {
  if(is.list(x)) {
    y <- x$y
    z <- x$z
    x <- x$x
  }
  f <- list(z=z)
}
# otherwise x,y is raw data
else {
  if(is.list(x) && !is.null(x$x) && !is.null(x$y)) {
    y <- x$y
    x <- x$x
  }
}

```

```

if(missing(y) && is.matrix(x)) {
  y <- x[,2]
  x <- x[,1]
}
if(missing(lims)) {
  lims.x <- range(x)
  lims.y <- range(y)
}
else if(is.list(lims)) {
  lims.x <- lims[[1]]
  lims.y <- lims[[2]]
}
else {
  lims.x <- c(lims[1],lims[2])
  lims.y <- c(lims[3],lims[4])
}
if(missing(bw)) bw <- bandwidth.sp(x,y)
# construct density estimate
f <- kern2d(x=x,y=y,bw=bw,
            nx=n[1],ny=n[2],
            lims=c(lims.x,lims.y),
            kernfun=kernfun)
x <- f$x
y <- f$y
z <- f$z
}
lims.x <- range(x)
lims.y <- range(y)
n <- c(length(x),length(y))

# make area slightly larger so z estimate is at the
# center of each grid cell rather than on a corner
shift.x <- (lims.x[2]-lims.x[1])/(n[1]+1)
shift.y <- (lims.y[2]-lims.y[1])/(n[2]+1)
lims.shift.x <- c(lims.x[1]-0.5*shift.x,lims.x[2]+0.5*shift.x)
lims.shift.y <- c(lims.y[1]-0.5*shift.y,lims.y[2]+0.5*shift.y)

# nodes will be the center of each grid cell
nodes.x <- seq(lims.shift.x[1],lims.shift.x[2],length=n[1]+1)
nodes.y <- seq(lims.shift.y[1],lims.shift.y[2],length=n[2]+1)

# compute area of each cell
area.grid <- diff(nodes.x)%*%t(diff(nodes.y))

```

```
# reduce area of cells on the edges or corners
area.grid[1,] <- area.grid[1,]*0.5
area.grid[,1] <- area.grid[,1]*0.5
area.grid[nrow(area.grid),] <- area.grid[nrow(area.grid),]*0.5
area.grid[,ncol(area.grid)] <- area.grid[,ncol(area.grid)]*0.5

# compute volume by multiplying area and height
volume <- area.grid*f$z
# scale volume so it sums to 1.0
volume <- volume/sum(volume)

# unwrap matrix of probabilities into a vector
# create row and column indices
unwrap <- data.frame(prob=c(volume),
                    row=rep(1:n[1],times=n[2]),
                    col=rep(1:n[2],each=n[1]))
# order grid cells by probability
unwrap.order <- unwrap[order(unwrap$prob),]
# determine mode and location of mode
mode <- unwrap.order[n[1]*n[2],"prob"]
mode.i <- unwrap.order[n[1]*n[2],c("row","col")]
mode.loc <- c(nodes.x[mode.i$row],nodes.y[mode.i$col])

# determine HRc [Home Range complement]
cumsum.index <- cumsum(unwrap.order$prob)<=alpha
# i is the number of probabilities whose sum is < alpha
i <- sum(cumsum.index,na.rm=T)
HRc <- sum(unwrap.order$prob[cumsum.index])

# determine which of the grid cells are
# in the home range using the value of i
unwrap.order$in.hull <- c(rep(0,i),rep(1,nrow(unwrap)-i))
# determine adding all the cell area inside the hull
area <- sum(c(area.grid)*unwrap.order$in.hull)

# unsort to restore row and columns
unwrap <- unwrap.order[row.names(unwrap),]

# restore vector of probabilities to matrix
wrap <- matrix(unwrap$in.hull,nrow=n[1])

# compute nodes for which to plot contour
edges.x <- seq(lims.x[1],lims.x[2],length=n[1])
```

```

edges.y <- seq(lims.y[1],lims.y[2],length=n[2])

# plot (1-alpha)x100% Home Range contour
coords <- contour(x=edges.x,
                 y=edges.y,
                 z=wrap,
                 nlevels=1,
                 add=T,
                 save=T,
                 plotit=plot.it,
                 labex=0,...)$"1"

# add mode if asked
if(addmode && plot.it) points(x=mode.loc[1],y=mode.loc[2],pch=symbol,lwd=3,col=6)
# print area and alpha level achieved
if(print.it) cat(paste("\nArea =",round(area,4),"\nalpha =",round(HRc,4),"\n"))

# return coordinates of contour, area, and alpha level achieved
invisible(list(coords=coords,area=area,alpha=HRc,mode=list(mode=mode,location=mode.loc)))
}

```

A.6 kern3d()

This function constructs a 3-dimensional kernel intensity estimate of a spatiotemporal point pattern.

```

kern3d <- function(coords,bw.sp,bw.t,
                 n=c(25,25,25),
                 at.time=(n[3]==length(unique(coords[,3]))),
                 lims=c(range(coords[,1]),range(coords[,2]),range(coords[,3])),
                 kernfun.sp=epanechnikov,kernfun.t=epanechnikov) {
  x <- split(coords[,1],coords[,3])
  y <- split(coords[,2],coords[,3])
  time <- unique(coords[,3])
  if(missing(bw.sp)) stop("Need to give a spatial bandwidth \"bw.sp\".")
  if(missing(bw.t)) stop("Need to give a temporal bandwidth \"bw.t\".")
  if(length(bw.sp)==1) bw.sp <- rep(bw.sp,length(time))
  gx <- seq(lims[1],lims[2],length=n[1])
  gy <- seq(lims[3],lims[4],length=n[2])
  if(is.numeric(at.time))
    gt <- at.time

```

```

else {
  if(at.time)
    gt <- time
  else
    gt <- seq(lims[5],lims[6],length=n[3])
}
at <- outer(X=gt,Y=time,FUN="-")/bw.t
z <- list()
for(i in 1:length(time)) {
  ax <- outer(X=gx,Y=x[[i]],FUN="-")/bw.sp[i]
  ay <- outer(X=gy,Y=y[[i]],FUN="-")/bw.sp[i]
  len <- length(x[[i]])
  X <- matrix(data=kernfun.sp(ax),nrow=n[1],ncol=len)
  Y <- matrix(data=kernfun.sp(ay),nrow=n[2],ncol=len)
  z[[i]] <- (X%*%t(Y))/bw.sp[i]^2
}
z.st <- list()
for(tt in 1:length(gt)) {
  z.st[[tt]] <- matrix(0,nrow=n[1],ncol=n[2])
  for(j in 1:length(time))
    z.st[[tt]] <- z.st[[tt]] + kernfun.t((gt[tt]-time[j])/bw.t)*z[[j]]/bw.t
}
invisible(list(x=gx,y=gy,t=gt,z=z.st,bw.sp=bw.sp,bw.t=bw.t))
}

```

A.7 Lenv.mc()

This program performs the L -analysis for a spatial point pattern. Included are computation of the observed \hat{L} -function, a simulated envelope, Cramér-von Mises-type statistic, and the empirical p-value.

```

Lenv.mc <- function(object,
  nsims = 100,
  maxdist,
  ndist = 100,
  process = "binomial",
  boundary = bbox(object),
  add = T, col = 2, lty = 2, ...) {
  object <- as.spp(object, drop = T)
  npoints <- dim(object)[1]
  bdy.x <- unique(boundary$x)

```

```

bdy.y <- unique(boundary$y)
if(length(bdy.x) != 2 || length(bdy.y) != 2)
  stop("boundary should be a rectangular box")
if(missing(maxdist) || is.null(maxdist))
  maxdist <- 0.5 * sqrt(diff(bdy.x)^2 + diff(bdy.y)^2)

# function for computing the Cramer-von Mises statistic
# as given by Cressie (1993, p. 642)
cvm <- function(x,K) (sqrt(approx(x=K$x,y=K$y,xout=x)$y)-sqrt(pi)*x)^2

# Compute observed statistics
cat("\n\t\tComputing Observed Statistics...")
lhat.obs <- Lhat(object, maxdist = maxdist, ndist = ndist, boundary = boundary, plot = F)
hx <- lhat.obs$values[, "dist"]
lb <- hx[1]
ub <- hx[length(hx)]
k.obs <- integrate(cvm,lb,ub,K=data.frame(x=hx,y=pi*lhat.obs$values[, "Lhat"]^2))$integral

# Compute MC statistics
cat("\n\t\tCreating Data Sets...")
how.many <- rep(npoints, nsims)
sims <- lapply(how.many, make.pattern, process = process, boundary = boundary, ...)
cat("\n\t\tComputing Simulated L-functions...")
Larray <- sapply(sims, FUN = function(x, maxdist, ndist, boundary, plot)
  Lhat(x,maxdist=maxdist,ndist=ndist,boundary=boundary,plot=F)$values[, "Lhat"],
  maxdist=maxdist,ndist=ndist,boundary=boundary,plot=F)
hu <- apply(Larray, 1, max)
hl <- apply(Larray, 1, min)
ha <- apply(Larray, 1, sum)
cat("\n\t\tComputing Simulated Cramer-von Mises Statistics...")
k <- apply(Larray,2,
  function(x,f,hx) {
    lb <- hx[1]
    ub <- hx[length(hx)]
    integrate(f,lb,ub,K=data.frame(x=hx,y=pi*x^2))$integral
  },
  f=cvm,hx=hx)

p <- (nsims+1-rank(c(k,k.obs))[nsims+1])/nsims
ret.val <- list(spp = object,
  dist = hx,
  Lhat = lhat.obs$values[, "Lhat"],
  lower = hl,

```

```

        upper = hu,
        average = ha/nsims,
        cvm = k,
        cvm.obs = k.obs,
        p = p)
if(add) {
  lines(ret.val$dist, ret.val$average, col = col)
  lines(ret.val$dist, ret.val$upper, lty = lty, col = col)
  lines(ret.val$dist, ret.val$lower, lty = lty, col = col)
}
invisible(ret.val)
}

```

A.8 Lhat.II()

This program simulates a spatial point pattern sampled in time. The spatiotemporal L_{II} -function and simulated envelope are also obtained.

```

set.seed(10)
t <- 6
n <- 50
stp.pattern <- make.pattern("binomial",n=n*t)
stp.pattern$time <- rep(1:t,each=n)

for(k in 0:(t-1)) {
  first <- T
  for(j in 1:(t-k)) {
    subset <- which(stp.pattern$time==j | stp.pattern$time==j+k)
    data <- stp.pattern[subset,1:2]
    if(first) Lhat.temp <- Lhat(spp(data),maxdist=0.5,ndist=100,plot.it=F)$values
    else Lhat.temp[,"Lhat"] <- Lhat.temp[,"Lhat"] +
      Lhat(spp(data),maxdist=0.5,ndist=100,plot.it=F)$values[,"Lhat"]
    first <- F
  }
  if(k==0) Lhat.temp[,"Lhat"] <- Lhat.temp[,"Lhat"]/t
  else Lhat.temp[,"Lhat"] <- Lhat.temp[,"Lhat"]/(t-k)

  if(k==0) Lhat.lag <- data.frame(Lhat.temp,lag=0)
  else Lhat.lag <- rbind(Lhat.lag,data.frame(Lhat.temp,lag=k))
}

```

```

B <- 100
stp.pattern.mc <- lapply(1:B,
  function(x,t,n) {
    pattern <- make.pattern("binomial",n=n*t)
    pattern$time <- rep(1:t,each=n)
    pattern
  },t=t,n=n)

Larray <- sapply(stp.pattern.mc,function(x,t) {
  for(k in 0:(t-1)) {
    first <- T
    for(j in 1:(t-k)) {
      subset <- which(x$time==j | x$time==j+k)
      data <- x[subset,1:2]
      if(first) Lhat.temp <- Lhat(spp(data),maxdist=0.5,ndist=100,plot.it=F)$values
      else      Lhat.temp[, "Lhat"] <- Lhat.temp[, "Lhat"] +
        Lhat(spp(data),maxdist=0.5,ndist=100,plot.it=F)$values[, "Lhat"]
      first <- F
    }
    if(k==0) Lhat.temp[, "Lhat"] <- Lhat.temp[, "Lhat"]/t
    else     Lhat.temp[, "Lhat"] <- Lhat.temp[, "Lhat"]/(t-k)

    if(k==0) Lhat.lag <- data.frame(Lhat.temp,lag=0)
    else     Lhat.lag <- rbind(Lhat.lag,data.frame(Lhat.temp,lag=k))
  }
  Lhat.lag[, "Lhat"]
},t=t)

Lmax <- data.frame(dist=Lhat.lag[, "dist"],Lmax=apply(Larray,1,max),lag=Lhat.lag[, "lag"])
Lmin <- data.frame(dist=Lhat.lag[, "dist"],Lmin=apply(Larray,1,min),lag=Lhat.lag[, "lag"])

```

A.9 make.stpp.pattern()

This function creates one of the four types of spatiotemporal point patterns. Plots are obtained if requested.

```

make.stpp.pattern <- function(spp.params=list(process="poisson",lambda=25),
  t,process="earthquake",
  time.func="rexp",time.params=list(rate=1),
  plot.it=F,return.data=T,as.list=T) {
  switch(casefold(process),

```

```

"earthquake"=","eq"= {
  if(is.null(spp.params$boundary))
    spp.params$boundary <- list(x=c(0,0,1,1),y=c(0,1,1,0))
  pattern <- do.call("make.pattern",spp.params)
  time.params$n <- nrow(pattern)
  time <- do.call(time.func,time.params)
  pattern$t <- sample(0:(nrow(pattern)-1))
  pattern$sort <- order(pattern$t)
  pattern <- pattern[pattern$sort,]
  pattern$time <- cumsum(time)-time[1]
  if(plot.it) {
    boundary <- list(x=c(-0.05,-0.05,0.05,0.05)+spp.params$boundary$x,
                    y=c(-0.05,0.05,0.05,-0.05)+spp.params$boundary$y)
    plot(pattern,type="n",xlim=range(boundary$x),ylim=range(boundary$y),axes=F,xlab="",ylab="")
    text(x=pattern$x,y=pattern$y,label=pattern$t,cex=0.75,col=2)
    polygon(x=boundary$x,y=boundary$y,lwd=3,col=6,density=F)
    apply(cbind(pattern$time,1:nrow(pattern)),1,function(x,range.t,boundary) {
      max.x <- max(boundary$x)
      min.y <- min(boundary$y)
      max.y <- max(boundary$y)
      y <- min.y+(max.y-min.y)*(x[1]-range.t[1])/diff(range.t)
      lines(x=c(max.x,max.x)+c(0.10,0.15),y=c(y,y),col=3)
      if(x[2]%%5==0) text(x=max.x+0.17,y=y,labels=x[2],cex=.75)
    },range.t=range(pattern$time),boundary=spp.params$boundary)
    text(x=max(boundary$x)+0.08,y=max(boundary$y)+0.02,labels="TIME")
    polygon(x=max(boundary$x)+c(0.02,0.02,0.15,0.15),y=boundary$y,col=2,density=F)
    title(main="Earthquake Process")
    spp.label <- unlist(spp.params)
    spp.mtext <- spp.desc(unlist(spp.params))
    mtext(text=spp.mtext,side=3,line=0.5)
  }
  pattern <- pattern[,c("x","y","time","t")]
},
"explosion"=","ex"= {
  time.params$n <- t
  time <- do.call(time.func,time.params)
  time <- cumsum(time)-time[1]
  pattern <- data.frame()
  if(!is.list(spp.params[[1]]))
    spp.params <- list(spp.params)
  for(i in 1:t) {
    j <- ifelse(i%%length(spp.params)==0,length(spp.params),i%%length(spp.params))
    if(is.null(spp.params[[j]]$boundary))

```

```

    spp.params[[j]]$boundary <- bbox(x=c(0,1),y=c(0,1))
    pattern.i <- do.call("make.pattern",spp.params[[j]])
    pattern.i$time <- rep(time[i],nrow(pattern.i))
    pattern.i$order <- rep(i,nrow(pattern.i))
    if(i==1) pattern <- pattern.i
    else    pattern <- rbind(pattern,pattern.i)
  }
  if(plot.it) {
    boundary <- list(x=c(-0.05,-0.05,0.05,0.05)+spp.params[[1]]$boundary$x,
                    y=c(0.05,-0.05,-0.05,+0.05)+spp.params[[1]]$boundary$y)
    plot(pattern,type="n",xlim=range(boundary$x),ylim=range(boundary$y),axes=F,xlab="",ylab="")
    text(x=pattern$x,y=pattern$y,labels=pattern$order,cex=0.75,col=2)
    polygon(x=boundary$x,y=boundary$y,lwd=3,col=6,density=F)
    apply(pattern[,3:4],1,function(x,range.t,boundary) {
      max.x <- max(boundary$x)
      min.y <- min(boundary$y)
      max.y <- max(boundary$y)
      y <- min.y+(max.y-min.y)*(x[1]-range.t[1])/diff(range.t)
      lines(x=c(max.x,max.x)+c(0.10,0.15),y=c(y,y),col=3)
      if(x[2]%5==0) text(x=max.x+0.17,y=y,labels=x[2],cex=.75)
    },range.t=range(pattern$time),boundary=spp.params[[1]]$boundary)
    text(x=max(boundary$x)+0.08,y=max(boundary$y)+0.02,labels="TIME")
    polygon(x=max(boundary$x)+c(0.02,0.02,0.15,0.15),y=boundary$y,col=2,density=F)
    title(main="Explosion Process")
  }
},
"birthdeath","bd","sampled"= {
  pattern <- list()
  if(!is.list(spp.params[[1]]))
    spp.params <- list(spp.params)
  for(i in 1:t) {
    j <- ifelse(i%length(spp.params)==0,length(spp.params),i%length(spp.params))
    if(is.null(spp.params[[j]]$boundary))
      spp.params[[j]]$boundary <- bbox(x=c(0,1),y=c(0,1))
    boundary <- list(x=c(min(spp.params[[j]]$boundary$x),max(spp.params[[j]]$boundary$x)),
                    y=c(min(spp.params[[j]]$boundary$y),max(spp.params[[j]]$boundary$y)))
    pattern[[i]] <- do.call("make.pattern",spp.params[[j]])
    if(plot.it) {
      spp.mtext <- spp.desc(unlist(spp.params[[j]]))
      plot(pattern[[i]],pch=".",xlim=boundary$x,ylim=boundary$y)
      title(main=paste("Time =",i))
      mtext(text=spp.mtext,side=3,line=.8)
    }
  }
}

```

```

    }
  },
  stop(paste("Process",process,"not supported.")))
if(!as.list) {
  n.pattern <- unlist(lapply(pattern,function(x) nrow(x)))
  pattern.df <- data.frame()
  for(i in 1:t) {
    temp.df <- cbind(pattern[[i]],time=rep(i,each=n.pattern[i]))
    if(i==1) pattern.df <- temp.df
    else pattern.df <- rbind(pattern.df,temp.df)
  }
  pattern <- pattern.df
}
if(return.data) invisible(pattern)
else invisible()
}

```

A.10 pgram.rho()

This function takes a spatial periodogram as its argument and constructs the R -spectrum.

```

pgram.rho <- function(object,rho,maxrho) {
  if(is.list(object) &&
    !is.null(object$p) &&
    !is.null(object$q) &&
    !is.null(object$pgram)) {
    p <- object$p
    q <- object$q
    pgram <- object$pgram
  }
  else stop("object must contain p, q, and pgram as elements.")
  pq <- as.matrix(expand.grid(p,q))
  data.rho <- data.frame(p=pq[,1],
                       q=pq[,2],
                       rho=sqrt(pq[,1]^2+pq[,2]^2),
                       pgram=c(object$pgram))
  if(missing(rho)) {
    if(missing(maxrho)) rho <- 0:ceiling(max(data.rho$rho))
    else rho <- 0:maxrho
  }
  data.rho$group.rho <- as.vector(cut(data.rho$rho,breaks=rho))
}

```

```

data.rho <- data.rho[order(data.rho$group.rho),]
data.rho <- data.rho[-nrow(data.rho),]
split.rho <- split(data.rho$pgram,data.rho$group.rho)
nrho <- unlist(lapply(split.rho,function(x) length(x)))
frho <- unlist(lapply(split.rho,mean))
result <- data.frame(rho=rho[-1],frho=frho)
result$lowerCI <- qchisq(0.025,2*nrho)/(2*nrho)
result$upperCI <- qchisq(0.975,2*nrho)/(2*nrho)
result$nrho <- nrho
result
}

```

A.11 pgram.theta()

This function takes a raw spatial periodogram as its argument and constructs the Θ -spectrum.

```

pgram.theta <- function(object,theta) {
  if(is.list(object) && !is.null(object$p) && !is.null(object$q) && !is.null(object$pgram)) {
    p <- object$p
    q <- object$q
    pgram <- object$pgram
  }
  else stop("object must contain p, q, and pgram as elements.")
  pq <- expand.grid(p,-q)
  data.theta <- data.frame(p=pq[,1],q=pq[,2],theta=atan(pq[,2]/pq[,1]),pgram=c(pgram))
  if(missing(theta)) theta <- seq(-95,95,10)*pi/180
  data.theta$group.theta <- as.vector(cut(data.theta$theta,breaks=theta))
  data.theta <- data.theta[order(data.theta$theta),]
  data.theta <- data.theta[-nrow(data.theta),]
  split.theta <- split(data.theta$pgram,data.theta$group.theta)
  ntheta <- unlist(lapply(split.theta,function(x) length(x)))
  ftheta <- unlist(lapply(split.theta,mean))
  dt <- min(diff(theta))
  theta <- round(seq(min(theta)+dt/2,max(theta)-dt/2,dt),4)
  result <- data.frame(theta=theta,ftheta=ftheta)
  result$lowerCI <- qchisq(0.025,2*ntheta)/(2*ntheta)
  result$upperCI <- qchisq(0.975,2*ntheta)/(2*ntheta)
  result$ntheta <- ntheta
  result
}

```

A.12 pgram.sp()

This function takes a spatial point pattern as its argument and returns either the raw or smoothed periodogram.

```
pgram.sp <- function(object,
                      freq,freq0.rm=T,
                      boundary=bbox(object),
                      smooth=!freq0.rm,bw=1>window,
                      npoints.p=25,npoints.q=2*npoints.p) {
  Lx <- diff(range(boundary$x))
  Ly <- diff(range(boundary$y))
  L.inv <- diag(c(1/Lx,1/Ly))
  n <- nrow(object)
  object <- as.matrix(object)

  # rescale data to unit square
  object[,1:2] <- object[,1:2]*%L.inv

  # obtain frequencies
  if(missing(freq)) freq <- list(p=0:16,q=-16:15)
  omega <- lapply(freq,function(x) 2*pi*x)
  omega <- as.matrix(expand.grid(omega$p,omega$q))
  n.freq <- unlist(lapply(freq,length))

  # remember location of frequency (0,0)
  index0 <- which(omega[,1]==0 & omega[,2]==0)%/max(freq$p)

  # compute Fourier coefficients for all frequencies
  i <- complex(real=0,imag=1)
  J <- apply(omega,1,function(x,data,i) {
    omega.s <- data*%matrix(x,nrow=2)
    sum(exp(-i*omega.s))
  },data=object[,1:2],i=i)

  # obtain spatial periodogram
  pgram <- matrix(Mod(J)^2,nrow=n.freq[1],ncol=n.freq[2])

  # remove frequency (0,0)
  if(!is.na(index0)) {
    f00 <- pgram[1,index0]
    if(freq0.rm) pgram[1,index0] <- 0
  }
}
```

```

# smooth periodogram if requested
if(smooth) {
  if(missing(window)) {
    cat("\n")
    warning("\n\tWindow function required to smooth periodogram.")
    cat("\tReturning raw periodogram.\n")
  }
  else {
    if(length(bw)==1) bw <- rep(bw,2)
    gp <- seq(freq$p[1],freq$p[n.freq[1]],length=npoints.p)
    gq <- seq(freq$q[1],freq$q[n.freq[1]],length=npoints.q)
    ap <- outer(gp,freq$p,"-")/prod(bw)
    aq <- outer(gq,freq$q,"-")/prod(bw)
    kappa.p <- matrix(window(ap),npoints.p,n.freq[1])
    kappa.q <- matrix(window(aq),npoints.q,n.freq[2])
    pgram <- kappa.p%*%pgram%*%t(kappa.q)/prod(bw)
    freq <- list(p=gp,q=gq)
  }
}
list(p=freq$p,
     q=freq$q,
     pgram=pgram/n,
     f00=f00/n,
     smooth=smooth,
     freq0.rm=freq0.rm)
}

```

A.13 pgram.stp()

This function takes a sampled point pattern as its argument and returns either the raw or smoothed spatiotemporal periodogram.

```

pgram.stp <- function(object,freq,
                     smooth=F,npoints=25,bw,kernfuns=list(dnorm),
                     plot.it=F,plot.type=image,
                     rm.freq0=T,positive=F) {
  # computes the Fourier coefficients for each time t
  Jpq <- function(object,p,q) {
    object <- as.matrix(object)
    Lx <- diff(range(object[,1]))

```

```

Ly <- diff(range(object[,2]))
n <- nrow(object)
object[,1:2] <- cbind(object[,1]/Lx,object[,2]/Ly)
omega.p <- 2*pi*p
omega.q <- 2*pi*q
omega <- as.matrix(expand.grid(omega.p,omega.q))
i <- complex(real=0,imaginary=1)
J <- apply(omega,1,
  function(x,data,i) {
    omega.s <- data%*%matrix(x,nrow=2)
    sum(exp(i*omega.s))
  },data=object[,1:2],i=i)
J
}

### begin periodogram code ###
if(missing(freq)) {
  p <- 0:16
  q <- -16:15
  index0 <- c(1,17)
}
else {
  p <- freq$p
  q <- freq$q
  index0 <- c(index0f(p,0),index0f(q,0))
  if(rm.freq0 && (index0[1] < 0 || index0[2] < 0)) {
    warning("Frequency 0 not computed.\n")
    rm.freq0 <- F
  }
}
object <- object[,1:3]
n <- nrow(object)
names(object) <- c("x","y","date")
times <- object$date
nt <- unique(times)
missing.months <- get.missing(unique(nt))
if(!is.na(sum(missing.months))) {
  months <- sort(c(nt,missing.months))
  nmissing <- length(missing.months)
  missing.months <- data.frame(x=rep(-1,nmissing),y=rep(-1,nmissing),date=missing.months)
  object <- rbind(object,missing.months)
  object <- object[order(object$date),]
}

```

```

else {
  months <- nt
  nmissing <- 0
}
nmonths <- length(months)
stp <- split(object[,c("x","y","date")],object[, "date"])

Jt <- lapply(stp,function(x,p,q,Jpq) {
  month <- unique(x$date)
  x <- x[,c("x","y")]
  if(x[1,1] < 0) {
    cat(paste("_",month," ",sep=""))
    j <- matrix(0,length(p),length(q))
  }
  else {
    cat(paste(month," ",sep=""))
    j <- Jpq(x,p,q)
  }
  j
},p=p,q=q,Jpq=Jpq)
Jt <- matrix(unlist(Jt),ncol=nmonths)
Ist <- apply(Jt,1,function(x,pos,n)
             length(x)*spec.fft(x,is.fourier=F,as.db=F,positive=pos)$pgram/n,
             pos=positive,n=n)
ngamma <- nrow(Ist)
if(positive) r <- 1:ngamma-1
else        r <- -((ngamma-1)%/2):(ngamma%/2)
Ist <- split(Ist,1:ngamma)
Ist <- lapply(Ist,function(x,p,q) matrix(x,length(p),length(q)),p=p,q=q)
Ist <- lapply(Ist,function(x,p,q) list(p=p,q=q,pgram=x),p=p,q=q)
for(i in 1:ngamma) Ist[[i]]$r <- r[i]

if(smooth || !missing(bw)) {
  if(smooth && missing(bw)) stop("Supply bandwidth to smooth periodogram.")
  if(length(npoints)==1) npoints <- rep(npoints,3)
  if(length(bw)==1) bw <- rep(bw,3)
  if(length(kernfun)==1) { kernfun.sp <- kernfun.t <- kernfun[[1]]; }
  else { kernfun.sp <- kernfun[[1]]; kernfun.t <- kernfun[[2]]; }
  Ist <- lapply(Ist,
               function(x,bw,npoints,kernfun)
                 smooth3d(x,bw=bw,npoints=npoints,kernfun=kernfun),
               bw=bw[1:2],npoints=npoints[1:2],kernfun=kernfun.sp)
  Kst <- list()
}

```

```

lims.t <- range(unique(nt))
gt <- seq(lims.t[1],lims.t[2],length=npoints[3])
for(tt in 1:length(gt)) {
  Kst[[tt]] <- list(pgram=matrix(0,nrow=npoints[1],ncol=npoints[2]))
  Kst[[tt]]$p <- Ist[[1]]$p
  Kst[[tt]]$q <- Ist[[1]]$q
  for(j in 1:length(nt))
    Kst[[tt]]$pgram <- Kst[[tt]]$pgram +
      kernfun.t((gt[tt]-nt[j])/bw[3])*Ist[[j]]$pgram/bw[3]
}
Ist <- Kst
}
if(plot.it) {
  invisible(lapply(Ist,function(x,plot.type)
    plot.type(x=x$p,y=x$q,z=x$pgram,xlab="p",ylab="q",zlab="I(p,q,r)",
    plot.type=plot.type))
}
list(Ist=Ist,p=p,q=q,r=r)
}

```

A.14 pgram.theta.htest()

This function takes a Θ -spectrum as its argument and returns the ratio test for anisotropy.

```

pgram.theta.htest <- function(pgtheta) {
  ntheta <- pgtheta$ntheta
  ftheta <- pgtheta$ftheta
  theta <- pgtheta$theta

  pgtheta.lower <- pgtheta[which(pgtheta$theta<=0),]
  pgtheta.lower <- pgtheta.lower[nrow(pgtheta.lower):1,]
  pgtheta.lower$theta <- -pgtheta.lower$theta

  pgtheta.upper <- pgtheta[which(pgtheta$theta>=0),]
  quotient <- data.frame(theta=pgtheta.upper$theta)
  quotient$ntheta <- pgtheta.upper$ntheta
  quotient$nltheta <- pgtheta.lower$ntheta

  quotient$ratio <- pgtheta.upper$ftheta/pgtheta.lower$ftheta
  quotient$lowerF <- qf(0.025,2*quotient$ntheta,2*quotient$nltheta)
}

```

```
quotient$meanF <- quotient$nltheta/(quotient$nltheta-2)
quotient$upperF <- qf(0.975,2*quotient$nutheta,2*quotient$nltheta)

invisible(quotient)
}
```

Bibliography

- [1] Baddeley, A. J. and Silverman, B. W. (1984) "A cautionary example on the use of second-order methods for analyzing point patterns." *Biometrics*. **40**: 1089-1093.
- [2] Bartlett, M. S. (1964) "The spectral analysis of two-dimensional point processes." *Biometrika*. **51**, (3): 299-311.
- [3] Bartlett, M. S. (1974) "The statistical analysis of spatial pattern." *Advances in Applied Probability*. **6**: 336-358.
- [4] Bartlett, M. S. (1975) *The Statistical Analysis of Spatial Pattern*. Chapman and Hall, London.
- [5] Bartlett, M. S. (1978) *Stochastic Processes. Methods and Applications*. Cambridge University Press, London.
- [6] Box, G. E. P, Jenkins, G. M. and Reinsel, G. C. (1994) *Time Series Analysis. Forecasting and Control*. Prentice-Hall, Inc, Englewood Cliffs, New Jersey.
- [7] Brillinger, D. R. (1972) "The spectral analysis of stationary interval functions." *Proceedings of the 6th Berkeley Symposium on Mathematical Statistics and Probability*. **1**: 483-513.
- [8] Burt, W. H. (1943) "Territoriality and homerange concepts as applied to mammals." *Journal of Wildlife Management*. **54**: 310-315.

- [9] Chilès, J. P. and Delfiner: (1999) *Geostatistics. Modeling Spatial Uncertainty*. Wiley and Sons, New York.
- [10] Choi, E. and Hall: (1999) “Nonparametric Approach to Analysis of Space-Time data on Earthquake Occurrences.” *Journal of Computational and Graphical Statistics*. **8**, (4): 733-748.
- [11] Choi, E. and Hall: (2000) “On the estimation of poles in intensity functions.” *Biometrika*. **87**, (2): 251-263.
- [12] Cressie, N. A. C. (1993) *Statistics for Spatial Data. Revised Edition*. Wiley and Sons, New York.
- [13] Daley, D. and Vere-Jones, D. (1988) *An introduction to the theory of point processes*. Springer-Verlag, New York.
- [14] Diggle, P. J., Besag, J. E., and Gleaves, J. T. (1976) “Statistical analysis of spatial patterns by means of distance methods.” *Biometrics*. **32**: 659-667.
- [15] Diggle, P. J. (1983) *Statistical Analysis of Spatial Point Patterns*. Academic Press, London.
- [16] Dunsmuir, W. and Robinson, P. M. (1981) “Estimation of Time Series Models in the Presence of Missing Data.” *Journal of the American Statistical Association*. **76** (375): 560-568.
- [17] Goldberg, R. R. (1961) *Fourier Transforms*. Cambridge University Press, London.
- [18] Goovaerts: (1997) *Geostatistics for Natural Resource Evaluation*. Oxford University Press, Oxford.
- [19] Haas, T. C. (1995) “Local Prediction of a Spatio-Temporal Process with an Application to Wet Sulfate Deposition.” *Journal of the American Statistical Association*. **90**, (432): 1189-1199.

- [20] Hanisch, K. H. and Stoyan, D. (1979) "Formulas for second-order analysis of marked point processes." *Mathematische Operationsforschung und Statistik, Series Statistics*. **14**: 559-567.
- [21] Haberman, R. (1987) *Elementary Applied Partial Differential Equations*. Prentice-Hall, Inc., Englewood Cliffs, New Jersey.
- [22] Hinkelmann, K. and Kempthorne, O. *Design and Analysis of Experiments (Volume I) - Introduction to Experimental Design*. Wiley and Sons, New York.
- [23] Journel, A. G. and Huijbregts, C. J. (1978) *Mining Geostatistics*. Academic Press, London.
- [24] Kooperberg, C. and O'Sullivan, F. (1996) "Predictive Oscillation Patterns: A Synthesis of Methods for Spatial-Temporal Decomposition of Random Fields." *Journal of the American Statistical Association*. **91**, (436): 1485-1496.
- [25] Koopmans, L. H. (1971) *The Spectral Analysis of Time Series*. Academic Press, London.
- [26] Kaluzny, S. P., Vega, S. C., Cardoso, T. P., and Shelly, A. A. (1998) *S+ Spatial Stats: User's Manual for Windows[®] and UNIX[®]*. Springer, New York.
- [27] Lotwick, H. W. and Silverman, B. W. (1982) "Methods for analysing spatial processes of several types of points." *Journal of the Royal Statistical Society B*. **44**: 406-413.
- [28] Matern, B. (1986) "Spatial Variation." *Lecture Notes in Statistics. Second Edition (1986)*. **36**, Springer, New York.
- [29] Milhøj, A. (1984) "Bias Correction in the Frequency Domain Estimation of Time Series Models." *Biometrika*. **71**, (1): 91-99.
- [30] Mugglestone, M. A. and Renshaw, E. (1996a), "The Exploratory Analysis of Bivariate Spatial Point Patterns using Cross-Spectra." *Environmetrics*. **7**: 361-377.

- [31] Mugglestone, M. A. and Renshaw, E. (1996b), “A Practical Guide to the Spectral Analysis of Spatial Point Processes.” *Computational Statistics & Data Analysis*. **21**: 43-65.
- [32] Ogata, Y. (1999) “Seismicity Analysis through Point-process Modeling: A Review.” *Pure and Applied Geophysics*. **155**: 471-507.
- [33] Rathbun, S. L. (1996) “Asymptotic properties of the maximum likelihood estimator for spatio-temporal point processes.” *Journal of Statistical Planning and Inference*. **51**: 55-74.
- [34] Rathbun, S. L. and Cressie, N. A. C. (1994) “A Space-Time Survival Point Process for a Longleaf Pine Forest in Southern Georgia.” *Journal of the American Statistical Association*. **89**, (428): 1164-1174.
- [35] Renshaw, E. and Ford, E. D. (1983) “The interpretation of process from pattern using two-dimensional spectral analysis: Methods and problems of interpretation.” *Applied Statistics*. **32**, (1): 51-63.
- [36] Rigas, A. G. (1991) “Spectral Analysis of Stationary Point Processes using the fast Fourier Transform algorithm.” *Journal of Time Series Analysis*. **13**, (5): 441-450.
- [37] Ripley, B. D. (1976) “The second-order analysis of stationary point processes.” *Journal of Applied Probability*. **13**: 255-266.
- [38] Ripley, B. D. (1988) *Statistical Inference for Spatial Processes*. Cambridge University Press, London.
- [39] Scott, D. W. (1992) *Multivariate Density Estimation: Theory, Practice, and Visualization*. Wiley and Sons, Inc, New York.
- [40] Stoyan, D. and Stoyan, H. (1985) “On one of Matern’s hard-core point process models.” *Mathematische Nachrichten*. **122**: 205-214.

-
- [41] Strichartz, R. (1994) *A guide to distribution theory and Fourier transforms*. CRC Press LLC, Boca Raton.
- [42] Tobler, W. (1970) "A Computer Movie Simulating Urban Growth in the Detroit Region." *Economic Geography*. **46**: 234-240.
- [43] Vecchia, A. V. (1985) "A general class of models for stationary two-dimensional random processes." *Biometrika*. **72**, (2): 281-291.
- [44] Walters, J. R., Daniels, S. J., Carter, J. H., Doerr: D., Brust, K., and Mitchell, J. M. (1998) "Foraging Habitat Resources, Preferences and Fitness of Red-cockaded Woodpeckers in the North Carolina Sandhills." Technical Report, Virginia Tech.
- [45] Worton, B. J. (1989) "Kernel Methods for Estimating the Utilization Distribution in Home-Range Studies." *Ecology*. **70**, (1): 164-168.

VITA

SUNDARDAS S. DORAI-RAJ

Sundardas S. Dorai-Raj was born on August 24, 1971, in Toronto, Ontario, Canada, to parents Balasundarum and Diana Dorai-Raj. His academic achievements include a B.S. and M.A. in Applied Mathematics from the University of Alabama in Tuscaloosa and a M.S. and Ph.D. in Statistics from Virginia Tech. He has also received the J.C. Arnold award and a commendation from the Virginia Tech Graduate School for his accomplishments in graduate student teaching. Upon graduating from Virginia Tech, Sundardas will continue his academic career as an Assistant Professor of Statistics at Auburn University in Auburn, Alabama, starting August, 2001.